Specific heat in the fractional quantum Hall regime

Benjamin A. Schmidt

Department of Physics
McGill University
Montréal, Québec, Canada

August 2019

A thesis submitted to McGill University in partial fulfillment of the degree of
Doctor of Philosophy

Acknowledgements

First and foremost, I thank Professor Guillaume Gervais for his unfailing confidence in me throughout my PhD. I loved every second I spent in the lab - whether soldering circuits, installing pumps, sketching on the whiteboard or endlessly transferring liquid helium into the insatiable refrigerator. None of this would have been possible without his unfaltering support.

In addition to the many scientific discussions I had with Guillaume, I also benefitted from conversations with a number of other faculty members, including Thomas Szkopek and Aashish Clerk at McGill, Kun Yang at the National High Magnetic Field Laboratory, and an endless stream of visitors to the lab and fellow conference-goers. These numerous opportunities to discuss openly my work and "talk shop" with so many fantastic researchers was one of the great aspects of the research environment that Guillaume was able to provide.

To perform any of my experiments, I first needed samples to measure. I am grateful to Loren Pfeiffer and Ken West at Princeton University and John Reno and Dominique Laroche at Sandia National laboratories for providing samples. Even though I had the best samples available, I would not have gotten anywhere in the lab without the help of technicians/miracle-workers, John Smeros, Richard Talbot and Robert Gagnon. I also benefitted greatly from the assistance of Juan Galego to keep the computers running and Pascal Bourseguin in the machine shop. I am also thankful to the rest of the physics department faculty and staff, who in various ways facilitated my research, enriched my studies and made my time at McGill so enjoyable.

I am extremely grateful to my partner-in-crime on the LabGUI software, Pierre-Francois Duc, who took my early version of the software and levelled it up by an order of magnitude.

I would be remiss not to mention the students and postdocs I worked most closely with in the lab. Xiaoqing Zhou was my original scientific sparring partner, and I deeply miss the discussions and camaraderie we had during those long days we spent together in the lab. I am grateful also to my more recent collaborators:

Bram Evert, Binxin Wu, Keyan Bennaceur, Samuel Gaucher, Simon Bilodeau and finally Matei Petrescu. I have learned so much from each of them in turn.

Michel Savard deserves special mention as a personal and scientific confidant - even though we lived on opposite sides of the lab, we had many important discussions on many different topics. I would also like to thank all the other people I was lucky enough to spend time with in the lab, even if we didn't work on the same projects. This includes people like James Hedberg, Olivier Cyr-Choinière, Prof. Qian Luo, Oulin Yu, Eli Martel, and a rotating cast of undergraduate students too numerous to list but all impactful in their own way.

I was fortunate to have been part of a fantastic community at McGill and in Montreal. I spent many happy hours on the ice with my teammates on the Absolute Zeros and our bitter rivals on Cold Fusion; in particular, Captain Jessica and Coach Jeff helped me grow as a player and a person. I am thankful that my close friends Nally and Geoffrey were there for me throughout my PhD. I would also like to thank my family, especially Miranda and my parents, for their love and encouragement that was critical to my success. As ever, I am deeply grateful to Ting for her unending love and support, even while I was distant - physically and/or metaphorically.

My work at McGill University was funded by the Natural Sciences and Engineering Research Council of Canada (NSERC), the Fonds de Recherche du Québec - Nature et Technologies (FRQNT) and the Canadian Institute for Advanced Research (CIFAR). I am extremely grateful to NSERC and the Department of Physics for fellowship support during my studies.

Abstract

The two dimensional electron gas (2DEG) that forms in ultra-clean GaAs/AlGaAs heterostructures at low temperature is a versatile platform for the study of low dimensional physics and many-body interactions. Most famously, it hosts the fractional quantum Hall effect (FQHE) - a series of exotic states formed by the condensation of the electrons into a Laughlin liquid with fractionally charged excitations. One state in particular, the $\nu = 5/2$ fractional quantum Hall state, remains the subject of intense theoretical and experimental effort, due to the conjecture that its low-energy excitations may obey non-Abelian quantum statistics. This thesis describes a novel experimental technique to measure the specific heat of the 2DEG and results in the second Landau level, including the first ever measurements of specific heat in absolute units at $\nu = 5/2$.

The first major result discussed in this thesis is the observation of the $\nu = 5/2$ fractional quantum Hall effect in the Corbino geometry. Unlike in conventional geometries there is no edge connecting the two contacts, which enables us to study bulk transport without complications due to the physics of the quantum Hall edge.

The next major result we describe is a direct measurement of the electron-phonon thermal relaxation time and thermal conductivity, from which we determine the specific heat of the 2DEG. We find thermal time constants of a few microseconds in the temperature range 50-100 mK for several filling factors in the second Landau level, with thermal relaxation somewhat slower at $\nu = 5/2$ than other filling factors. The specific heat of the 2DEG is significantly enhanced above its value in the absence of magnetic field and follows an activation-like behaviour, as expected for a gapped state. By integrating the specific heat, we obtain the entropy of the 2DEG, and find remarkable agreement with previously reported measurements of the entropy via longitudinal thermopower at both $\nu = 5/2$ and $\nu = 7/3$. Further refinement of our specific heat measurement technique could lead to detection of the non-Abelian entropy at $\nu = 5/2$.

Abrégé

Le gaz électronique bidimensionnel qui se forme dans une hétérostructure de GaAs/AlGaAs de très haute mobilité à basse temperature est une plate-forme polyvalente pour l'étude de la physique en basses dimensions et des interactions multicorps. L'effet le plus célèbre est l'effet Hall quantique fractionnaire (EHQF): une série d'états exotiques qui se forment quand les électrons se condensent en un liquide de Laughlin avec excitations de charges fractionnaires. Un état en particulier, l'état de Hall quantique fractionnaire de $\nu = 5/2$, est déjà un sujet de recherche théorique et expérimental intensif, parce qu'il y a une conjecture que ses excitations de basse énergie obéissent aux statistiques quantiques non abéliennes. Cette thèse décrit une technique expérimentale pour mesurer la chaleur spécifique d'un gaz électronique bidimensionnel et les résultats dans le deuxiéme niveau de Landau, incluant les premières prises de mesures de chaleur spécifique dans l'état 5/2.

Le premier résultat abordé dans cette thèse est l'observation de l'état $\nu = 5/2$ pour une géométrie de Corbino. Contrairement aux autres géométries conventionnelles il n'y a pas de bords qui relient les deux bornes, permettant d'étudier le transport électronique dans le volume de l'échantillon sans les complications dues aux états de Hall quantique des bords.

Le deuxième résultat dans cette thèse est la mesure directe de la constante de temps de relaxation thermique electron-phonon et la conductivité thermique permettant de déterminer la chaleur spécifique d'un gaz électronique bidimensionnel. Des constantes de temps de l'ordre de quelques microsecondes à 50-100 mK dans le deuxiéme niveau de Landau sont obtenues, dont la plus lente est observée pour l'état 5/2. La chaleur spécifique est augmentée considérablement au-dessus de sa valeur en absence de champs magnétique et suit un comportement semblable à celui de l'activation, comme prévu pour un état incompressible. En intégrant la chaleur spécifique, nous obtenons l'entropie du 2DEG et avons trouvé un accord remarquable avec les mesures précédemment reportées de l'entropie via une puissance thermoélectrique longitudinale pour l'état 5/2 et l'état 7/3. Un affinement supplémentaire de notre technique de mesure de la chaleur spécifique pourrait mener

à la détection de l'entropie non abélienne à l'état 5/2.

Statement of Originality

This thesis represents genuine scholarship by the author, including original contributions to the field of low-temperature condensed matter physics. Specific portions of the thesis present results that have previously been published elsewhere, as described below. The author's contribution to the work are as follows:

- *Theory of non-Abelian entropy measurements:* The experimental proposals to detect non-Abelian anyons via entropy measurements (Chapter 3) are due to their respective authors, including the adiabatic cooling proposal by author's supervisor, Guillaume Gervais (GG), and Kun Yang (KY) [*Phys. Rev. Lett.* **105**, 086801 (2010)]. The author of this thesis, BAS, assisted with verification of the calculation and estimates published in the aforementioned paper, and further original calculations, entirely by BAS, are presented in Appendix D. The impetus to measure specific heat was due to BAS, and ideas about how to potentially link it to non-Abelian entropy came from discussions between GG and BAS.

- *Apparatus:* The low-temperature apparatus, including the dilution refrigerator, magnet, experimental tail and instrumentation were substantially in place prior to the arrival of the author at McGill University. BAS was responsible for repair and upgrades of subsystems including the pumps and pumping lines, design and construction of new sample holders and optimization of the instrumentation setup. Details of some of the instrumentation work are presented in Chapter 4.

- *FQHE in the Corbino Geometry:* The idea to use the Corbino geometry in our lab was championed by Keyan Bennaceur (KB), who along with Simon Bilodeau (SB) fabricated the Corbino geometry samples. Data collection software (LabGUI) was written by BAS and Pierre-Francois Duc, making use of a variety of open source software including Python, PyQT, NumPy, SciPy and MatPlotLib. All measurements reported in Chapter 5 were performed by BAS, apart from the data in Figure 5.10, the raw data for which was gathered by Matei Petrescu (MP). All analysis was carried out by BAS, who also made the original connection between our data and the earlier works studying the relationship between Arrhenius plots and quasiparticle charge. The work was carried out under the guidance of GG, including scientific discussions led by GG that included BAS, KB and SB. The results were first published as *Solid State Comm.* **217** 1-5 (2015), *Fast Track.* Portions of Chapter 5 closely follow and paraphrase the aforementioned paper, which was itself written entirely by BAS.

- *Thermalization of the 2DEG:* The synthesis of existing models and experimental results into a model for thermalization of our Corbino device under Joule heating, culminating in numerical calculations of the temperature profiles in our Corbino devices presented in Chapter 5, represents original scholarship by BAS. In particular, BAS devised the model and carried out all analytical and numerical calculations, under the supervision of GG and with verification of certain calculations by MP. The mathematical derivation presented in Appendix C first appeared in the supplementary information to *Phys. Rev. B* **95** 201306 (2017).

- *Specific heat experiment:* The idea to do the specific heat experiment presented in Chapter 7, originally as a first step towards adiabatic cooling, was due to BAS as part of an overall research program set out by GG. The experimental design was devised and refined by BAS, including the unipolar square wave scheme and "shift-and-add" procedure to null extraneous transients. Measurements were carried out by BAS, using custom data collection scripts. Data analysis was performed by BAS under the guidance of GG and with helpful discussion with other lab members. Significant contributions to the study of condensed matter physics include:

  - A novel experimental technique to measure the thermalization time and specific heat of a 2DEG.
  - The first reported measurement of the specific heat of a 2DEG below 100 mK, in absolute units with no phonon contribution.
  - Comparison of the inferred entropy with thermopower power data.

  The results presented in Chapter 7 and Appendix F were previously reported in *Phys. Rev. B* **95** 201306 (2017), *Rapid Communications.* Portions of Chapter 7 closely follow the text of that paper, including certain paraphrased sections.

- Additional experiments: Appendix E presents some of the author's additional experimental work, based on original experimental concepts by BAS. In particular, the interpretation of rectification in the gated Hall bar in terms of self-gating, the idea to try to use the thermal gradient due to Joule heating in the Corbino device to drive thermopower, and the concept to use RF non-resonant heating do drive $\partial\mu/\partial T$ are all original ideas by BAS. The presented measurements and analysis were also carried out by BAS.

Contents

List of Figures

List of Abbreviations

2DEG Two-dimensional electron gas

CF Composite fermion

CMRR Common mode rejection ratio

DOS Density of states

FQHE Fractional quantum Hall effect

IQHE Integer quantum Hall effect

LL Landau level

LLL Lowest Landau level

MR Moore-Read

NA Non-abelian

PZ Piezoelectric

QH Quantum Hall

SdH Shubnikov-de Haas

SLL Second Landau level

SNR Signal-to-noise ratio

VdP Van der Pauw

WF Wiedemann-Franz

Chapter 1

Introduction

1.1 Introduction

According to modern physics, all particles may be classified into two categories: bosons and fermions. Bosons, such as photons, may occupy the same quantum state; hence, light can be amplified coherently in lasers and used to send information down fibre optic lines, create holograms, or even cut steel. Conversely, fermions, such as electrons, obey the Pauli exclusion principle: each one demands its own state, and thus they obey Fermi statistics. However, it turns out that this restriction to two classes of particles arises from the three dimensional nature of our universe. In a two dimensional world, there could be other classes of particles. Such particles, called anyons - because they can have “any” phase - would break the boson-fermion dichotomy with striking results. In particular, so-called non-Abelian (NA) anyons could be used to build a topological quantum computer that would be inherently robust against noise and decoherence. In this thesis, I will discuss progress toward performing measurements that could confirm the existence of non-Abelian anyons in one particular system: the 5/2 fractional quantum Hall effect (FQHE). While other experimental approaches have given results consistent with non-Abelian behaviour [1], and new material systems have gained traction as possible platforms for topological quantum computation [2], unequivocal observation of this bizarre piece of two-dimensional physics remains elusive.

1.2 Outline of the thesis

Chapter 2 will serve as a primer on quantum Hall (QH) physics, providing some background necessary to understand the rest of the thesis. I will start by introducing some mathematical notation, and then proceed with an overview of the classical Hall effect, Shubnikov-de-Haas oscillations, integer quantum Hall effect (IQHE), fractional quantum Hall effect and finally the 5/2 FQHE.

In Chapter 3, I will discuss in detail several "bulk entropy measurement" schemes for detection of non-Abelian states. A number of such experiments have been proposed, and preliminary thermopower results have already been reported in the literature. I will provide summaries of these proposals, as well as progress toward experimental realization of them where applicable.

The next chapter, Chapter 4, introduces our instrumentation and measurement apparatus. Low temperature physics requires specialized equipment to cool the sample to a fraction of a degree above absolute zero and probe the sensitive quantum states that occur under those conditions. I will primarily discuss optimization of the low-noise measurement circuit for our particular studies, touching only briefly on the refrigeration techniques used.

All of the experiments proposed in Chapter 3 rely on measurements of the bulk of the two-dimensional electron gas, while in conventional transport measurements most of the current flows at the edge of the sample. Chapter 5 introduces the Corbino geometry, which can circumvent this problem for some types of experiments. I will introduce general transport measurement techniques and benchmark results for our highest quality Corbino sample. This chapter is adapted in part from our publication "Second Landau Level Fractional Quantum Hall Effects in the Corbino Geometry" [3].

Chapters 6 and 7 are based on our publication "Specific heat and entropy in the second Landau level fractional quantum Hall effect" [4] and contain the central results of this thesis: direct measurements of the specific heat of the electron system in the QH regime, including in the 5/2 fractional quantum Hall effect. Chapter 6 begins with a literature review regarding thermalization of a two-dimensional electron gas, before discussing numerical calculations of electron thermalization in our Corbino device. Chapter 7 introduces a novel technique to measure the electron thermal relaxation time constant and specific heat. This technique was used to perform the measurements in the second Landau level, which are reported and discussed in the same chapter. In the last part of the chapter, we compare the entropy as determined from our measurements of specific heat to existing thermopower results, and find remarkably good agreement at filling factors 5/2 and 7/3.

Finally, Chapter 8 provides a summary and discusses the future outlook for these types of experiments.

1.3 Notational conventions

Throughout this thesis, S is used to denote the Seebeck coefficient (thermopower), while $\mathcal{S}$ is used to denote entropy. Where applicable, upper case letters will be used to denote extrinsic quantities (*e.g.* heat capacity, C), and lower case letters for their intrinsic equivalents (*e.g.* specific heat, c). Symbols are defined at their first usage.

Chapter 2

Background

This chapter will provide an overview of the major concepts used in the later chapters of this thesis. In particular, we will discuss the integer and fractional quantum Hall effects, focusing on the 5/2 fractional quantum Hall effect. We will first introduce the mathematical formalism and notation required to describe resistivity (and conductivity) of 2D materials with both longitudinal and transverse components. We will then discuss the effects of a magnetic field on a 2D system with increasing "quantumness" - *i.e.* lower temperature and disorder. These effects are the Hall effect, Shubnikov-de Haas (SdH) oscillations, the integer quantum Hall effect (IQHE) and the fractional quantum Hall effect (FQHE). Finally, we will discuss the peculiar physics of the second Landau level (SLL), including the 5/2 FQHE, and briefly summarize the experimental status of the field of 5/2 FQH physics.

2.1 Two-dimensional resistivity and conductivity as tensors

For a two-dimensional sample, the usual scalar relations between the electric field $\vec{E}$ and current density $\vec{j}$ are

$$\vec{E} = \rho\vec{j}, \tag{2.1}$$

and

$$\vec{j} = \sigma\vec{E}, \tag{2.2}$$

where ρ is the resistivity (sometimes called sheet resistance), σ is the conductivity (sheet conductance), and $\rho = 1/\sigma$. In some situations, such as under the influence of an external magnetic field, $\vec{E}$ and $\vec{j}$ may not be parallel, and we must instead use the tensor relations

$$\vec{E} = \hat{\rho}\vec{j}, \tag{2.3}$$

with

$$\hat{\rho} = \begin{pmatrix} \rho_{xx} & \rho_{xy} \\ -\rho_{xy} & \rho_{yy} \end{pmatrix}, \tag{2.4}$$

and

$$\vec{j} = \hat{\sigma}\vec{E} \tag{2.5}$$

with

$$\hat{\sigma} = \begin{pmatrix} \sigma_{xx} & \sigma_{xy} \\ -\sigma_{xy} & \sigma_{yy} \end{pmatrix}. \tag{2.6}$$

The components ρ_{xx} and ρ_{yy} provide the longitudinal resistivity along the x- and y-directions, and are equal if the resistivity is isotropic. The off-diagonal resistivity, ρ_{xy} is also known as the *Hall resistivity.* In transport experiments, what is actually measured is either the macroscopic resistance (R), or conductance (G), rather than their microscopic counterparts. Using the geometry of Figure 2.1, the Hall resistance and Hall resistivity are exactly equal with no geometric factors as follows:

$$\rho_{xy} = \frac{E_y}{j_x} = \frac{V_y/w}{i_x/w} = \frac{V_y}{I_x} = R_{xy}. \tag{2.7}$$

A similar equality also holds for σ_{xy} and G_{xy}. Incidentally, this mathematical quirk helps to make the integer quantum Hall effect (which will be discussed later) a practical resistance standard by reducing the need for extremely precise sample geometries. A measurement of the Hall resistance is a direct measurement of the Hall resistivity, hinting at how the Hall effect links experimental observables to deep underlying physics.

By substituting equation 2.5 into equation 2.3, we can obtain the relations between the resistivity and conductivity components for isotropic conductivity as follows:

$$\sigma_{xx} = \frac{\rho_{xx}}{\rho_{xx}^2 + \rho_{xy}^2}, \quad \rho_{xx} = \frac{\sigma_{xx}}{\sigma_{xx}^2 + \sigma_{xy}^2} \tag{2.8}$$

$$\sigma_{xy} = \frac{-\rho_{xy}}{\rho_{xx}^2 + \rho_{xy}^2}, \quad \rho_{xy} = \frac{-\sigma_{xy}}{\sigma_{xx}^2 + \sigma_{xy}^2}. \tag{2.9}$$

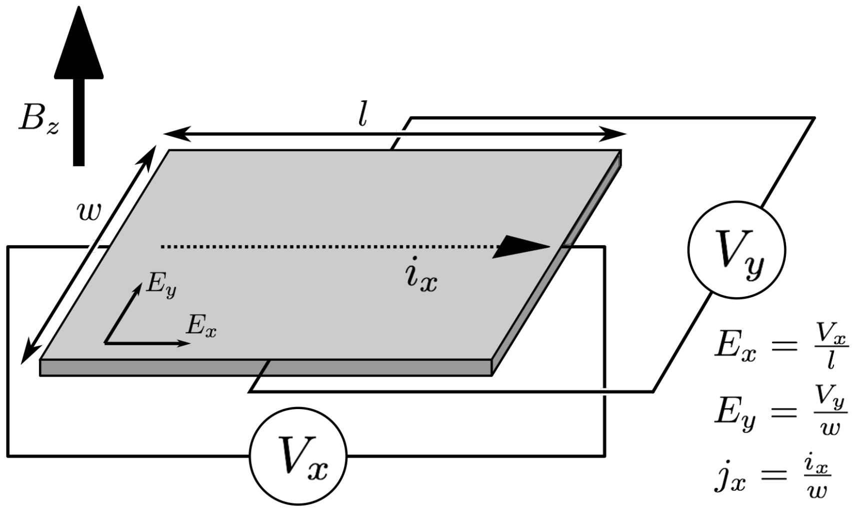

Figure 2.1: Geometry of a 2D conductor in a perpendicular magnetic field.

In high magnetic field conditions, $\rho_{xy} \gg \rho_{xx}$, equation 2.8 simplifies to

$$\sigma_{xx} = \frac{\rho_{xx}}{\rho_{xy}^2}, \tag{2.10}$$

which is surprising, since it means that the resistivity and conductivity of the sample are actually proportional to each other. Later, we will see the extreme case of this: an insulating state that shows zero resistance. This is just the first of many intriguing results in Hall effect physics, and it comes simply from considering conductivity and resistivity as tensors.

2.2 The Hall effect

The classical Hall effect describes the behaviour of a conductor in a magnetic field. For example, consider a thin rectangular metal film in the x-y plane, with a magnetic field applied in the z-direction. Just as in the zero-field case, if a current is applied in the x-direction, a voltage drop may be measured along the x-direction according to Ohm's law: $V_x = I_x R_{xx}$. However, if we measure along the y-direction, there is also a transverse voltage V_y. The origin of this voltage is the Lorentz force acting on the charge carriers according to

$$\vec{F} = q\vec{v}_d \times \vec{B}_z, \tag{2.11}$$

where q is the carrier charge, v_d is the drift velocity and B_z is the magnetic field perpendicular to the sample. As illustrated in Figure 2.2, charge carriers build up on one side of the sample, such that the force due to their electric field ($F = qE_y$) balances the Lorentz force. The resulting Hall resistance, after using the relation $j_x = nqv_d$, where n is the carrier density, is given by

$$R_H \equiv R_{xy} = \frac{E_y}{j_x} = \frac{B_z}{qn}. \tag{2.12}$$

Interestingly, the sign of R_H depends on the charge of the carriers, and so Hall measurements find practical use to determine the majority carrier density and type (electrons or holes) in semiconductors. Conversely, sensors made from material with known carrier density and type are routinely used to measure magnetic field in industrial applications.

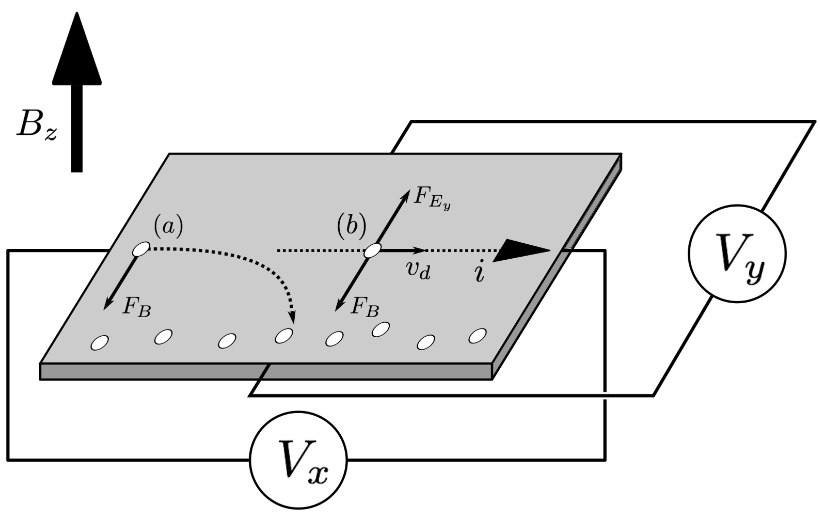

Figure 2.2: Illustration of the classical Hall effect. An applied current in the x direction, i, drives charged particles (positively charged holes, in this case) through the sample. (a) Initially, the Lorentz force deflects them towards one side of the sample. (b) They soon build up there, creating an electric field E_y that, in steady state, exactly balances the Lorentz force. The associated voltage, V_y, is called the Hall voltage, and V_y/i is the Hall resistance.

2.3 Shubnikov-de Haas Oscillations

Much of the interesting physics that emerges in condensed matter systems has to do with their density of states (DOS), especially near the Fermi level, which is the boundary between filled and unfilled states. At zero magnetic field, the DOS (denoted g throughout this thesis) for a two-dimensional electron gas (2DEG) is flat as shown in Figure 2.3a. The zero-field DOS, g_0, is simply given by

$$g_0 = \frac{n_e}{E_f} = \frac{m^*}{\pi\hbar^2}, \tag{2.13}$$

where m^* is the band effective mass of the carriers, n_e is the electron density and E_f is the Fermi energy.

However, when a magnetic field is applied, the DOS is modulated by the formation of Landau levels (LLs). These can be roughly understood at the semiclassical level as quantized cyclotron motion. A charged particle in a magnetic field, such as an electron, tends to move in a circle. If its quantum mechanical coherence length is greater than the circumference of the circle, we can also consider it as a wave, and require that the circumference is equal to an integer number of wavelengths. We can therefore define a magnetic length[1],

$$l_B = \sqrt{\frac{\hbar}{eB_z}}, \tag{2.14}$$

which is the radius of the circle for which an electron with momentum $\hbar k$ completes exactly one wavelength, $\lambda = 2\pi/k$ during the orbit. The corresponding cyclotron energy E_c and frequency ω_c are

$$E_c = \hbar\omega_c = \frac{\hbar e B_z}{m^*}, \tag{2.15}$$

where m^* is the electron's cyclotron effective mass. In the absence of disorder, the DOS would be a comb of Dirac delta functions, spaced apart by $\hbar\omega_c$. Indeed, the complete solution of the 2D Schrödinger equation in a magnetic field yields the following DOS,

$$g(\epsilon) = \frac{g_0}{\hbar\omega_c} \sum_{n=1}^{\infty} \delta(\epsilon - \epsilon_n), \tag{2.16}$$

[1] l_B should not be confused with the cyclotron radius for electrons at the Fermi surface, $R_c \equiv \hbar k_f/qB$. The condition $R_c = l_B$ occurs when the first Landau level is perfectly filled.

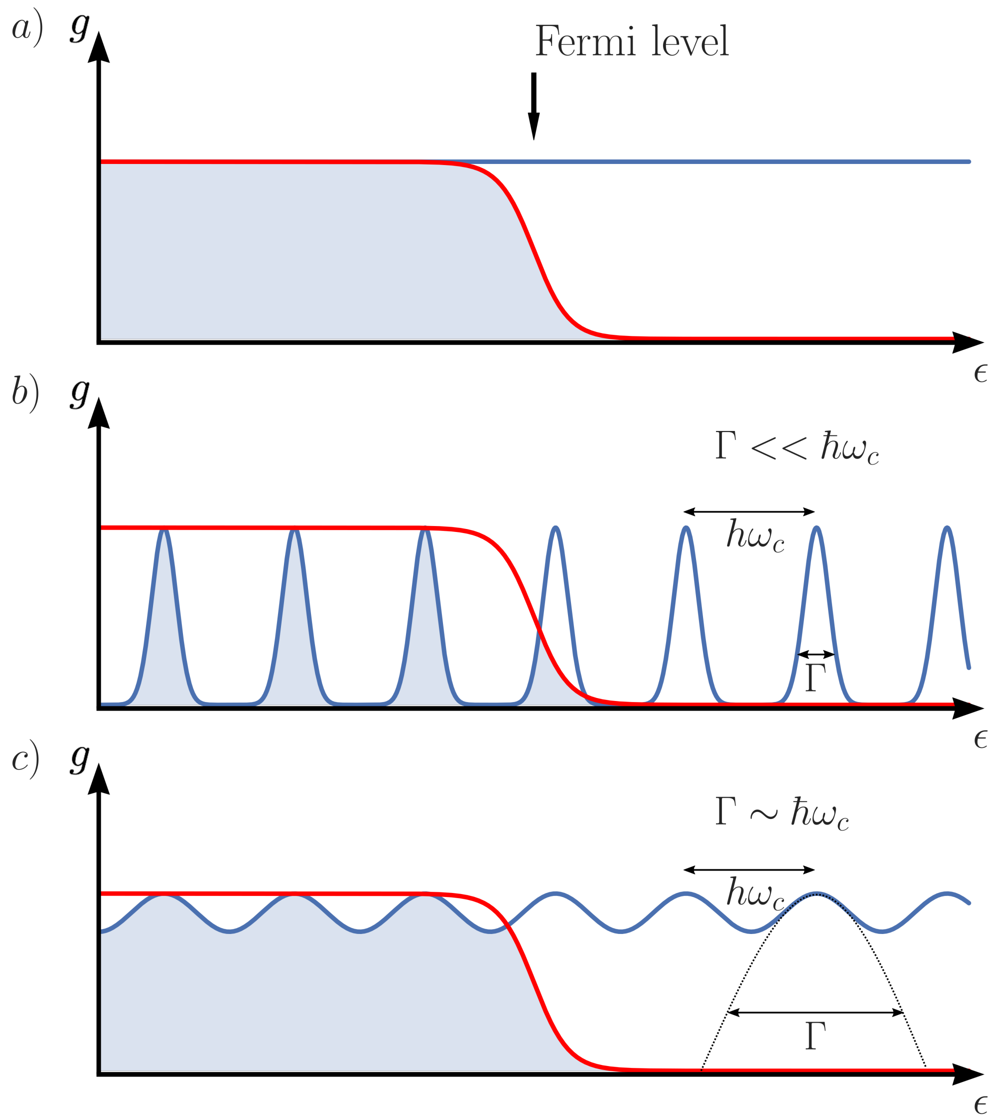

Figure 2.3: Density of states (blue line) and fermi function (red line) with filled states shaded in light blue a) DOS at B = 0. b) DOS with well-separated Landau levels. c) DOS with broad Landau levels, which overlap leading to sinusoidal modulation of DOS.

where $\epsilon_n = (n + 1/2)\hbar\omega_c$ [5]. The number of available states in each Landau level is given by $n_B = g_0\hbar\omega_c = eB/h$, *i.e.* the area under each peak is normalized by the spacing of the peaks. However, disorder in real samples broadens the peaks, yielding a DOS like the one shown in Figure 2.3b. The width of this broadening function is conventionally denoted Γ. Whether the broadening function is Gaussian, Lorentzian, semi-elliptical, semi-parabolic or something else has been an issue of extensive discussion in the literature (see, for example, [6] and references therein). However, at low magnetic field, for $\hbar\omega_c \ll \Gamma$, all choices lead to a DOS of the form

$$g(\epsilon) = g_0 + \Delta g \sin\left(\frac{2\pi\epsilon}{\hbar\omega_c}\right), \tag{2.17}$$

as depicted in Figure 2.3c. Since the physics of electronic systems depends on the density of states within roughly $k_B T$ of the Fermi level, many properties of the 2DEG vary sinusoidally as either the magnetic field or Fermi level is tuned. These oscillations are generally known as the de Haas-van Alphen effect, and for conductivity the SdH effect. In Chapter 5, we will discuss SdH oscillations in more detail when we use them to characterize the mobility and quantum lifetime of carriers in our devices.

2.4 Integer quantum Hall effect

As the magnetic field is increased, the broadened Landau Levels eventually become well-separated when $\hbar\omega_c > \Gamma$, as shown in Figure 2.3b. If the Fermi level lies between two Landau levels, the conductivity approaches zero. Correspondingly, the resistivity also vanishes as a consequence of the tensor relation (Equation 2.8). As von Klitzing *et al.* discovered in 1980 [7] plateaus also emerge in R_H, which are perfectly quantized in units of the quantum of conductance (Figure 2.4).

To help describe what is happening, we can introduce the concept of a filling factor, ν, which is simply the number of Landau levels that the electrons fill. For example, in Figure 2.3, three Landau levels are full and the fourth one is one quarter full, so $\nu = 3.25$.[2] More formally, we have the filling factor

$$\nu = \frac{n_e}{n_B} = \frac{n_e h}{eB}, \tag{2.18}$$

[2]Note that the nomenclature becomes somewhat complicated due to spin splitting: $\nu = 3.25$ is considered to be in the second Landau level, since the first Landau level includes the spin up and spin down branches in the range $0 < \nu < 2$. Furthermore, $\nu = 3.25$ is also in the upper spin branch of the $N = 1$ Landau level, where N is the filling factor neglecting spin splitting and counting from zero.

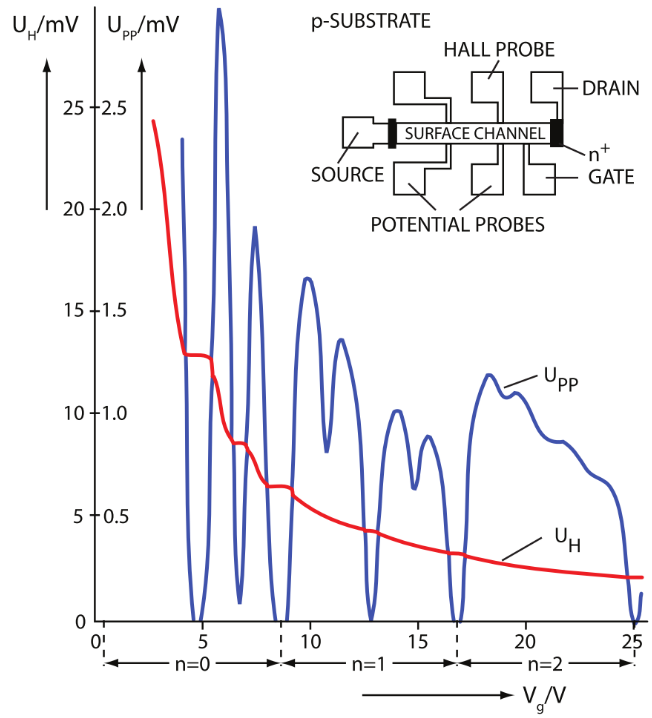

Figure 2.4: Discovery of the quantum Hall effect by Klaus von Klitzing in a MOSFET device. The longitudinal resistivity (blue) shows deep minima, while the transverse resistivity (red) shows quantized plateaus at the same field values. Note the x-axis is electron density, controlled using an electrostatic gate, rather than magnetic field. Data from reference [7], enhanced and colourized figure reproduced with permission from reference [8].

and correspondingly the magnetic field for a particular filling factor,

$$B_\nu = \frac{n_e}{n_B} = \frac{n_e h}{e\nu}. \tag{2.19}$$

The hallmark signature of the IQHE is the combination

$$\rho_{xx} = 0 \tag{2.20}$$

and

$$\rho_{xy} = \frac{h}{ie^2} \tag{2.21}$$

for $i - \epsilon < \nu < i + \epsilon$, where i is an integer and ϵ is the half-width of the plateau. Although it is quite straightforward to see that σ_{xx} vanishes due to the lack of conducting states when the Fermi energy sits between two Landau levels, it is less obvious why ρ_{xx} should also vanish. The question is: where does the current flow with zero resistance in a sample with no conductance? The answer is that it flows around the edge of the sample. This can most readily be understood in the "band-bending" picture, shown in Figure 2.5. The Landau levels form extended states in the bulk, but at the edges of the sample they bend upwards. Where each one crosses the Fermi level, it forms a one-dimensional conducting edge channel. Because that channel is in principle dissipationless, the voltage drop along its length is zero and as such $R_{xx} = 0$. However, the conductance of each one-dimensional channel is given by the quantum of conductance, e^2/h, so the total two-point conductance of i edge channels is ie^2/h. Due to the magnetic field, these edge states are also chiral: they flow only in one direction. In the Hall geometry, the potential at each voltage contact is the same as the potential at the current contact upstream from it (since there is no voltage drop along the dissipationless edge channel), so the measurement yields the two-point measurement result: $R_h = h/ie^2$.

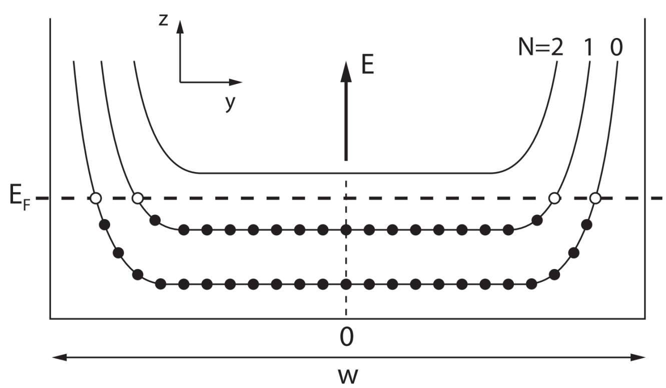

Figure 2.5: Cross section showing band bending at the sample edges in the IQHE. Landau levels are indicated by the solid lines, bending upwards at the edges. States below E_f (dashed line) are filled (indicated by filled circles). Where the bands cross the Fermi level, the unfilled states (empty circles) form one-dimensional chiral edge channels going into or out of the page. Figure reproduced with permission from reference [8].

2.5 Odd integer quantum Hall effect

The Landau levels responsible for the IQHE may be further split due to the electron spin. In the most naive picture, the energy of spin-up and spin-down electrons in a magnetic field differs by the Zeeman energy, E_z. The Zeeman energy is given by

$$E_z = \mu_B g B_z, \tag{2.22}$$

where μ_B is the Bohr magneton and the known value of g in GaAs is -0.44. The resulting value of E_z, $\sim$0.3 K/T, is much smaller than the experimentally observed odd IQH gaps, which are around 6 K/T [6]. In fact, the odd IQHE cannot be understood from a single particle picture; rather, it is necessary to consider exchange-enhancement of the g-factor in order to explain the observed gaps [9]. Piot *et al.* have developed a theory for the onset of spin-splitting as a magnetic-field-induced Stoner transition [6]. Such an explanation is consistent with our results presented in Chapter 5, where we observe the onset of spin splitting at extremely low magnetic fields and odd-integer resistivity minima of width similar to the even-integer minima. This would be impossible to understand in the simple non-interacting Zeeman picture.

2.6 Fractional quantum Hall effect

In samples with very low disorder, additional quantum Hall plateaus emerge at fractional filling factors, with fractionally quantized Hall resistivity. In order to understand this phenomenon, it is necessary to consider the many-body physics of interacting electrons. One way to understand the particular fractions that occur is through the composite fermion (CF) picture. We begin by quantizing the magnetic flux into fluxons carrying magnetic flux of $\Phi = h/e$. The number of fluxons per unit area is then $n_\Phi = B/\Phi$, which means that we can rewrite the filling factor as simply $\nu = n_e/n_\Phi$. The IQH condition occurs when the number of electrons is an integer multiple of the number of flux quanta. Now we consider the possibility that an electron can pair with two flux quanta to form a new quasiparticle called a composite fermion (CF). A 2D CF gas is also subject to the IQHE, however the effective field it experiences is reduced by the number of flux quanta used up by forming CFs. The remaining flux density n_Φ^* is equal to $n_\Phi - 2n_e$, because two flux quanta per electron are used to create the composite fermions. Additionally, the density of composite fermions n_{CF} is identical to the density of electrons. Therefore, the effective filling factor for the CFs is

$$\nu^* = \frac{n_{CF}}{n_\Phi^*} = \frac{n_e}{n_\Phi - 2n_e}, \tag{2.23}$$

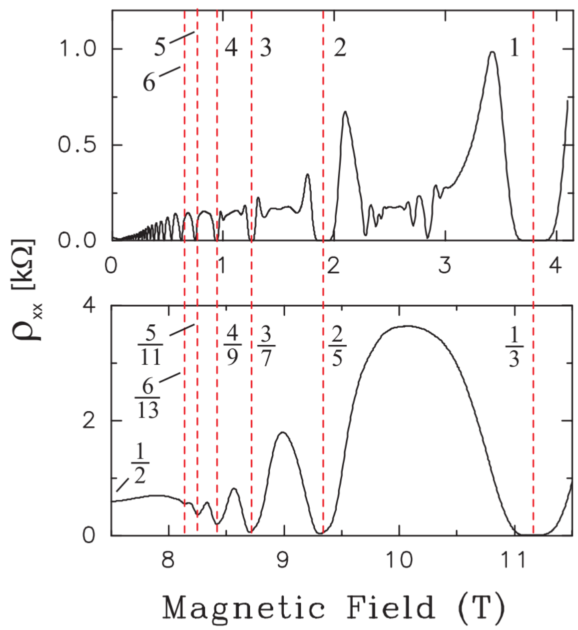

Figure 2.6: Top panel: Magnetoresistance data for a 2DEG, with IQH minima indicated. Bottom panel: FQH minima in the same sample at higher magnetic field. The correspondence between the minima (dashed red lines) are a demonstration of how the FQH minima can be interpreted as IQH minima, but for composite fermions rather than electrons. Figure reproduced with permission from [8] based on data from [10].

or, by dividing through by n_Φ,

$$\nu^* = \frac{\nu}{1-2\nu}, \tag{2.24}$$

which means that ν^* will take on integer values when the electron filling factor is

$$\nu = \frac{p}{1+2p}, \tag{2.25}$$

for p = 1, 2, 3... This explains the filling factors of the most prominant FQH series (1/3, 2/5, 3/7...). Similar constructions using holes instead of electrons, or 4-flux CFs explain most other fractional states. In all cases, Equation 2.25 and its generalizations only allow for the IQHE of CFs to occur for odd-denominator values of ν.

2.7 5/2 fractional quantum Hall effect

In 1987, an even-denominator FQH plateau was observed for the first time, at filling factor 5/2 [11]. This surprising experimental discovery led to a flurry of theoretical proposals, since it does not fit the standard odd-denominator CF series. The most interesting explanation for the $\nu = 5/2$ state is the Moore-Read (MR) Pfaffian wavefunction [12]. In a hand-waving way, it can be understood by considering the same 2-flux CFs invoked in the previous section. Since 5/2 is really 2 + 1/2, the spin-up and spin-down branches of the lowest Landau level (LLL) are both filled. The second Landau level (SLL) is half-filled, yielding a ratio of n_{CF} to n_Φ of 1/2. Therefore, if the CFs form with two fluxons per electron, every fluxon is attached to an electron, leaving zero residual magnetic field. Indeed, in the half-filled LLL, the 2DEG acts much like a Fermi liquid of CF's at zero field. The Moore-Read state is formed by CFs Cooper-pairing to form a "superconducting-like" state, accounting for the observed vanishing ρ_{xx}. This state is particularly interesting because the pairing is exotic: unlike in usual s-wave superconductors, the pairing is p-wave. As a result, the MR state supports *non-Abelian* (NA) excitations. Experimental verification of non-Abelian physics would be a major scientific breakthrough, however there are alternative explanations for the $\nu = 5/2$ and the experimental picture is still murky despite some promising results (see Section 2.8).

Besides the MR Pfaffian state, a number of other theories have been proposed to explain the $\nu = 5/2$ FQHE. One of the first proposed was the Haldane-Rezayi state [13], an Abelian spin-unpolarized state that corresponds to d-wave pairing [14]. Another unpolarized Abelian state is the two-component *331* state [15]. Finally, there is the non-Abelian particle-hole conjugate to the Moore-Read Pfaffian, known as the *anti-Pfaffian* state [16, 17]. Experimental studies of the $\nu = 5/2$ FQHE generally fall into one of two categories: either one tries to compare measured physical properties (such as spin polarization) to the predictions of specific theories, or one tries to observe non-Abelian behaviour directly.

2.7.1 Non-Abelian Anyons

A central concept in many-body physics is the idea of quantum statistics. A group of quantum particles may be described by a collective wavefunction, Ψ. If the particles are well-separated, one may ask what would happen to Ψ if two of the particles swapped places. In three dimensions, there are only two possibilities according to the spin-statistics theorem. For bosons, Ψ is unchanged by particle exchange, while for fermions, it changes to $-\Psi$. In two dimensions, the topological restriction that allows only Bosons and Fermions is lifted, and other statistics are possible. In particular, Abelian anyons can change phase by a fraction of π. Laughlin quasiparticles, such as the $e/3$ quasiparticles at $\nu = 1/3$ behave as Abelian anyons [18]. Non-abelian anyons are even more bizarre. Upon exchange of particles, their wavefunction is transformed by a unitary operator. They are called non-Abelian anyons since the operation acts as a matrix multiplication, so multiple exchange operations do not commute. A sequence of such operations, when considering the world lines of the quasiparticles in two spatial dimensions plus time, can be described mathematically by the braid group. It has been shown that some non-Abelian systems can be used to create a universal quantum computer, with quantum logic gates implemented by specific braiding operations. This is particularly intriguing, since the operations are "topologically protected," and computation based on them should be highly fault-tolerant [19]. The MR Pfaffian state proposed at $\nu = 5/2$ cannot be used to implement a full set of quantum gates, but other quantum Hall states such as $\nu = 12/5$ may [20].

2.7.2 Quasiparticles at $\nu = 5/2$

The low-energy excitations of the Moore-Read state, which contain at their centres the localized non-Abelian anyons, are vortex-like quasiparticles. That is, in the superconductor analogy, the quasiparticles are similar to the vortices that form in a superconductor exposed to a magnetic field smaller than the critical magnetic field. A way to understand this is to think of the 5/2 QH condensate trying to "reject" any deviation in magnetic field away from perfect 5/2 filling. Each flux line that gets introduced gets localized to a small region that pushes away the QH condensate. The charge of the quasiparticle is given by the integral of missing charge density in the vicinity of the quasiparticle, and in the case of the non-Abelian anyons in the Moore-Read state is found to be $e/4$. Therefore, to introduce quasiparticles to $\nu = 5/2$, one can simply shift the filling factor slightly by either detuning the magnetic field or changing the electron density using an electrostatic gate.

2.8 Experimental status of $\nu = 5/2$

2.8.1 Quasiparticle charge

One prediction of both the Pfaffian and anti-Pfaffian models is that the non-Abelian quasiparticles have charge $e/4$. The first observation of quasiparticles with charge $e/4$ at $\nu = 5/2$ were carried out using shot-noise measurements [21]. Since shot-noise is simply the statistical result of current being transmitted stochastically in discrete units, the charge of the carriers appears directly in the formula for its noise spectral density. Additional evidence for charge $e/4$ quasiparticles comes from studies of quasiparticle tunnelling [22] and local compressibility [23].

2.8.2 Spin-polarization

Another property of quantum Hall states that varies from one state to another is their spin polarization. The first integer quantum Hall state, at $\nu = 1$ is fully spin-polarized, since it occurs when only the lower-energy spin branch of the LLL is full. Conversely, the state at $\nu = 2$ is fully unpolarized, since both the up and down spin branches are full. This even-odd pattern holds for the IQHE, but the picture for the FQHE is more complex. At $\nu = 5/2$, both spin-polarized and spin-unpolarized wavefunctions have been proposed. A clear experimental determination of the actual spin-polarization would eliminate certain theoretical descriptions as possibilities. Several attempts have been made to find evidence for the spin polarization by observing the behaviour of the 5/2 energy gap versus magnetic field [24–26]. Of particular interest is the effect of a parallel magnetic field, which tunes the Zeeman energy without affecting the cyclotron energy. However, interpretation of the experimental results is complicated by effects of the finite width of the quantum well, which is comparable to the magnetic length [27].

More recently, multiple groups have performed experiments to measure the spin polarization directly. The most successful technique has been an innovative version of resistively detected NMR in conjunction with fast electrostatic gating [28, 29]. In these studies, the sample is first tuned to a particular filling factor (such as 5/2), and continuous wave RF is applied at a frequency close to the nuclear resonance. Then, a voltage is applied to the gate to bring the sample to another filling factor (such as 2/3), where its resistance is highly sensitive to the nuclear spin. If the RF that was applied while at 5/2 was on resonance, the nuclei will have been partially depolarized and the resistance at the detection state will be different. By repeating this procedure, it is possible to determine the resonant frequency of the nuclei while the electrons are in the 5/2 state. That frequency is proportional to the spin flip energy for the nuclear spin, which will be enhanced if the electrons are spin-polarized and create an additional effective magnetic field. The change in resonance frequency due to spin polarization of the electrons is known as the *Knight shift*. The results of this experiment, performed independently by two different groups, suggest a fully spin-polarized 5/2 state. This is consistent with the prediction of the Moore-Read Pfaffian, and eliminates the 331 state as a possibility.

2.8.3 Tunnelling

Theory predicts that non-Abelian and Abelian states can be distinguished based on the tunnelling rates for quasiparticles through a quantum point contact. Two groups have reported experimental results for this type of study [22, 30], with the most recent results suggesting competition between an Abelian and non-Abelian state, depending on the degree of confinement, with the non-Abelian state being favoured at weak confinement (and, one would therefore assume, in the bulk).

2.8.4 Neutral edge modes

Some of the most challenging and intriguing experiments used to study the 5/2 FQHE involve the detection of neutral edge modes. In both the IQHE and FQHE, charge is transported by chiral edge states. Current can only flow in one direction, either clockwise or counterclockwise, depending on the sign of the carrier charge and the direction of the field. However, theory predicts that there could also be neutral edge modes, which can transport heat but not charge. For example, one can imagine an electron and a hole forming a neutral exciton. Such modes could travel “upstream” - *i.e.* in the opposite direction from charge transport, since they are not affected by the magnetic field. Whether such modes exist or not depends on the wavefunction underlying the particular quantum Hall state, and thus detection (or convincing non-detection) could be used to narrow down the list of candidate wavefunctions for the 5/2 state.

Researchers at the Weizmann Institute have successfully detected neutral edge modes in integer and fractional filling factors, including $\nu = 5/2$ [31]. To do so, they measured shot noise at a particular contact on the sample, while driving current at different contacts. They observed an increase in shot noise at the probe contact, even though no current reached it. This was interpreted as evidence for the flow of heat without charge transport.

2.8.5 Interferometry

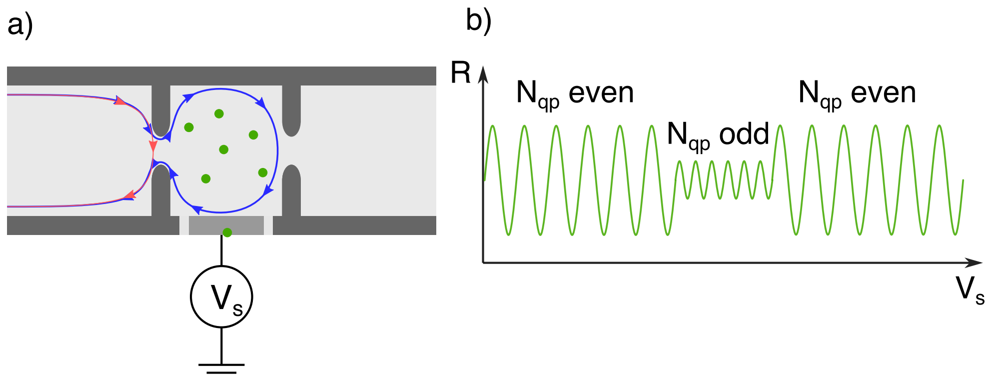

Figure 2.7: a) Fabry-Pérot interferometer for electrons or quasiparticles. The dark grey regions represent electrostatic gates, defining a central region and two quantum point contacts. Changing the side-gate voltage, V_s, changes the area, and therefore the number of QPs (represented green dots) enclosed. b) Simplified cartoon the expected results for such an experiment. Figure based on reference [32].

Perhaps the most direct evidence for non-Abelian anyons would be observation of actual braiding operations. One way to do that is by using an electron (or quasiparticle, in this case) interferometer, analogous to familiar optical interferometers. A cartoon of such a device is shown in Figure 2.7a, where the particles following the red path and the blue path interfere constructively or destructively. Particles traveling around the edge braid around localized particles in the central area, and it has been shown that the periodicity of the resulting interference pattern depends on whether they wind around an odd or even number of non-Abelian anyons [33, 34]. As the side gate voltage is changed, changing the parity of the number of enclosed quasiparticles, one would expect a signal similar to the one shown in Figure 2.7b, with distinct changes in the periodicity of the interference pattern. The experiments by Willett *et al.* [1, 35, 36] have shown promising results, and work in this area is still ongoing.

2.9 Summary

The two-dimensional electron gas in a magnetic field is a rich platform for studying condensed matter physics as it plays host to a hierarchy of increasingly "quantum" phenomena as new highs in sample mobility and lows in temperature are reached. One of the most recent frontiers is the even-denominator $\nu = 5/2$ QH state, which may host non-Abelian anyons that break the fermion/boson dichotomy. The next chapter will introduce measurement techniques that could detect the additional ground state entropy expected in a non-Abelian state. These experiments were originally proposed as a way to avoid the damaging fabrication steps required to build interferometers, as well as reduce complications due to quantum Hall edge physics.

Chapter 3

Entropy detection in the fractional Quantum Hall Regime

One of the holy grails of condensed matter physics is unambiguous detection of non-Abelian (NA) quantum statistics. Ideally, this would involve actually performing braiding operations with the quasiparticles and observing the resulting change in their quantum state. At $\nu = 5/2$, this would mean constructing an interferometer and observing changes in the Aharanov-Bohm periodicity as the number of quasiparticles in the bulk changes between even and odd [37]. Several groups have attempted such studies. While the results by Willett *et al.* [1] provide evidence for such states, independent verification is still lacking. Due to the difficulty of performing actual quasiparticle braiding operations in the 5/2 state, measurement of the bulk entropy has been proposed as an alternative and complementary experimental direction. The entropy may be determined by measuring the thermopower, adiabatic cooling, magnetization, heat capacity and other related quantities. This chapter will provide an overview of these experimental proposals, as well as highlight some of their advantages and limitations.

3.1 Expected non-Abelian entropy of the 5/2 state

In a non-Abelian system, there must be a set of degenerate ground states which are accessible only via braiding operations. The number of such states (or degeneracy, D) is exponential in the number of quasiparticles, according to

$$D = d^{N_{qp}}, \tag{3.1}$$

where d is the so-called quantum dimension and N_{qp} is the number of non-Abelian quasiparticles. For the Moore-Read state, $d = \sqrt{2}$ since the quasiparticles are Ising anyons [12]. Correspondingly, the quasiparticles (if localized) must also have a *non-Abelian entropy*,

$$\mathcal{S}_D = k_B \log D = k_B N_{qp} \log d, \tag{3.2}$$

which is proportional to the number of quasiparticles. In 2009, two different groups proposed experimental schemes that would use the entropy as a signature of an FQH state being non-Abelian [38, 39]. Such experiments would avoid the practical difficulties of fabricating interferometers, as well as the theoretical challenges of understanding the detailed physics of the quantum Hall edge. However, entropy measurements are also non-trivial, especially since the total entropy of the quasiparticles also has a substantial (and, in many regimes, dominant) contribution from other sources. In general, we may break up the total entropy, $\mathcal{S}_{total}$, according to

$$\mathcal{S}_{total} = \mathcal{S}_D + \mathcal{S}_n, \tag{3.3}$$

where $\mathcal{S}_n$ is the normal entropy due to usual excitations of the system. In the next few sections, we will give an overview of various experimental schemes to probe the entropy.

3.2 Thermopower

In metals and semiconductors, the fact that charge carriers also transport heat causes thermal currents, electrical currents, thermal gradients and potential gradients to become interrelated. Thus, resulting *thermoelectric effects* can be used in various configurations. For example, in the Peltier effect an electrical current drives a heat current, cooling one of the terminals of the device. In reverse, a heat current can drive an electric current, which can be used for thermoelectric power generation. In this section, we will consider the voltage that arises in an open circuit due to a thermal gradient. This is known as the *Seebeck effect*, or often simply the *thermopower*.

The Seebeck coefficient is defined as

$$S_{ij} = \frac{qE_i}{\nabla_j T} \tag{3.4}$$

where q is the charge of the carriers, E is the electric field and the i and j subscripts refer to the orientations of the electric field and temperature gradient (x and y in Cartesian coordinates, or r and ϕ in polar coordinates). Note that the transverse Seebeck effect in a magnetic field is sometimes called the Nernst effect, with the Nernst coefficient defined as $N = S_{xy}/B_z$. Equation 3.4 can also be rewritten as

$$S_{ij} = -\frac{\Delta V_i}{\Delta T_j}, \tag{3.5}$$

which relates the voltage measured between two points to the temperature differential across the sample.

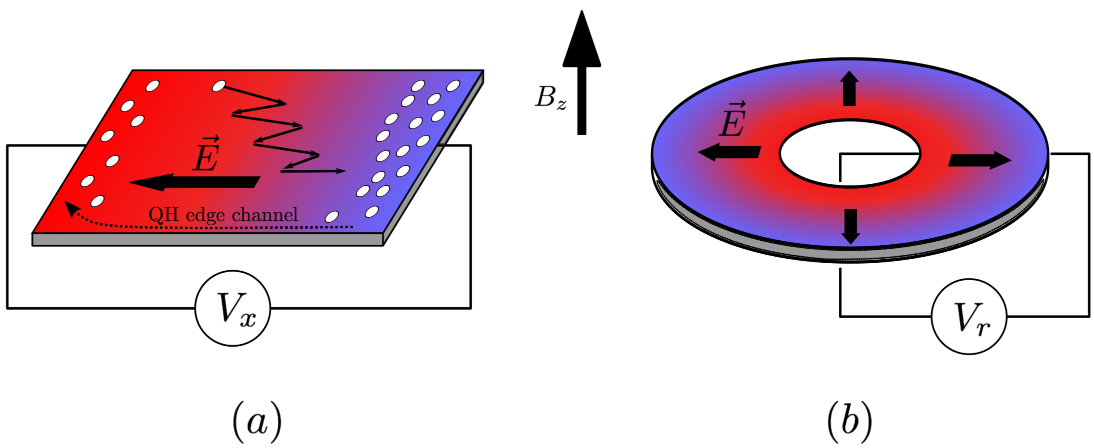

Figure 3.1: a) Seebeck effect in a rectangular 2DEG. A temperature gradient, maintained by an external heater, exerts an entropic force on the quasiparticles (indicated by the zig-zag path): a QP with high kinetic energy from the hot side loses energy when it arrives at a colder part of the sample, and does not have the energy to return all the way to where it started. The net effect is a weighted random walk, tending to move particles to the cold side). They soon build up on the cold side of the sample, setting up an electric field. However, the quantum Hall edge provides an alternative return path "shorting out" the thermopower. b) A radial temperature gradient in a Corbino device causes a radial electric field to develop. However, there is no QH edge, so a larger charge build-up and electric field can be maintained than in the rectangular device.

In a 2DEG, there are two major contributions to S_{ij}: diffusion and phonon drag. In this section, we will focus on diffusion thermopower, which is dominant in the low temperature limit below a few hundred milliKelvin [40]. A cartoon of diffusion thermopower is shown in Figure 3.1a and discussed in its caption. Under certain conditions, the thermopower of a 2DEG is approximately equal to the entropy per quasiparticle. Cooper *et al.* [41] showed that this relation holds for longitudinal thermopower in the quantum Hall regime in the clean limit,

$$S_{xx} = \frac{-\mathcal{S}}{eN_e}, \tag{3.6}$$

while Yang and Halperin [39] later proposed its use for detection of non-Abelian anyons via their excess entropy. In the *Corbino geometry*, shown in Figure 3.1b, the radial thermopower is instead equal to the entropy per quasiparticle,

$$S_{rr} = \frac{-\mathcal{S}}{qN_{qp}}, \tag{3.7}$$

as shown by Barlas and Yang [42]. Since the number of quasiparticles is generally much smaller than the number of electrons, the thermopower is expected to be much larger in the Corbino geometry.

Chickering *et al.* have carried out thermopower measurements at $\nu = 5/2$ and $\nu = 7/3$ at temperatures as low as 20 mK, but were not able to draw firm conclusions as to the existence or non-existence of a non-Abelian entropy contribution [40, 43]. Doing so may require the study to be carried out at even lower temperatures, in order to reduce the contribution of $\mathcal{S}_n$. In Appendix E, I present results of my experimental investigations into measuring thermopower driven by *in situ* Joule heating in the Corbino geometry.

3.3 Detection via Maxwell relations

The Maxwell relations are a set of equations that relate various thermodynamic derivatives. They are derived by considering the mixed partial derivatives of thermodynamic potentials, such as the Gibbs free energy. Since the non-Abelian entropy is proportional to N_{qp}, it would be observable by measuring $(\partial\mathcal{S}/\partial N)_T$. Cooper and Stern [38] noticed that two of the Maxwell relations are of particular interest for this task:

$$\left(\frac{\partial\mu}{\partial T}\right)_N = -\left(\frac{\partial\mathcal{S}}{\partial N}\right)_T \tag{3.8}$$

and

$$\left(\frac{\partial M}{\partial T}\right)_B = -\left(\frac{\partial\mathcal{S}}{\partial B}\right)_T, \tag{3.9}$$

where M is the orbital magnetization. The latter equation is useful due to the flux-like nature of FQH quasiparticles, which creates a direct relationship between ΔB and N_{qp}. An experiment based on equation 3.8 would involve measuring the change in chemical potential of the 2DEG, at constant electron density, while the temperature is changed by a small amount. Equivalently, one could measure the change in electron density at constant chemical potential by using a top gate near the 2DEG as a capacitive charge sensor. One would then use the geometric capacitance to calculate the equivalent change in μ, or, ideally, use a feedback loop to tune the gate voltage and maintain constant electron density in the 2DEG. The required gate voltage would then equal the change in μ due to the applied ΔT. The simpler version of the experiment has been performed in the few Kelvin temperature regime by Kuntsevich *et al.* [44], however substantial effort would be required to adapt it to $\lesssim 100$ mK temperatures due to diverging thermal timescales [43–45]. A serpentine heater deposited on the sample may allow fast enough temperature modulation, but it is still likely to create unwanted thermal gradients within the 2DEG. My initial investigation into a version of the experiment using non-resonant RF heating to quickly modulate the 2DEG temperature is presented in Appendix E.

Similarly, an experiment based on Equation 3.9 would require sensitive measurement of the 2DEG's magnetization as a function of temperature, using a technique such as torque magnetometry. To my knowledge, such an experiment has not been reported in the literature.

3.4 Adiabatic Cooling

Another approach to the entropy, first proposed by Gervais and Yang [46], is to consider the effect of adiabatically adding ΔN quasiparticles to a thermally isolated 2DEG. The question is: how would the temperature of the system change in response? If the process is adiabatic in the classical sense (no heat added) and reversible, we must have $\Delta S = 0$. Therefore, the equation

$$\Delta S = 0 = \frac{\partial \mathcal{S}}{\partial N}\Delta N + \frac{\partial \mathcal{S}}{\partial T}\Delta T \tag{3.10}$$

must be satisfied. Rearranging, and using the relation $C = T\frac{\partial \mathcal{S}}{\partial T}$, we obtain

$$\frac{\Delta T}{\Delta N} = -\frac{T}{C}\frac{\partial \mathcal{S}}{\partial N} \tag{3.11}$$

Since C is always positive, $\frac{\Delta T}{\Delta N}$ immediately provides a probe of the sign of $\frac{\partial \mathcal{S}}{\partial N}$, even if C itself is unknown. In principle, this experiment could be carried out by using either a change in magnetic field or a gate to add and remove quasiparticles. In conjunction with a specific heat measurement, it would provide full information about the dependence of $\mathcal{S}$ on N.

In practice, the difficulty with adiabatic cooling is that it requires thermal isolation of the 2DEG, which means the experiment has to be performed faster than the thermal relaxation timescale. However, changing the quasiparticle number quickly also generates heat within the 2DEG, breaking the adiabaticity requirement. An estimate of the expected achievable temperature change due to the non-Abelian part of the entropy is presented in Appendix D.

3.5 Specific heat

Perhaps the best-known experimental proxy for the entropy is the specific heat, which is the amount of energy required to heat a unit of material by a unit of temperature. However, specific heat is far from ideal as a means to detect $\mathcal{S}_D$, since it probes the temperature derivative of $\mathcal{S}$, while $\mathcal{S}_D$ is *a priori* temperature independent. Nonetheless, it may be possible to detect $\mathcal{S}_D$ via specific heat in a few different ways.

3.5.1 Degeneracy breaking at low temperature

In principle, the non-Abelian ground states are not "true" ground states, their degeneracy being lifted at low enough temperature by terms that are exponential in the separation of their quasiparticles [47]. At low enough temperatures, the degeneracy is expected to break, as illustrated by the red curve in Figure 3.2. The temperature scale where this occurs is $T_d \approx \Delta e^{-l/l_0}$, where Δ is the energy gap of the FQH state, l is the spacing between quasiparticles and l_0 is the characteristic size of the quasiparticles [39]. There is also some evidence from numerical calculations that the 5/2 quasiparticles are very large, with $l_0 \simeq 150$ nm [48], which may lead to T_d being reached within an experimentally accessible temperature range. For example, with $\Delta = 500$ mK, $n_e = 3 \times 10^{11}\,\text{cm}^{-2}$ and B detuned from $\nu = 5/2$ by 5 mT, we would have $T_d = 67$ mK (assuming the 150 nm size estimate). The breakdown of the non-Abelian degeneracy could provide the temperature dependence necessary

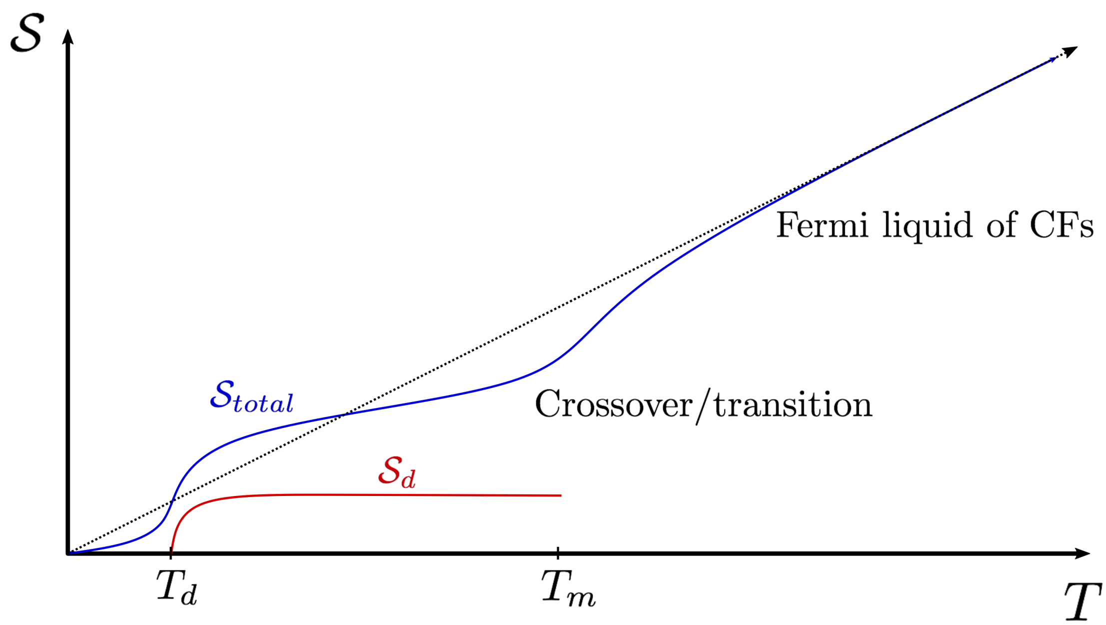

Figure 3.2: Sketch of the expected entropy vs temperature in a non-Abelian quantum system. At the lowest temperature, the NA states are not degenerate, and there is only normal entropy. At some characteristic degeneracy temperature, T_d, the states become degenerate and begin to act as a manifold of non-Abelian ground states, contributing entropy $\mathcal{S}_D$ to $\mathcal{S}_{total}$. Above the melting temperature, T_m, the system undergoes a series of crossovers and/or transitions, such as perhaps Wigner crystal melting, breakup of the paired MR state and formation of a Fermi liquid of composite fermions. In the Fermi liquid state, the entropy is, in principle, linear and extrapolates to zero (dotted line).

for the non-Abelian entropy to influence the specific heat.

3.5.2 Integration to known high temperature behaviour

The entropy of the system can be found from specific heat, up to a constant of integration, using the equation

$$\mathcal{S}(T) = \mathcal{S}(T_0) + \int_{T_0}^{T} \frac{C}{T'} dT', \tag{3.12}$$

where C is the system's heat capacity (the extrinsic version of specific heat). If one could determine $\mathcal{S}$ at one temperature T_0, one could use measurements of $C(T)$ to find $\mathcal{S}$ at other temperatures. For example, one could measure thermopower at high temperature, and C over a range of T that includes much lower temperatures with different physics. Alternatively, one could use more theoretical arguments. The third law of thermodynamics says that $\mathcal{S} = 0$ at $T = 0$. In practice, T_0 could be chosen such that $\mathcal{S}(T_0) \ll S(T)$ and the error introduced into the determination of $\mathcal{S}(T)$ is negligible. Finally, it may be possible to find $\mathcal{S}$ in absolute units at high temperature, when the CF's form a Fermi liquid. The entropy of a Fermi liquid is known to be linear with an intercept of zero, as illustrated in Figure 3.2. Linear behaviour over a wide range of T could therefore be used to determine $\mathcal{S}$. This latter approach has been successfully used in studies of superfluid Helium-3 [49].

3.6 Summary

By measuring the entropy *vs* number of quasiparticles in a fractional quantum Hall state, it is, in principle, possible to determine whether it is non-Abelian. This chapter has discussed a number of experimental techniques to access the entropy. However, all of these measurements must probe the bulk quasiparticles to be successful, whereas usual transport techniques tend to be dominated by edge physics. Chapter 5 will introduce the Corbino sample geometry, which will help to mitigate this problem and improve the sensitivity of experimental measurements. First, however, we will take a look at the measurement apparatus and instrumentation in the next chapter.

Chapter 4

Instrumentation and Methods

Observation of subtle quantum phenomena close to absolute zero requires both an ultra-low temperature refrigerator and an array of sensitive measurement equipment and techniques. In this chapter, I will introduce the physical apparatus used to perform the measurements presented in the rest of the thesis.

4.1 Refrigeration

4.1.1 Dilution Refrigerator

Our samples are cooled using the workhorse of low-temperature physics: the *dilution refrigerator*. In order to reach temperatures as low as 17 mK, several cooling stages are employed, as shown in Figure 4.1. Our system is a so-called wet refrigerator, meaning that the cooling stages are located within a vacuum can that is immersed in liquid helium to reach 4.2 K. The topmost stage of the cryostat, called the 1 K pot, is cooled by evaporative cooling of ^{4}He. A small pipe connects the 1 K pot to the helium bath, and an external vacuum pump pulls the helium out. Since higher energy atoms preferentially leave the liquid, the remaining atoms have a lower average kinetic energy and temperature (typically around 1.5 K during normal operation).

Below the 1 K pot, the remaining stages comprise the *dilution unit* itself. The *still* is cooled by evaporative cooling of ^{3}He, which has a much lower boiling point than ^{4}He and reaches a few hundred mK. The source of ^{3}He is actually the lowest stage of the refrigerator: the mixing chamber. In the mixing chamber, both ^{3}He and ^{4}He coexist, but phase-separate due to their quantum mechanical properties and distinct quantum statistics. By pulling ^{3}He from the ^{3}He rich phase to the ^{3}He poor phase, further cooling is achieved. The system operates in a closed loop,

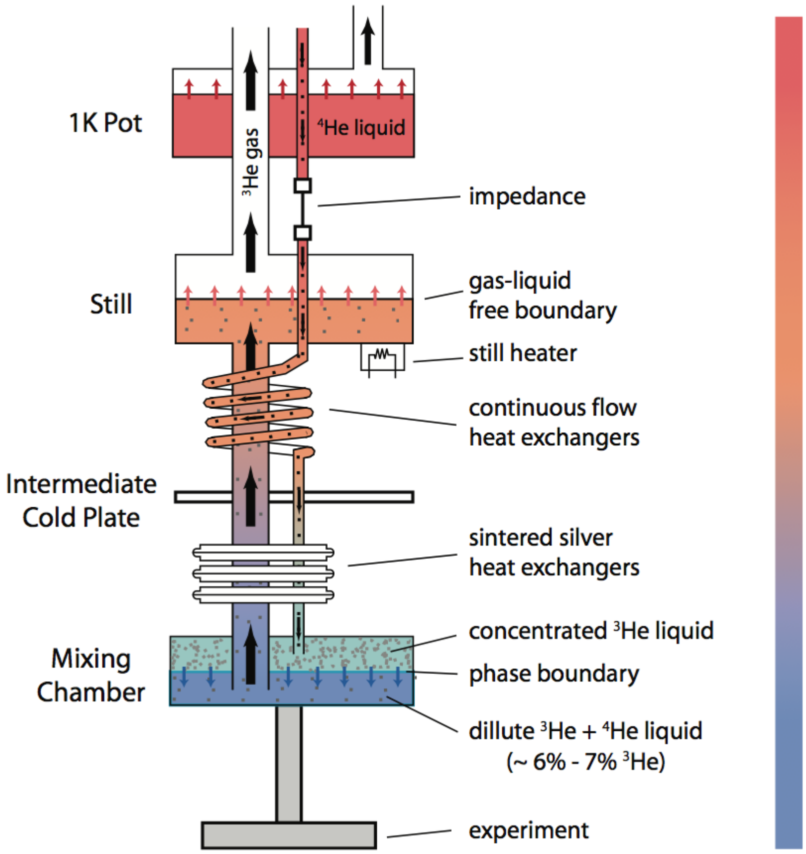

Figure 4.1: Schematic diagram of a dilution unit showing the multiple cooling stages and their respective temperatures. Figure reproduced with permission from reference [8].

whereby ^{3}He is pumped out of the still, pressurized, and returned to the mixing chamber via an impedance (to ensure a slow return rate) and a series of pre-cooling heat exchangers. A more detailed description of the refrigerator is available in Cory Dean's PhD thesis [8].

4.2 Cooling Electrons

4.2.1 General considerations

While the dilution refrigerator itself is a commercially available and well-established piece of technology, bringing the electrons within the sample to the same temperature as the mixing chamber presents a notoriously difficult challenge. To perform electrical measurements, there must be wires passing from the sample at base temperature, through each stage of the refrigerator, and ultimately to the instrumentation at room temperature. Special precautions must therefore be taken to prevent heating the electrons by thermal conduction or Joule heating. These two mechanisms are discussed below.

Thermal conduction

Good electrical conductors are usually also good thermal conductors at low temperature, where electrons are more important than phonons in thermal transport. To avoid conducting heat to the sample, we can use superconducting wires, in which electrons do not carry heat. Alternatively, we can use thin wires made of alloy materials such as Manganin and NiChrome which have relatively low thermal conductivity and low, but sufficient, electrical conductivity compared to pure metals such as copper and silver.

Joule heating

Any current flowing through the sample will generate heat in the sample according to Joule's law: $P = I^2R$. This is particularly problematic if the electron-phonon coupling is weak (as it is at low temperature), and this power cannot be efficiently dissipated. Stray currents may arise from ground loops, capacitive and emf pickup in the wiring, microphonics and even Johnson noise in the room temperature resistors included within the measurement circuit. To mitigate this, filters may be installed to limit any frequencies outside of the desired measurement bandwidth from reaching the refrigerator, and the room temperature part of the circuit should be carefully designed to prevent noise currents from arising in the first place.

4.2.2 Our wiring design

In order to satisfy the requirements of our experimental setup, different types of wires are used at different stages of the cryostat. Between the top of the cryostat (at room temperature) and the 1 K pot, we use Manganin wires, which have relatively poor thermal conductivity but acceptable electrical conductivity. Between the 1 K pot and the mixing chamber, we use CuNi-clad monofilament NbTi superconducting wires. Since a superconductor does not carry heat and CuNi is a poor thermal conductor, these wires reduce the heat load reaching the mixing chamber. The wires are epoxied to copper heatsink blocks at each stage to thermally anchor them. From the mixing chamber to the sample stage, we use silver wires. These wires pass through a pressed silver powder filter which both provides a thermal contact and filters out microwave frequencies (via dissipation of eddy currents induced in the silver grains). Certain headers also include lowpass RC filters with a cutoff frequency of around 1 kHz, which are suitable for low frequency measurements. In addition to filtering, the capacitors in the RC filters also act as efficient heatsinks, since by design a capacitor features two plates with large area separated only by a very thin insulating layer. All wires are arranged as individually shielded twisted pairs. However, as will be discussed later it is often impractical to use the two wires of the pair as source and return, since capacitive coupling between them would be problematic.

All wires and filters used in this thesis were the same as described in Cory Dean's PhD thesis [8], with no modification. The sample wiring diagram is reproduced in Appendix B.

4.3 Low Noise measurement

4.3.1 Lock-in amplifier

A lock-in amplifier is a powerful tool that can be used to accurately measure one specific frequency component of a signal. Mathematically, it can be thought of as a one component Fourier transform of the signal. Internally, it multiplies the signal with a reference sine wave, as shown in Figure 4.2 and integrates the result. Unlike a true Fourier transform, however, it integrates over only a finite integration window using a low pass filter. To detect both in-phase and out-of-phase signals, two lock-in circuits are required: one for each phase. Many modern lock-ins include both circuits within a single instrument for convenience. The basic lock-in equations are:

$$X(t) = 2\int_0^\infty \sin(\omega_{ref}t) \cdot v_{sig}(t-t')I(t')dt' \tag{4.1}$$

$$Y(t) = 2\int_0^\infty \cos(\omega_{ref}t) \cdot v_{sig}(t-t')I(t')dt', \tag{4.2}$$

where $I(t')$ is the normalized impulse response function of the low-pass filter, and X and Y are the in-phase and out-of-phase voltage respectively. If the input signal is simply $v_{sig} = v_0 \sin(\omega_{ref} t)$, the resulting outputs are

$$X(t) = v_0 \int_0^\infty (1 - \cos(2\omega_{ref} t)) \cdot I(t')dt' \tag{4.3}$$

$$Y(t) = v_0 \int_0^\infty (\sin(2\omega_{ref} t)) \cdot I(t')dt'. \tag{4.4}$$

If the integration time (*i.e.* the width of $I(t)$) is large compared to π/ω, this reduces to $X(t) = v_0$ and $Y(t) = 0$. The output for an input at any other frequency approaches zero for sufficiently long integration time. The lock-in is, therefore, an extremely high-Q tuneable bandpass filter. Basically, signals at the frequency of interest have been transformed to DC, where they are easily filtered using a simple low pass filter. All other frequencies are transformed to other AC frequencies and can be removed by the low pass filter.

Older analog lock-in amplifier designs use sophisticated analog electronics to perform the calculation, while newer digital models digitize the signal, multiply by the (digital) reference and apply digital filters to the result. In some low temperature measurements, analog lock-ins are still used in order to avoid electrical interference which is unavoidably emitted by digital models. Such noise could potentially reach the sample, either heating it up or simply degrading the signal-to-noise ratio of the measurement. In our setup, I found that removing digital instrumentation from the Faraday cage surrounding the refrigerator did indeed lower the observed noise, as discussed later in section 4.4.4.

Advantages

In low-temperature physics, lock-in amplifiers are often used to avoid the problems of purely DC measurement. DC measurements are typically very noisy, due to thermoelectric voltages, diverging 1/f noise, and thermal drift in components such as resistors (both within the instruments and in the external circuitry). By instead using low frequency excitation and detection, we can prevent slowly varying voltages from affecting the measurement.

Lock-in amplifiers are also an ideal tool for harmonic and heterodyne detection. By detecting at multiples of the excitation frequency, or the sum (or difference)

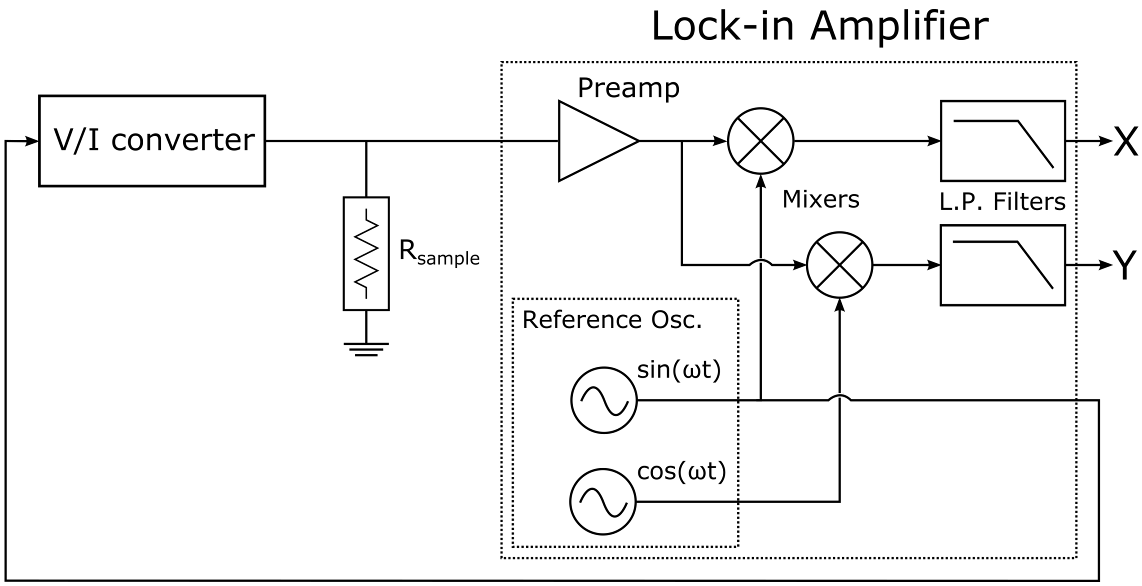

Figure 4.2: Simplified schematic for a Lock-in amplifier and basic measurement. The reference oscillator generates a sine wave voltage output, which is converted to a current by the V/I converter and applied to the sample. The voltage across the sample is amplified by a preamplifier before being split and multiplied by internal sine and cosine reference signals. The output from these is low pass filtered to obtain the X and Y components as DC voltages. In modern lock-ins, the input signal is digitized after the preamplifier and all other parts are implemented digitally.

between multiple excitation signals, it becomes straightforward to probe nonlinear effects with high sensitivity.

Pitfalls

Because a lock-in requires a reference signal at the frequency of interest, there is an internal oscillator generating a sine wave at that frequency. If the instrument or sample is improperly grounded, that signal may couple to the measurement side of the circuit, leading to a persistent background offset in the lock-in measurement. I observed this problem in some measurements when the SR830's digital output port was connected to an optoisolator. While the optoisolator serves its function of electrically isolating the instrumentation from the computer being used to record the data, it does also provide additional ground paths for the instruments connected to it via the shields of their signal cables and its grounded chassis. To break the ground loop, one can instead connect the analog X and Y outputs of the SR830 to a DC voltmeter (such as Agilent A34401) and connect that to the optoisolator to be read by the computer.

4.3.2 Voltage measurement and voltage preamplifiers

An ideal voltage detector would measure the potential difference between two points in a circuit without any current passing through the detector (*i.e.* it would have infinite input impedance). For AC voltages, the main measurement tool we use is the voltage preamplifier. Voltage preamplifiers are characterized by several key parameters. The most obvious is the *gain* - the ratio of the output voltage to the input voltage. A large gain boosts the signal above the level of the noise added by later instrumentation stages, however, excessive gain may lead to clipping of the signal if the output voltage becomes too large. This is especially problematic if the desired signal is smaller than extraneous signals. In this case the signal should only be partially amplified prior to application of filters. In the SR830, the tradeoff between applying more gain at the internal preamplifer (for low noise) or after the filter (for rejection of large off-frequency background signals) is adjustable by changing the "dynamic reserve."

The next key figure, for our purposes, is the equivalent input voltage noise, $\tilde{v}_{in}$. This is defined as the measured RMS noise at the output, divided by the gain. Note that it might not actually be physical noise at the input itself: it can have contributions from any component in the preamplifer circuit, including the power supply. In general, $\tilde{v}_{in}$ is frequency dependent, having a $1/f$ dependence below some corner frequency f_c and a flat dependence above that. One also needs to pay attention to the input impedance of the preamplifier, which must be much larger than the sample impedance in order to approximate the "infinite input impedance" approximation. Other important parameters are: linearity, bandwidth and flatness, stability, and input bias voltage.

Finally, it should be noted that preamplifiers may either be single-ended ($v_{out} = Gv_{in}$) or differential ($v_{out} = G(v_{in2} - v_{in1})$). In practice, the output signal consists of not only the amplified difference between the inputs, but also a component of the sum of the two (the common mode voltage). This can be a problem if, for example, both inputs pick up a voltage at 60 Hz due to power line hum. A differential preamplifier's ability to reject common-mode signals is specified by its *common mode rejection ratio* (CMRR).

4.3.3 Current measurement

An ideal current detector would accurately measure the current passing through it, without any voltage drop across the detector (zero impedance). We will consider two current measurement methods: current preamplifiers and voltage measurement across a sense resistor.

Current preamplifiers

The gain, or transimpedance, of a current preamplifier is the ratio of its output voltage to the input current. As in the voltage preamplifier, the purpose of a current preamplifier is to boost the input signal to a level such that noise added by later signal processing stages is negligible. Its noise performance may be characterized by the equivalent input current noise, i_{in}, which is defined similarly to v_{in}.

One nice feature of current preamplifiers is that they actively maintain the input at virtual ground. Thus, the sample acts like it is actually grounded, rather than at a finite voltage equal to iZ_{in}. On the other hand, current preamplifiers tend to be more difficult to use than their voltage counterparts. Many models, including the SR570, have a non-negligible input bias current, meaning they constantly drive a small current into the sample. Another issue with current preamplifiers is that their noise performance tends to degrade badly with increasing input cable length, due to the capacitance of the wires to ground. In fact, the state-of-the-art *Femto* line of preamplifiers are not suitable for many low temperature applications, since there are always a few meters of wiring between the sample and the preamplifier. The SR570 made by *Stanford Research Systems*, which was used in measurement setup B (see below), is relatively immune to long input wires, making it more suitable for low-temperature measurements.

Voltage preamplifier + sense resistor

It is also possible to measure current by using a voltage preamplifier to measure the voltage drop across a resistor. This scheme has some advantages over using a current preamplifier, in that it avoids the problem of injecting an offset bias current into the sample (since JFET preamplifiers have negligible bias current) and is less affected by capacitance than most commercial current preamplifiers. The main drawback of this scheme is that the resistor does not provide a "virtual ground." To have the sample truly grounded, it would be possible to place the sense resistor in

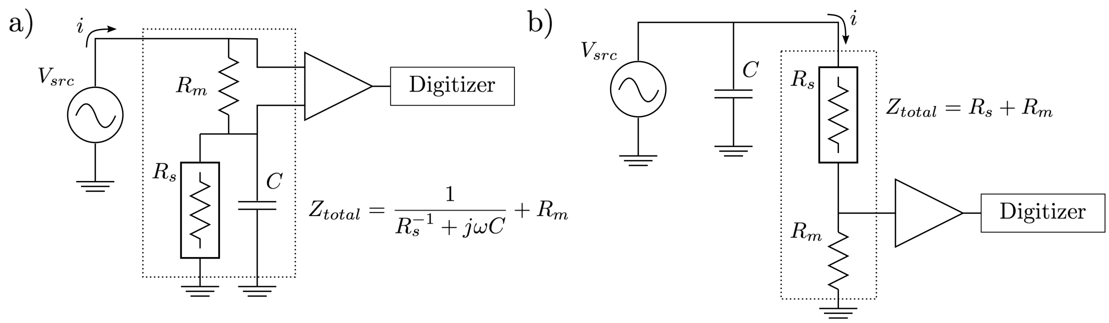

Figure 4.3: Two different arrangements for measuring current with a sense resistor, R_m. The sample is represented by R_s and stray capacitance of the wiring by C. In each case, the measured current is given by $i = V_{src}/Z_{total}$, where Z_{total} is the total impedance of the components within the dotted rectangle. a) Sense resistor between the voltage source and the sample: C contributes to the measured impedance. b) Sense resistor between the sample and ground, eliminating C from the measurement.

the input arm of the circuit and use a differential preamplifier to measure the voltage drop across it as shown in Figure 4.3a. However, in that case we would measure an impedance, Z_{total} that includes any stray capacitance to ground. Conversely, by placing the resistor between the sample and ground, as in Figure 4.3b, the stray capacitance forms a separate current arm and does not contribute to Z_{total}. Note, however, that crosstalk between the "input" and "output" sides of the circuit is still possible via mechanisms such as stray capacitance, mutual inductance, RF and ground loops.

4.4 Experimental configurations

4.4.1 Measurement setup A

For a basic quantum Hall measurement in the Hall or van der Pauw geometry, it is practical to apply a fixed current to the sample and measure the resulting voltage. An example of such a measurement is shown schematically in Figure 4.4. The current source is simply composed of a voltage source and a very large resistance ($R_{source} \gg R_{sample}$). The current through the sample is then given by V_{source}/R_{source}. The voltage between two points at the sample can be measured either at the same contacts (for a two point measurement) or other contacts (for a four point measurement).

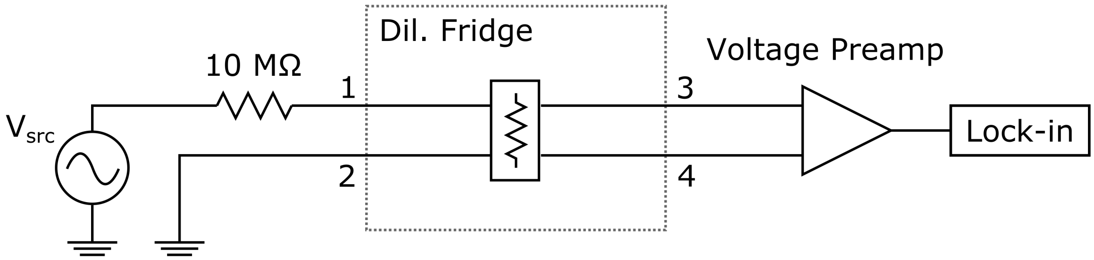

Figure 4.4: Basic 4 point measurement scheme for Hall or VdP geometry.

Bandwidth considerations

In all of our thermal relaxation time measurements, the maximum relevant frequencies are below 1 MHz. At that frequency, the wavelength of electromagnetic waves is 300 m, which is much larger than the length of the wires in our apparatus. Therefore, we do not have to consider the effects of reflection and standing waves (*i.e.* impedance matching) in the circuit, and can instead perform a simpler low-frequency analysis. The bandwidth of our measurement is then set either by the designed bandwidth of the measurement instrumentation, or the RC-time constants built into the circuit. The main source of capacitance is the stray capacitance between the long wires and ground (except on those wires where RC filters are deliberately introduced, which are used only for low frequency measurements). The measured capacitance to ground is 2 nF per wire if the sample is connected to the breakout box on the rack, and 0.6 nF if measured directly at the top of the cryostat. In Figure 4.4, wires 2, 3, and 4 all have stray capacitance, but their most direct resistive path to ground is through the sample itself. Since the two point resistance of the sample (in Hall or van der Pauw geometry) is roughly the Hall resistance, or 10 kΩ at $\nu = 5/2$, the measurement bandwidth is limited to

$$f_{BW} = \frac{1}{2\pi RC} = \frac{1}{2\pi \times 10\,\mathrm{k\Omega} \times 0.6\,\mathrm{nF}} = 27 \text{ kHz} \tag{4.5}$$

This bandwidth is far too low for the measurements discussed in Chapter 7, making this measurement scheme unsuitable for those experiments. The situation would be even worse in the Corbino geometry, which has a significantly higher two-point resistance in the MΩ range.

4.4.2 Measurement setup B: two-point using a current preamplifier

In the Corbino geometry, the sample has only two contacts and a large magnetoresistance (over 100 kΩ, diverging beyond GΩ in IQH states). If the previous circuit were used, the voltage across the device would tend toward V_{in} in IQH states. Additionally, we are interested in the sample's conductance, rather than its resistance. For these reasons, it makes more sense to apply a fixed voltage and measure the resulting current. The schematic for this setup is shown in Figure 4.5.

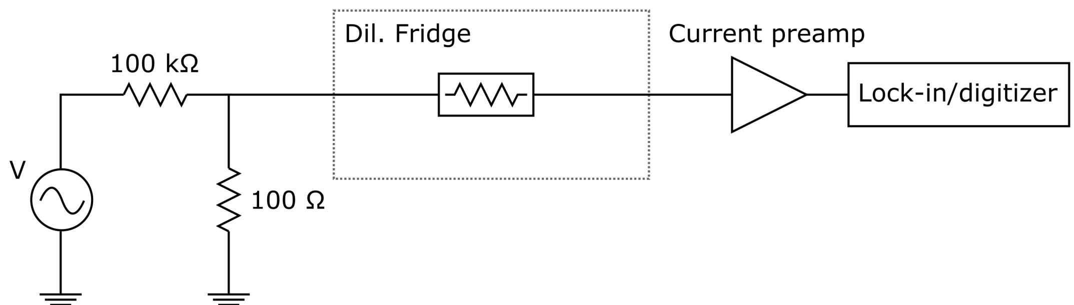

Figure 4.5: Basic 2 point conductance measurement scheme for Corbino geometry.

Bandwidth considerations

In this case, the RC-limited bandwidth is set by the 100 Ω resistor on the input side and the input impedance of the preamplifier on the output side. Using the 10^6 gain setting on the SR570 current preamplifer, the input impedance is also 100 Ω. Therefore, the bandwidth would be 2.6 MHz, however the SR570 is limited to only 200 kHz bandwidth on this setting. Higher bandwidth is achievable by lowering the gain, but this comes at the expense of significantly higher input noise (60 pA/$\sqrt{\text{Hz}}$ for 800 kHz bandwidth, compared to 2 pA/$\sqrt{\text{Hz}}$ for 200 kHz bandwidth). Some of my early measurements of thermal relaxation times in high filling factor IQH states were performed using this measurement scheme, and 200 kHz was just barely adequate. In Chapter 7, higher bandwidth was required, and a different measurement circuit had to be used.

4.4.3 Measurement setup C: 2-point using a sense resistor

To overcome some of the problems associated with using a dedicated current preamplifier, we can instead insert a resistor into the current path, measure the voltage drop across it, and calculate the current using Ohm's law. Figure 4.6 shows such a measurement scheme, with the sense resistor placed between the sample and ground. The sense resistor could, alternatively, be placed at the input side of the circuit, between the voltage divider and the sample. However, as discussed in 4.3.3, in that case it would detect the total current entering the refrigerator, including current flowing into the parallel path to ground formed by the stray capacitance between the input wiring and ground. At 100 kHz, the impedance of this stray capacitance is roughly $|Z| = 1/\omega C = 1.6\,\text{k}\Omega$, which is much smaller than the sample impedance. Therefore, the contribution to the signal due to changes in the conductance of the sample would be tiny relative to the large background.

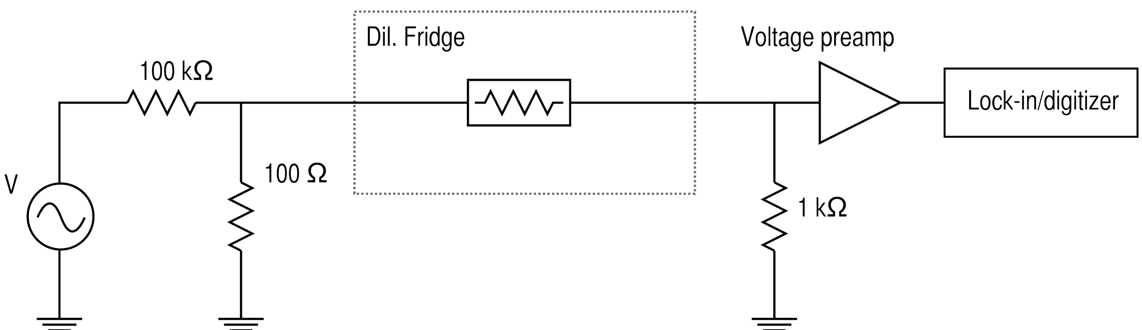

Figure 4.6: Basic 2-point conductance measurement scheme for Corbino geometry.

The effective current noise in this scheme is given by the effective voltage noise at the preamplifier input, divided by R_{sense}.

$$\tilde{i}^2 = \frac{\sqrt{\tilde{v}_{in}^2 + 4k_BTR_{sense} + \tilde{v}_{ext.}}}{R_{sense}}, \tag{4.6}$$

where $\tilde{v}_{in}$ in the preamplifier's equivalent input noise and $\tilde{v}_{ext.}$ is noise due to external interference (ground loops, emf pickup, microphonics etc.). Accordingly, it is always better, in terms of i_n, to increase the value of R_{sense}, even when its Johnson noise becomes the dominant noise source. In practice, R_{sense} was chosen based on the required measurement bandwidth. Using $R_{sense} = 1\,\text{k}\Omega$ and the SR560 preamplifier ($v_{in} = 4\,\text{nV}/\sqrt{\text{Hz}}$), the current noise is $5.7\,\text{pA}/\sqrt{\text{Hz}}$. This is worse than the 2 $\text{pA}/\sqrt{\text{Hz}}$ noise listed on the SR570 manufacturer's specficitations, however the achievable bandwidth is higher and there is no input bias current.

Bandwidth considerations

For this circuit, the bandwidth at the input is the same as it is in setup B, 10 MHz. On the output side, the bandwidth is set by the 1 kΩ resistor, and is 265 kHz (corresponding to a time constant of 0.6 μs). This value was chosen as a tradeoff between signal-to-noise ratio (SNR) and bandwidth.

4.4.4 Measurement setup D: lower noise 2-point using a cooled sense resistor

The actual voltage noise measured in setup C was found to be around 20 nV/$\sqrt{\text{Hz}}$, which is higher than the expected 5.7 nV/$\sqrt{\text{Hz}}$ due to the combination of Johnson noise in R_{sense} and the SR560's input noise of 4 nV/$\sqrt{\text{Hz}}$. The additional noise arises due to the presence of numerous digital instruments on the equipment rack, which are both located inside the Faraday cage and strongly coupled to the refrigerator. An example of the problem can be seen in Figure 4.7. Panel (a) shows a nearly flat spectrum up to the preamplifier's bandwidth cutoff frequency of 1 MHz. The noise level of 0.5 mV_{rms} corresponds to about 6 nV/$\sqrt{\text{Hz}}$ equivalent input noise. However, when the Lakeshore 370 is turned on, as in panel (b), there is much more noise above 300 kHz, peaking at 900 kHz. This noise is particularly problematic, since it lies in the frequency range of interest for the thermal relaxation time measurements in Chapter 7.

With all instrumentation either turned off or moved out of the Faraday cage, the voltage noise is limited by the combination of the preamplifier and the sense resistor. The NF LI-75A preamplifier has lower noise ($\tilde{v}_{in} = 2\,\text{nV}/\sqrt{\text{Hz}}$), than the SR560 ($\tilde{v}_{in} = 4\,\text{nV}/\sqrt{\text{Hz}}$), although it tends to be less able to reject external noise than the latter. In a "quiet" Faraday cage, it does indeed meet specifications and lower the measured noise. The new limiting factor is then Johnson noise in the 1 kΩ sense resistor. This can be reduced from 4.1 nV/$\sqrt{\text{Hz}}$ to 2.1 nV/$\sqrt{\text{Hz}}$ by immersing the resistor in a liquid nitrogen bath. Using the full setup shown in Figure 4.8, measurements with just 3 nV/$\sqrt{\text{Hz}}$ noise level were achievable.

Lower noise may still be achieved by cooling the sense resistor to 4 K and using one of the few preamplifiers that claim even lower input noise levels (*Signal Recovery*

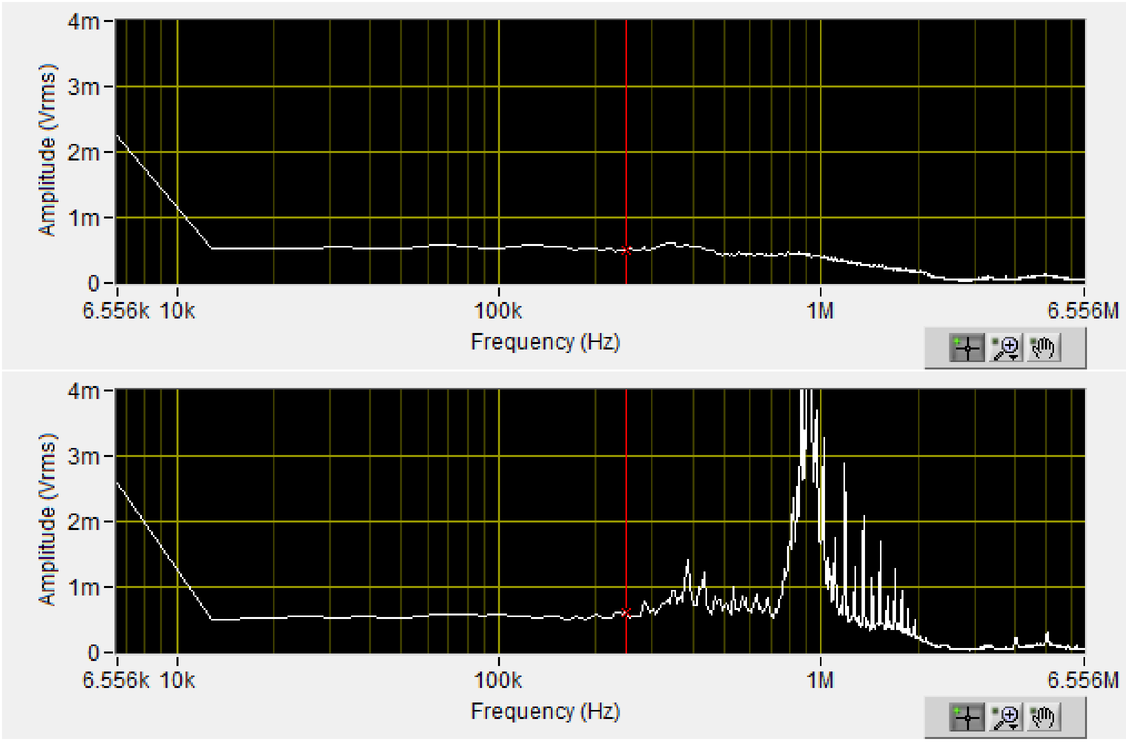

Figure 4.7: Example noise spectra when measuring the voltage across the sample. (A) Spectrum with all instruments within the shielded room turned off, except for the preamplifier. The digitizer (Zurich Instruments HF-2 lock-in) is located outside of the Faraday cage. (B) Identical setup to A, but with the Lakeshore 370 resistance bridge turned on.

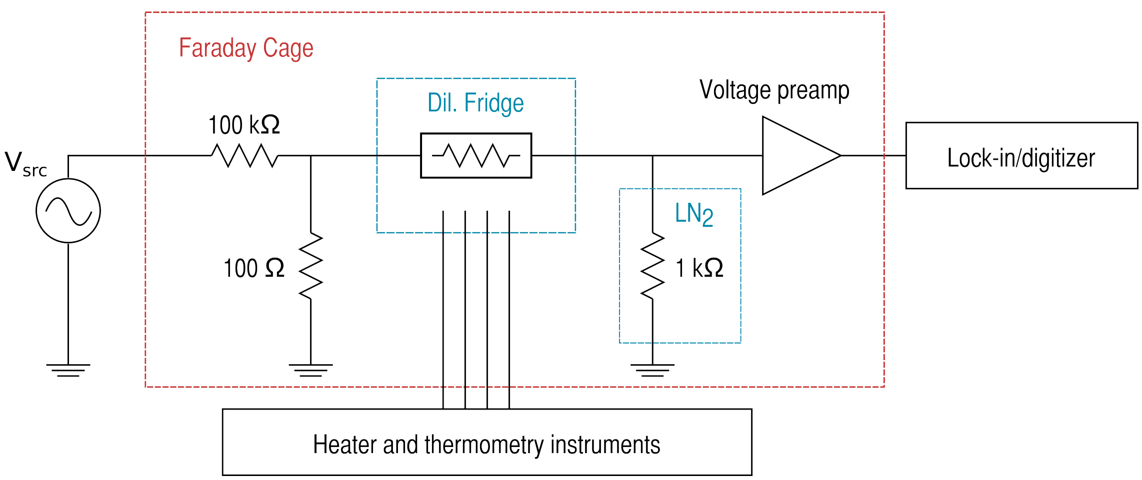

Figure 4.8: Basic 2 point conductance measurement scheme for Corbino geometry.

5184 and *NF* SA series, for example). In order to achieve an even higher signal-to-noise ratio, one could use a cryogenic preamplifier or detect the current using a superconducting quantum interference device (SQUID).

4.5 Summary

To obtain thermal relaxation data, it is necessary to set up a measurement scheme with low noise but also sufficient bandwidth. Our setup has just barely enough bandwidth for the experiment. In practice, we are able to measure conductance transients with time constants very close to the electrical RC time, by carefully examining the assymmetry of the square wave response waveform (turning on bias vs. turning off bias). The actual square wave response also differs from a simple RC response due to the inductance of the wiring. The actual response data, as well as the data processing steps required to make sure we isolate the conductance transient, are described in Chapter 7.

Chapter 5

Fractional quantum Hall effect in the Corbino geometry

One of the key concepts in both mathematics and physics is topology; that is, that some properties of a physical or abstract object are determined by very general characteristics, such as its number of edges, surfaces, holes and the connectedness between them, rather than specific geometric details. This chapter discusses the quantum Hall effect in samples with an unusual topology, the Corbino disk, which features only two contacts that are not connected by any edges. We will begin with a brief historical and theoretical overview of the Corbino geometry, followed by a discussion of sample characterization and transport measurements in the FQH regime. Finally, we will revisit an old idea: that the value of the y-intercept of an Arrhenius plot of conductance in a FQH state is related to the fractional charge of the quasiparticles. Intriguingly, this model seems to hold in the first Landau level, but not in the more exotic second Landau level.

5.1 Topology and the Corbino Geometry

A classic example of topology is the donut, which is, in some sense, the same as a mug with a handle: both are three-dimensional objects formed by a single surface punctured by a single hole. In practice, the two objects have nothing in common despite their topological similarity. Knotted strings provide a more useful example: a string with a slip knot is equivalent to an unknotted string, since one can be deformed to the other with a single tug, while a proper knot cannot be untied without letting go of one end of the string. Although the knot and the slip knot appear to be similar, they are topologically distinct and therefore have very different practical applications.

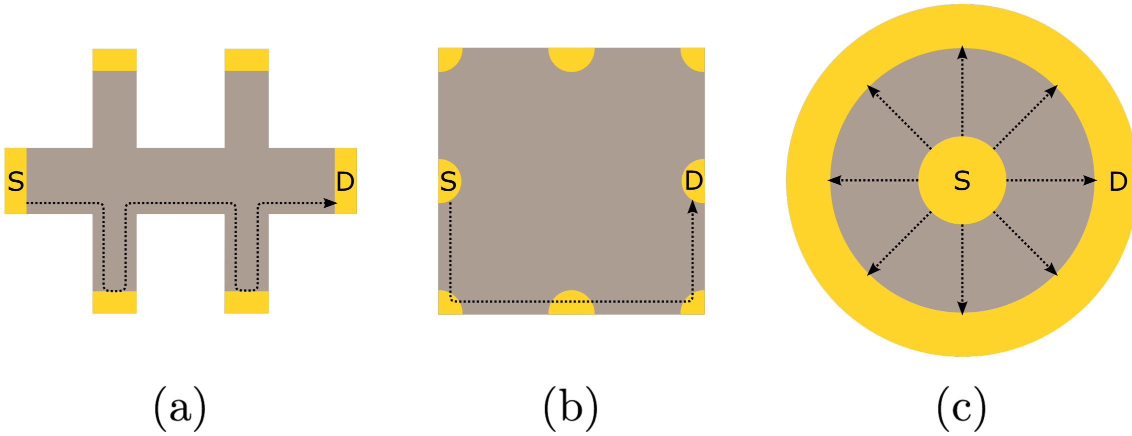

Figure 5.1: a) Hall, b) van der Pauw and c) Corbino geometries, showing current paths (dashed arrow) from source (S) to drain (D). The grey regions represent the 2DEG, while the yellow regions represent the ohmic contacts.

In the same way, the Hall bar and Van der Pauw (VdP) samples often used in quantum Hall experiments are topologically identical: they are both single 2D objects with a single outer edge and no holes, as can be seen in panels (a) and (b) of Figure 5.1. Therefore, the results of electronic transport measurements are the same for both (up to some geometric factors, and possible mixing of R_{xy} and R_{xx}), and are dominated by edge state conduction in the QH regime. In this chapter, we will consider the Corbino geometry, which consists of an annulus with an inner and outer contact, as shown in Figure 5.1c. The Corbino disk is topologically distinct from the other two geometries, since it has just two contacts that are not connected by any edges. As such, current in the Corbino geometry cannot be carried by edge states, unlike in the Hall and VdP geometries. In the IQHE and FQHE, the conductance between the contacts vanishes instead of the resistance as in the other two cases, since the current is forced through the bulk insulating region rather than along the dissipationless edge modes. For this reason, the Corbino geometry provides an excellent platform to study what happens in QH states far from the edge of the sample.

5.2 History of the Corbino geometry

The Corbino effect was first reported in 1911 by Italian physicist Orso Mario Corbino [50]. He noted that when a voltage is applied between the inner and outer rims of a punctured disk of conducting material in a perpendicular magnetic field,

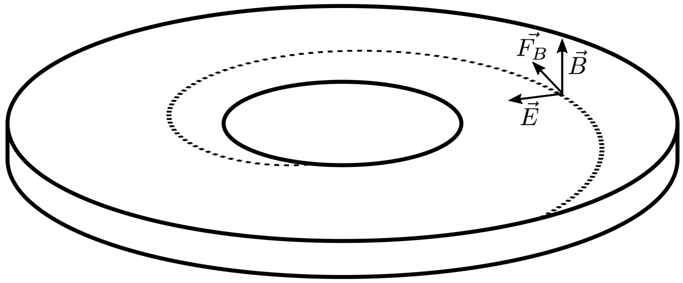

Figure 5.2: Spiral current path in a Corbino disk exposed to a perpendicular magnetic field.

the resulting current will travel in a spiral path due to the Lorentz force (as shown in Figure 5.2). Since the current path is much longer than the direct one that would be followed in the absence of a B-field, the resistance between the two edges is enhanced even if the intrinsic resistivity of the material itself does not vary with magnetic field.

Around 1960, the Corbino disk attracted attention due to the realization that the tangential component of the spiral current path will itself generate a perpendicular magnetic field, which will in turn affect the sample [51–54]. It was thought that the nonlinear effect of this self-feedback phenomenon could be used to build a practical rectifier or even an amplifier. Of course, that technology was never developed, due to the rapid development of silicon-based semiconductor electronics.

The Corbino geometry once again became relevant with the discovery of the IQHE in 1980 [7]. Very early on, Laughlin realized the importance of topology in the IQHE and used a variant of the Corbino geometry in his 1981 theory paper on the subject [55]. Since then, it has occasionally been used by both theorists and experimentalists to distinguish between bulk and edge effects in the IQHE and FQHE.

5.3 Conductance in the Corbino geometry

Conventionally, quantum Hall studies are performed using Hall bar samples. The reason for this is that it allows for independent measurement of the Hall (R_{xy}) and longitudinal (R_{xx}) components of the resistance. As previously discussed, these two components show strikingly different behaviours. While R_{xx} exhibits SdH oscillations, ultimately approaching zero resistance in QH states, R_{xy} exhibits a linear magnetic field dependence with the signature well-quantized plateaus of the quantum Hall effect. While these two phenomena have led to our understanding of IQH and FQH physics, both are signatures of the formation of 1D dissipationless edge channels. Let us now take a look at transport between two contacts that are not connected by any edges, in the Corbino geometry.

5.3.1 Total resistance between the contacts

Interestingly, the resistance between the two contacts of a Corbino device is proportional to $1/\sigma_{xx}$, rather than ρ_{xx}. Recall from Chapter 2, that $\sigma_{xx} \propto \rho_{xx}$. Therefore, the *conductance* in Corbino looks a lot like the *resistance* in a Hall bar. We can calculate the total resistance, R, between the two contacts by first consider-

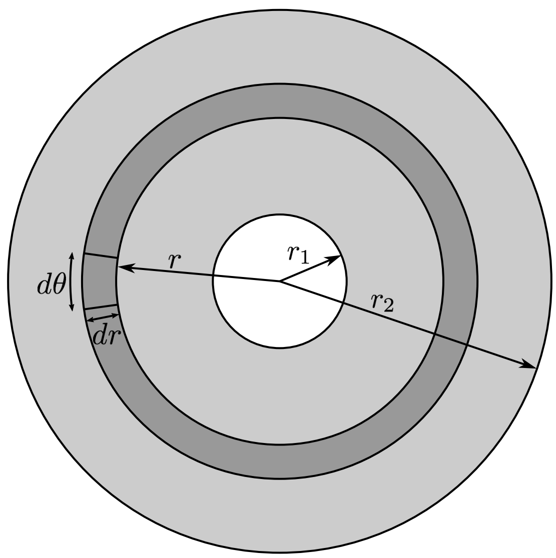

Figure 5.3: Diagram of a Corbino disk, showing an annulus and segment thereof for the purpose of calculating its conductance.

ing a small piece of the sample of length dr and width $rd\theta$, as shown in Figure 5.3. In steady state, Maxwell's equations state that the line integral $\oint \vec{E} \cdot d\vec{l'} = 0$, and therefore, by symmetry, $E_\theta = 0$ when considering the path to be the circle of radius r. However, note that there may still be a current flow j_θ. We might naively set out to calculate R from ρ_{xx} by calculating the electric field due to an applied current density,

$$\begin{pmatrix} E_r \\ 0 \end{pmatrix} = \begin{pmatrix} \rho_{xx} & \rho_{xy} \\ -\rho_{xy} & \rho_{yy} \end{pmatrix} \begin{pmatrix} j_r \\ j_\theta \end{pmatrix}, \tag{5.1}$$

but it is more straightforward to work with conductivity by writing down the conductance,

$$\begin{pmatrix} j_r \\ j_\theta \end{pmatrix} = \begin{pmatrix} \sigma_{xx} & \sigma_{xy} \\ -\sigma_{xy} & \sigma_{yy} \end{pmatrix} \begin{pmatrix} E_r \\ 0 \end{pmatrix}, \tag{5.2}$$

which simplifies to $j_r = \sigma_{xx} E_r$. The resistance of the annulus with radius r and width dr is then

$$dR = \left(\int_0^{2\pi} \sigma_{xx} r d\theta \right)^{-1} dr = \frac{dr}{2\pi r \sigma_{xx}}, \tag{5.3}$$

and the resistance between inner and outer contacts is

$$R = \int_{r_1}^{r_2} \frac{dr}{2\pi r \sigma_{xx}} = \frac{\log(r_2/r_1)}{2\pi \sigma_{xx}}. \tag{5.4}$$

Conventionally, we measure the conductance, since the resistance diverges as σ_{xx} vanishes at QH minima. The relation

$$2\pi \sigma_{xx} = G \log(r_2/r_1) \tag{5.5}$$

relates the microscopic transport property (σ_{xx}) to the macroscopically measurable quantity (G). Figure 5.4a shows an example measurement of R_{xx} and R_{xy} in a Hall bar. Using those two measurements and the known sample dimensions, σ_{xx} was calculated and is shown in Figure 5.4b. The behaviour of σ_{xx} is qualitatively similar to ρ_{xx}, apart from an overall scaling factor of $1/B^2$ which leads to a rapidly increasing conductivity as B approaches zero (see inset). The differing behaviour between ρ_{xx} and σ_{xx} in Figure 5.4 can help us develop an intuition about how to interpret these two quantities. In Figure 5.4a, we see that ρ_{xx} basically oscillates around its zero field value - at least, until the oscillation amplitude becomes too large and the minima reach zero. We may think of ρ_{xx} as the material's intrinsic resistivity, related to the carrier lifetime and DOS near the Fermi level. Conversely, the conductivity, σ_{xx}, decreases drastically with increasing magnetic field, since it factors in not only changes to the carrier lifetime and DOS due to magnetic effects, but also the lengthening of the current path due to the Corbino effect. We may think of σ_{xx} as the actual bulk conductance of the 2DEG (albeit normalized to remove geometric factors); *i.e.* a measure of its ability to move charge in response to an applied electric field, and the relevant property to use when calculating power dissipation in a Corbino disk. This intuition about ρ_{xx} and σ_{xx} can also be shown

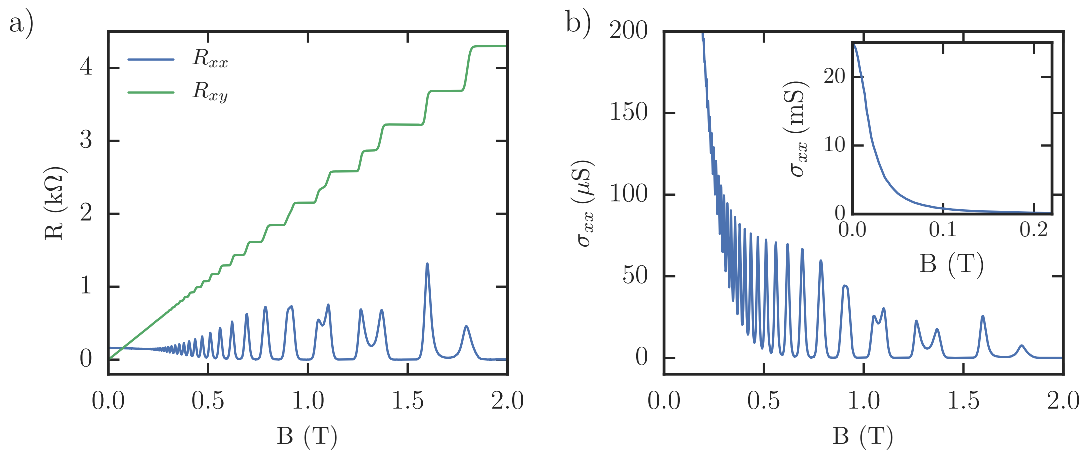

Figure 5.4: a) R_{xx} and R_{xy} measured in a Hall bar (device HB01, described in Appendix A). b) σ_{xx} calculated from R_{xx} and R_{xy}, reflecting what the conductance of a Corbino device fabricated from the same wafer would look like (up to a geometric scaling factor). The inset shows σ_{xx} from 0 to 0.22 T. Note the different scale on the inset - mS instead of μS.

more formally in the Drude model with a magnetic field, where it can be shown that $\rho_{xx} = \frac{m^*}{n_e e^2 \tau}$ and $\sigma_{xx} \approx \frac{\rho_{xx}}{\rho_{xy}^2}$. Because ρ_{xx} is a more direct measure of the microscopic carriers' physics, it is necessary to convert σ_{xx} to ρ_{xx} before attempting to extract transport lifetimes from the conductance data.

5.4 Fabrication of Corbino geometry devices

The Corbino geometry samples used in this thesis are GaAs/AlGaAs heterostructures grown by molecular beam epitaxy (MBE). Rather than attempting to cut or etch the samples into disc shapes, we simply deposited the two contacts using e-beam lithography, as shown in Figure 5.5. Both Corbino devices have an inner contact radius $r_1 = 0.25$ mm, outer contact inner radius $r_2 = 1.0$ mm and outer contact outer radius $r_3 = 1.5$ mm. Although several samples were fabricated, only two were used in the experiments reported in this thesis. The first, CB01, was grown at Sandia National Laboratories and has a mobility of around 10^6 cm^2/V $\cdot$ s. The second, CB05, was grown at Princeton University and has a much higher mobility of around 2.5×10^6 cm^2/V $\cdot$ s. Further details of the two samples are provided in Appendix A, and detailed characterization, including measurements of their electron density and mobility, are provided in the next sections.

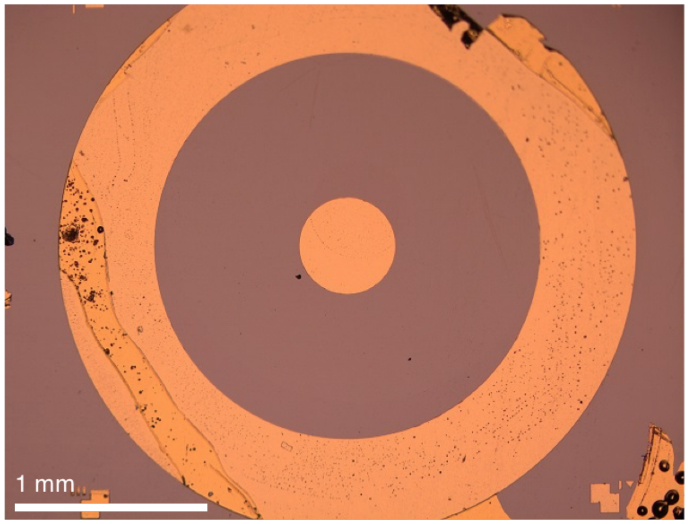

Figure 5.5: Photograph of a typical Corbino device similar to CB01 and CB05.

5.5 Characterization of sample CB01 (high-mobility device)

5.5.1 Density and mobility determination

The Corbino geometry presents special challenges when trying to determine the sample's mobility and electron density. In the Hall and VdP geometries, one can simply perform a linear fit to $R_{xy}(B)$ to determine the electron density and measure $R_{xx}(B = 0)$ to determine the mobility (as discussed in reference [8], for example). In the Corbino geometry, there is no simple way[1] to measure R_{xy} to determine the density. It is also a two-terminal device, and as such it is impossible to accurately separate the 2DEG's resistance from the contact resistance. To determine the electron density, n_e, we can look at $G(B)$ and identify the IQH features for which the filling factor is known. Assuming n_e is fixed, the minima are centred at field values,

$$B_\nu = \frac{n_e h}{\nu e}, \tag{5.6}$$

where ν takes on integer values. Knowing that the conductivity minima must be spaced in B according to equation 5.6, we can readily infer the filling factors from the ratios of the locations of the minima in B. Figure 5.6 shows an example of G vs B in CB01 with minima labelled by their filling factor. From this labelling, we find

[1]It is possible to drive an azimuthal current in the device using a time-varying magnetic field and measure the resulting voltage [56–58], yielding σ_{xy}.

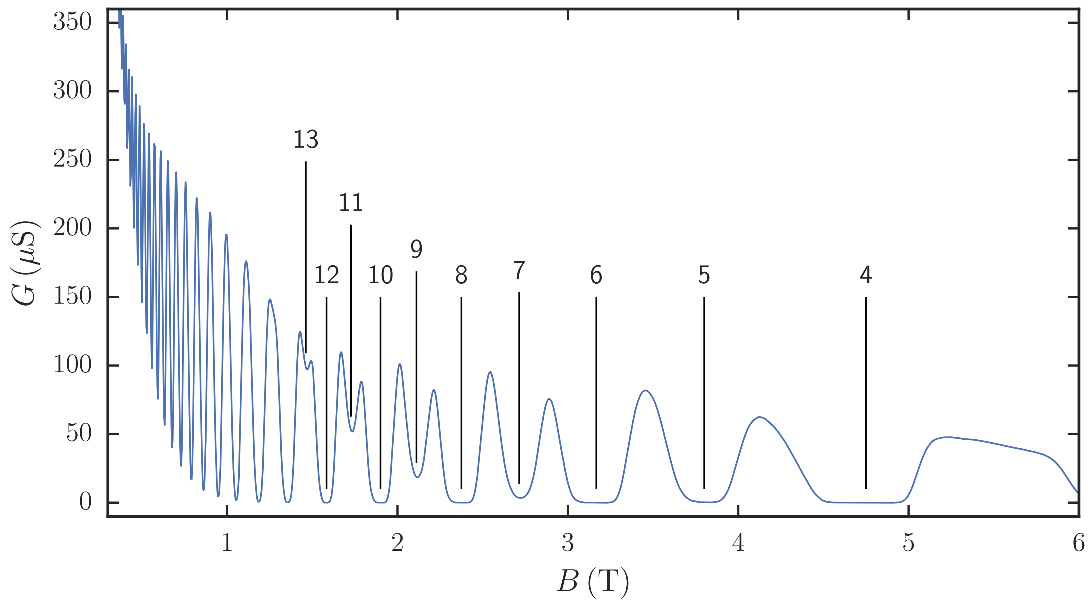

Figure 5.6: Conductance of CB01 at 450 mK, showing IQHE with labelled filling factors.

$n_e = 4.59 \times 10^{11}\,\mathrm{cm}^{-2}$ in this sample. At zero magnetic field, the resistance of the sample is much smaller than the combined contact and lead resistance, preventing an accurate measurement of the zero-field mobility. To partially overcome this problem, CB01 had four wires attached: two to each contact. This way, it was possible to avoid measuring the lead resistance, however the contact resistance was still inevitably included in the resistance measurement. Figure 5.7 shows the resistance of CB01 around B=0, using a 13.5 Hz, 10 nA, current-biased measurement (setup A). Using equations 2.8 and 5.5, we can write down R in terms of ρ_{xx} as

$$R = \frac{\log(r_2/r_1)}{2\pi}\left(\rho_{xx} + \frac{\rho_{xy}^2}{\rho_{xx}}\right) + R_{contact}. \tag{5.7}$$

By substituting $\rho_{xy} = B/n_e e$ and $\mu = (\rho_{xx} n_e e)^{-1}$ into the above equation, we obtain

$$R = \frac{\log(r_2/r_1)}{2\pi}\left(\rho_{xx} + \frac{B^2}{n_e e \rho_{xx}}\right) + R_{contact}. \tag{5.8}$$

If we fit $R(B)$ with a parabola, we can extract the value of ρ_{xx} around $B = 0$ from the prefactor of B^2 independently of $R_{contact}$. Such a fit is shown in Figure 5.7b, yielding $\rho_{xx} = 14.5 \pm 0.5\,\Omega$ and $\mu = 9.6 \pm 0.3\,\times 10^5\ \mathrm{cm}^2/\mathrm{V}\cdot\mathrm{s}$. The same fit also

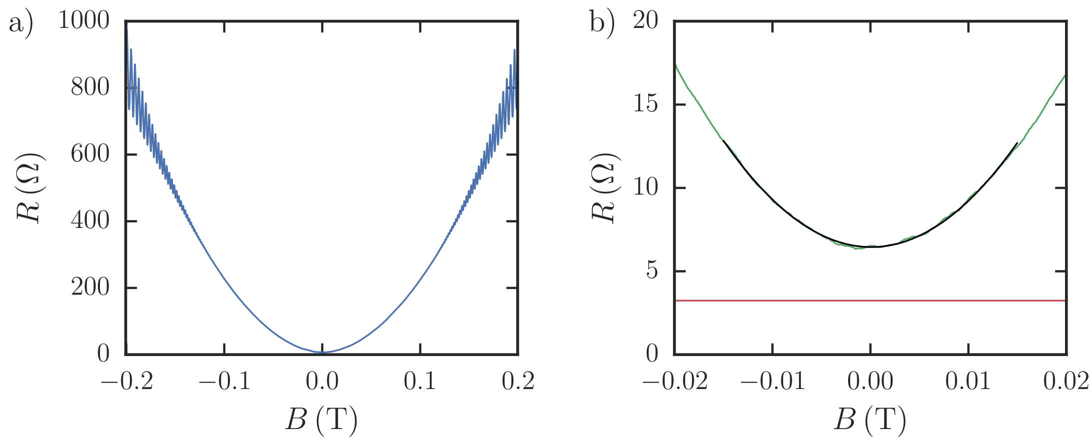

Figure 5.7: a) Resistance of CB01 near B = 0. b) R data (green line) and a least-squares fit (black line) of the equation $R = a \times (B - B_0)^2 + c$, where a and c are used to extract the mobility and contact resistance as described in the text, and B_0 allows for a possible offset of the true zero field. Using the results of the fit and the procedure outlined in the text, we find $\mu = 9.6 \pm 0.3\ \times 10^5$ cm^2/V $\cdot$ s and $R_{contact} = 3.24 \pm 0.05\,\Omega$ (indicated by the red line). Uncertainties were estimated by varying the fitting range between ± 0.1 T and ± 0.2 T, and reflect the slight systematic deviation of the data from purely parabolic behaviour.

yields $R_{contact} = 3.24 \pm 0.3\,\Omega$, as shown by the red horizontal line. Since the inner contact is smaller in area than the outer one by a factor of 20, we can infer that it is the main source of the measured contact resistance.

5.5.2 Conversion to ρ_{xx} and Dingle plot

Based on equation 2.8, ρ_{xx} can be calculated from σ_{xx} and ρ_{xy} as

$$\rho_{xx} = \frac{1 \pm \sqrt{1 - 4\sigma_{xx}\rho_{xy}}}{2\sigma_{xx}}, \tag{5.9}$$

where the positive sign is used for low field where $\rho_{xx} > \rho_{xy}$ and the negative sign is used for $\rho_{xx} < \rho_{xy}$. Figure 5.8 shows ρ_{xx} calcuated for CB01 from the same data shown in Figure 5.7. Note that the apparent "jump" in ρ_{xx} is an artefact due ot the sensitivity of equation 5.9 to the precise value of ρ_{xy} near the crossover point where ρ_{xy} becomes larger than ρ_{xx}. It is not immediately clear whether the general increase of ρ_{xx} with B is due to changing contact resistance, magnetoresistance of the Corbino itself, or an error in the calculation of the contact resistance. The latter could occur if ρ_{xx} is field dependent very close to $B = 0$, due to, for example, weak

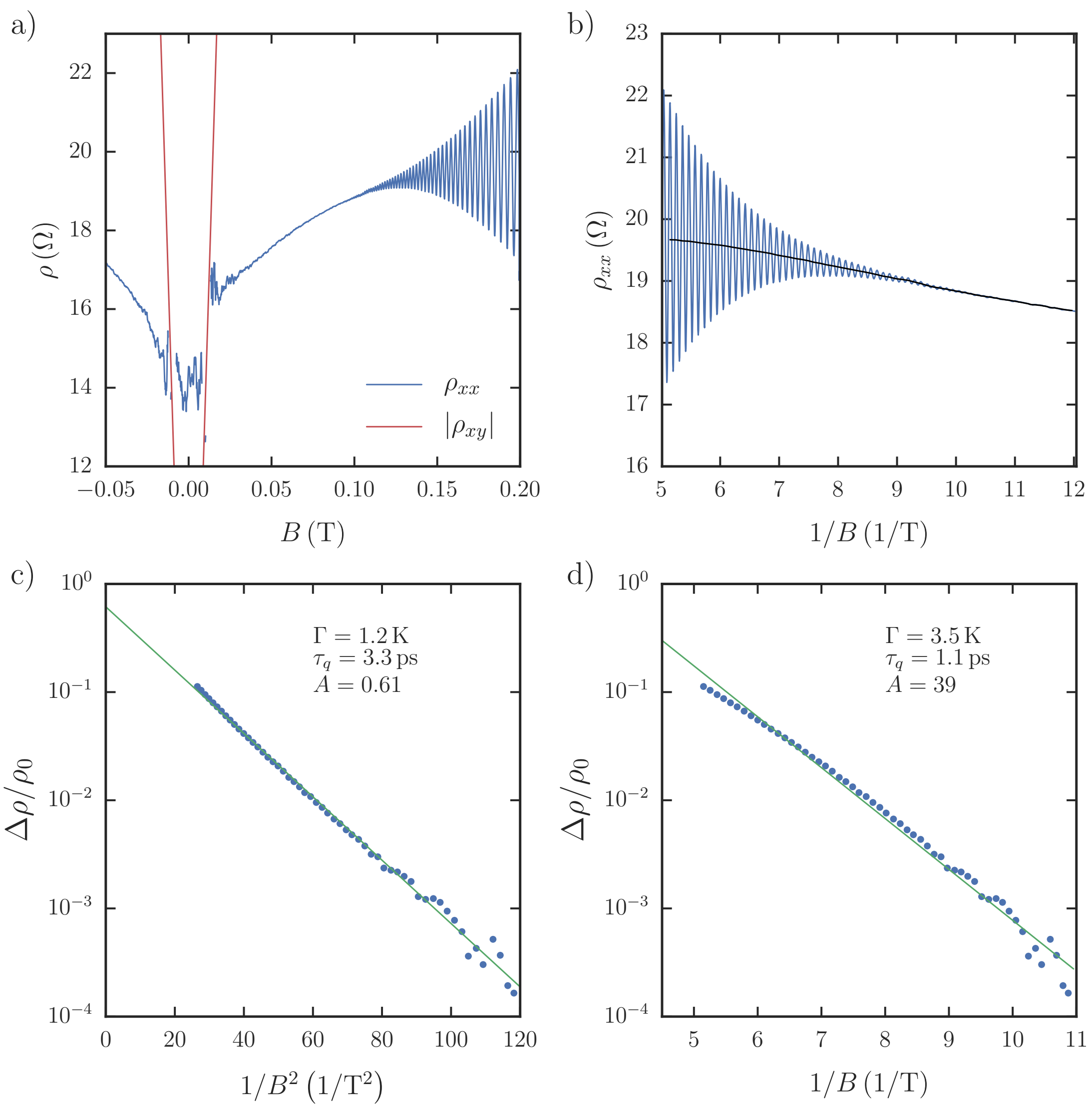

Figure 5.8: SdH oscillations plotted in ρ_{xx} and Dingle plots. a) ρ_{xx} (in blue) calculated from Corbino resistance using equation 5.9. $|\rho_{xy}| = |B|/ne$, is also shown in red. b) ρ_{xx} vs 1/B, showing evenly-spaced SdH oscillations and the moving average of ρ_{xx} (black line). c) Dingle plot using $1/B^2$ on the x-axis (appropriate for Gaussian broadening). d) Dingle plot using $1/B$ on the x-axis (appropriate for Lorentzian broadening).

localization [8].

SdH oscillations provide a way to estimate the Landau level broadening Γ, or equivalently the quantum lifetime τ_q, of electrons in the 2DEG. As shown in Figure 5.8b, the SdH oscillations in this sample appear in the vicinity of B=0.095 T. Since the onset of the oscillations requires separation of LLs on the order of their broadening, we can immediately estimate $\Gamma = 12$ K from the value of $\hbar\omega_c$ at the onset field. The broadening can also be expressed as the quantum lifetime, $\tau_q = \hbar/2\Gamma$, which is $\sim$ 0.3 ps based on the extinction point estimate. A more formal way to find Γ is to plot ρ_{xx} vs 1/B, as shown in Figure 5.8b and construct a Dingle plot of the amplitude of the SdH oscillations. It has been shown [59] that if the LLs are broadened by a Lorentzian function, then the amplitude of the oscillations is given by

$$\frac{\Delta\rho_{xx}}{\rho_{xx}} = A\exp\left(\frac{-\pi}{\omega_c\tau_q}\right), \tag{5.10}$$

where A is a constant that depends on the relationship between conductance and the underlying DOS. If the broadening is Gaussian instead, the SdH amplitude is given by

$$\frac{\Delta\rho_{xx}}{\rho_{xx}} = A\exp\left(\frac{-2\pi^2\Gamma^2}{\hbar^2\omega_c^2}\right), \tag{5.11}$$

where the Gaussian broadened LLs take the form $\exp(-(\epsilon-\epsilon_n)^2/2\Gamma^2)$ [59]. Based on equations 5.10 and 5.11, the form of the broadening function can be distinguished by fitting $\log(\Delta\rho/\rho)$ to $1/B^2$ and $1/B$ and seeing which one is closest to linear. Such fits are plotted in Figure 5.8c and d [2]. The fit vs $1/B^2$ is more linear, with only a slight deviation of the data points from the linear trend at low values of $1/B^2$. This is often observed [6] as $\Delta\rho$ approaches ρ and the SdH oscillations begin to deform. The plot versus $1/B$ is clearly curved with a negative second derivative everywhere. These two results are overall similar to the results of Piot *et. al.*, and lend support to a model of Gaussian-broadened disorder. Based on the fit to $1/B^2$, the broadening is $\Gamma = 1.2$ K or $\tau_q = 3.3$ ps. However, it should be noted that the temperature for these measurements, 450 mK, is not much lower than Γ, and there could be finite temperature effects built into the estimate of Γ. The intercept of the Dingle plot fits is expected to be $A = 2$ if ρ_{xx} is proportional to the DOS, and $A = 4$ if ρ_{xx} is proportional to the square of the DOS. For the fit to $1/B^2$, we find $A = 0.61$, which

[2]Note that the resistance of the sample throughout the plotted range exceeds 200 Ω, making the fit insensitive to any error in the measured contact resistance of less than 5 Ω.

is much closer to the theoretically expected values than $A = 39$ for the $1/B$ fit, further validating that Gaussian-broadened disorder is a better description of the data. However, the fact that A is off by a factor of four from the closest theoretically predicted value is surprising, and suggests that the nature of the disorder in this sample is not fully captured by the simple Gaussian broadening model in [59].

5.6 Magnetotransport in an ultra-high mobility Corbino device

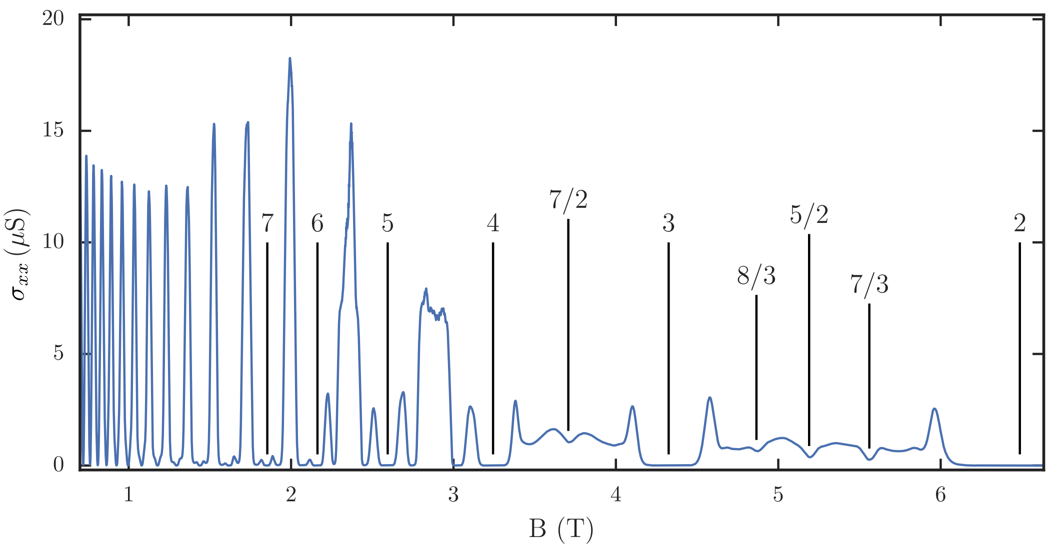

Figure 5.9: Magnetoconductance of sample CB05, with labelled integer and fractional quantum Hall minima.

In this section, we will characterize a second sample, CB05, which is fabricated on a much higher mobility wafer. As shown in Figure 5.9, this sample shows a rich array of features in its magnetoconductivity. In addition to the labeled IQH minima, there are peaks and dips corresponding to various many-body phases: bubble phases, stripe phases and FQH states. We will discuss this device's behaviour in three magnetic field regimes. First, we will use the techniques introduced in the previous section to estimate the sample's mobility and quantum lifetime from its conductivity and SdH oscillations in the low field regime ($B < 1\,\mathrm{T}$). Next, at intermediate fields ($1\,\mathrm{T} < B < 3.2\,\mathrm{T}$), we will look at the electronic stripe and bubble which occur for

$\nu > 4$ in ultra-high mobility samples. Finally, we will discuss the FQH states which occur for $\nu < 4$ ($B > 3.2$ T).

5.6.1 Low field characterization of CB05

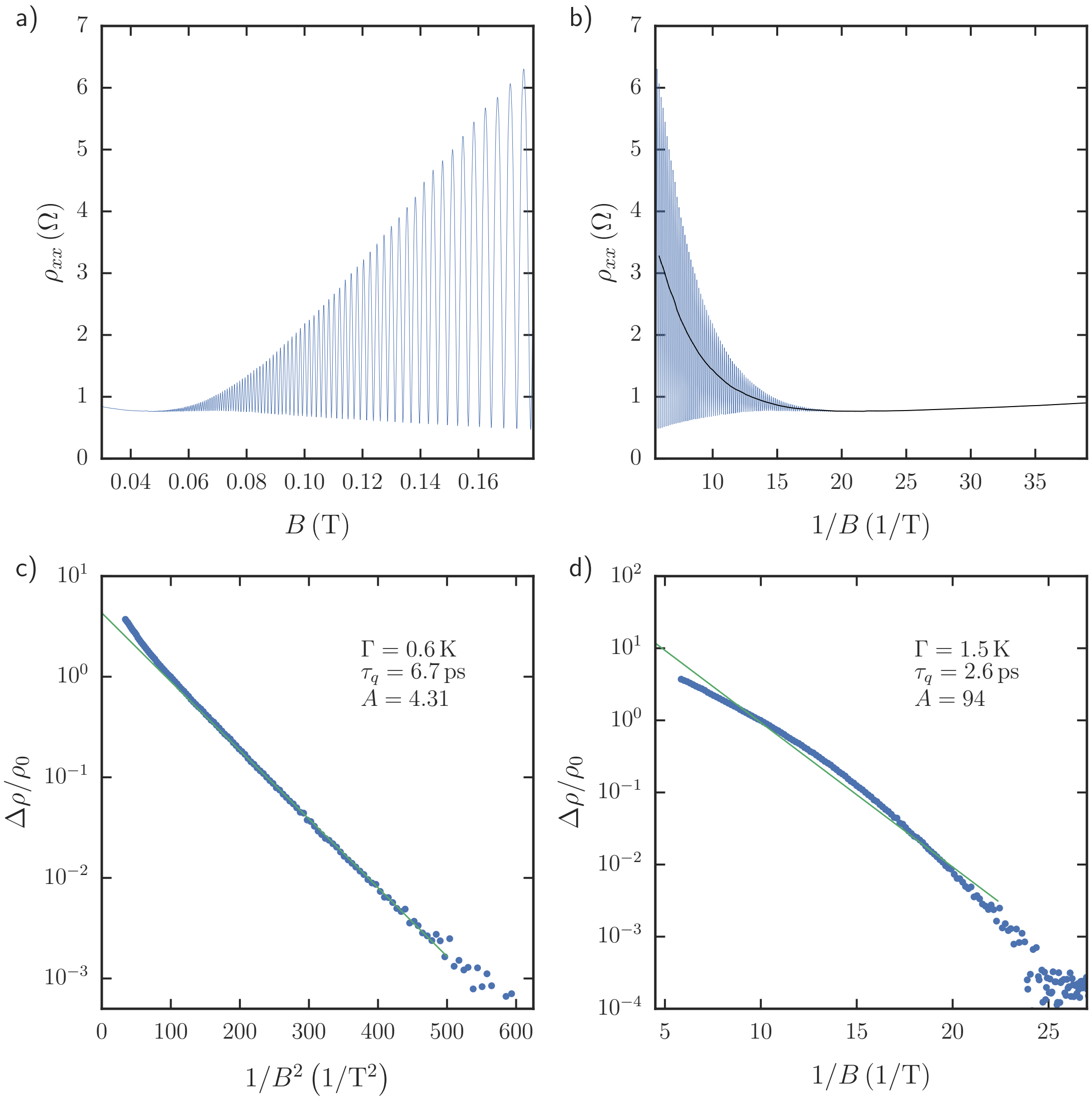

Figure 5.10: SdH oscillations plotted in ρ_{xx} and Dingle plots. a) ρ_{xx} (in blue) calculated from Corbino resistance using equation 5.9. b) ρ_{xx} vs 1/B, showing evenly-spaced SdH oscillations and the moving average of ρ_{xx} (black line). c) Dingle plot using $1/B^2$ on the x-axis (appropriate for Gaussian broadening). d) Dingle plot using $1/B$ on the x-axis (appropriate for Lorentzian broadening).

Figure 5.10a shows the low-field resistivity of the sample calculated from σ_{xx}, with σ_{xy} assumed to be simply the classical Hall conductivity for n_e inferred from the QH minima labelled in Figure 5.9. According to measurements performed by the sample grower at 0.3 K, the wafer had a mobility of $25 \times 10^{11}\,\mathrm{cm}^2/\mathrm{V}\cdot\mathrm{s}$ and a density of $3 \times 10^{11}\,\mathrm{cm}^{-2}$. The expected zero field value of ρ_{xx} is then $0.83\,\Omega$, which is close to the value at the lowest field measured in Figure 5.10a. The extremely high quality of this sample is also apparent from the appearance of SdH oscillations at a very small magnetic field, 0.040 T, which suggests $\tau_q = 4.8$ ps and $\Gamma = 0.8$ K. The results of Dingle plot analysis using $1/B^2$ roughly agree with the simple extinction point estimate, yielding $\tau_q = 6.7$ ps and $\Gamma = 0.6$ K. As in CB01, plotting versus $1/B$ gives an obviously less linear fit.

The extracted value of τ_q is much smaller than the transport lifetime calculated from the sample mobility, $\tau_t = 950$ ps, as expected for samples in which long-range scattering from remote impurities is the primary scattering mechanism [8, 60, 61]. The quantum lifetime is also smaller by about a factor of five than the value, $\tau = 33 \pm 3$ ps, found for another sample previously measured in our lab [8]. We tentatively attribute the lower quantum lifetime to the density, structure of the wells and location of the dopants (*i.e.* setback distance). Sample CB05 has roughly twice the density ($3.06 \times 10^{11}\mathrm{cm}^{-2}$ vs. $1.6 \times 10^{11}\mathrm{cm}^{-2}$) and half the setback distance (80 nm vs. 160 nm) of the sample in reference [8]. This may lead to an increase in the scattering rate, and consequently to an increased Landau level width.

5.6.2 Bubble and stripe phases in high Landau levels

At filling factors between $\nu = 4$ and $\nu = 14$, we observe rich behaviour of the conductivity between the IQH minima, as shown in Figure 5.11. These additional peaks and dips are due to bubble and stripe phases, rather than FQH states, and have been studied primarily around $\nu = 4, 5$ and 6 [62–64]. Their presence at even higher filling factors indicates the extremely high quality of the sample.

The stripe phases, occurring at half-filling of each LL, are known to be anisotropic [62, 63]. Since our Corbino-geometry sample is radially symmetric, we are unable to check for this anisotropy, instead measuring the integral of the conductance in all directions. The current between the contacts preferentially flows in the easy direction - hence, we observe a peak, even if conductivity in the hard direction is greatly suppressed. We observe "textbook" examples of such peaks at $\nu = 6 + 1/2$, $\nu = 7 + 1/2$ and $\nu = 8 + 1/2$. At still higher filling factors, the peak can just be discerned up to $\nu = 10 + 1/2$. Going the other direction in magnetic field, at

$\nu = 4$ (and to some degree at $\nu = 5$), the peak in conductivity is suppressed. One possible explanation for this is that the anisotropy in conductance forces the current to flow only along a narrow strip (with width equal to the inner contact diameter), increasing the current density and therefore the local temperature of the 2DEG via Joule heating. The measurements in Figure 5.11 were performed using a current preamplifier with a DC bias of up to 5 nA, which may have been sufficient to cause self-heating.

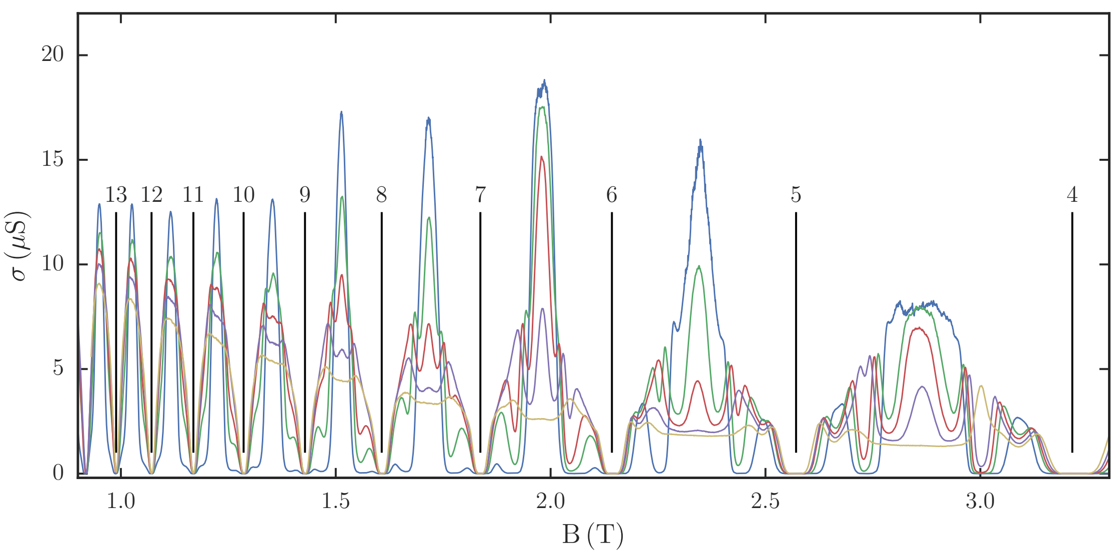

Figure 5.11: Temperature evolution of IQHE and RIQHE in high filling factors. Conductivity vs. field at base temperature of 22 mK (blue), 80 mK (green), 100 mK (red), 120 mK (purple) and 153 mK (gold).

The primary series of bubble phases are visible as well-developed minima on the flanks of the IQH minima up to $\nu = 9$. At still higher filling factors, they appear to slightly deform the flanks of each IQH minimum up to $\nu = 13$. The persistence of both these bubble phases and the stripe phases to such high filling factors is also a strong indication of the extremely high quality of the sample.

5.6.3 Activation measurements of fractional quantum Hall states

At filling factors above $\nu = 4$, we observe minima in the conductivity due to the FQHE. These include $\nu = 5/2$ and $\nu = 7/3$ in the SLL, as shown in Figure 5.12. To determine the energy gap, Δ, of each state, we performed standard Arrhenius

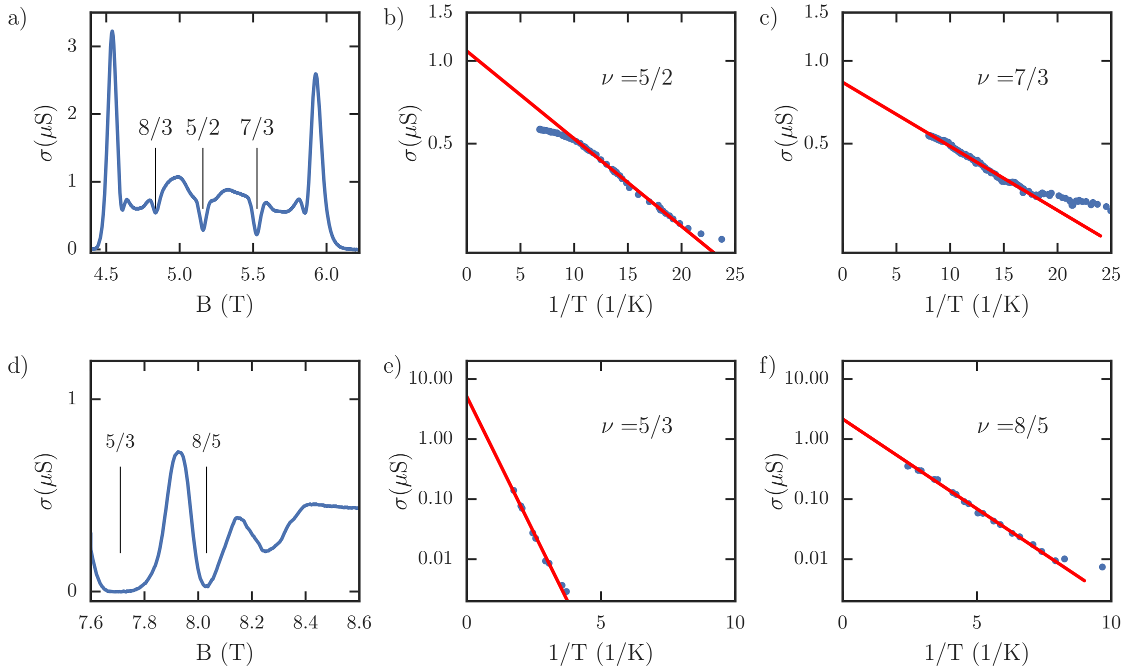

Figure 5.12: Magnetoconductance and Arrhenius plots in the LLL and SLL. a) σ_{xx} vs B in the SLL at base temperature, $T_{mc} = 23$ mK. b,c) Arrhenius plot of conductivity minimum versus the inverse temperature at $\nu = 5/2$ and $\nu = 7/3$. d) σ_{xx} vs B in the LLL at base temperature, $T_{mc} = 23$ mK. e,f) Arrhenius plots at $\nu = 5/3$ and $\nu = 8/5$. The red lines are a linear fit to subsets of the data and correspond to the gap energies. These, and the intercept values are reported in Table 1.

fits as shown in Figure 5.12b and c, using the relation $\sigma_{xx} = \sigma_0 e^{-\Delta/2k_BT}$. The gaps for $\nu = 5/2$ and $\nu = 7/3$ were determined to be 147 ± 7 mK and 107 ± 5 mK respectively. Larger energy gaps are expected based on numerical calculations (see [48] and references therein) and experimentally measured activation gaps as high as 450 mK have been reported previously in the literature [65]. The relatively modest gap we observe may be due to some combination of the precise quantum well shape and disorder of the sample. The disorder, in particular can be tuned by LED illumination of the sample during the cooldown procedure, which is known to have effects on $\nu = 5/2$ beyond simply changing the sample density and mobility [66].

Conductivity extrapolation

Prior to successful measurements of shot noise in the FQH regime, there was great interest in any experimental approach to the problem of confirming the predicted fractional charge of FQH quasiparticles. One approach was to look at the

Table 5.1: Arrhenius fit parameters for data shown in Fig. 5.12.

ν	Δ [mK]	q	σ_0 [μS]	$h\sigma_0/q^2$
5/2	147 ± 7	e/4	1.09 ± 0.07	0.45 ± 0.03
7/3	107 ± 5	e/3	0.84 ± 0.05	0.19 ± 0.01
5/3	4180 ± 210	e/3	5.1 ± 0.2	1.19 ± 0.35
8/5	1380 ± 70	e/5	2.2 ± 0.4	1.39 ± 0.25

prefactor σ_0 from the Arrhenius fit, which was predicted to be

$$\sigma_0 = \frac{2q^2}{h}, \tag{5.12}$$

at least for disorder in the form of long-range random potential as discussed in references [67, 68]. Since, in the Corbino geometry, we measure σ_{xx} directly, it is trivial to extract σ_0 from the y-intercept of the Arrhenius plots in Figure 5.12, yielding the values for σ_0 presented in Table 5.1. The values of q in the table are the theoretically predicted quasiparticle charge at each filling factor (with $e/4$ used at $\nu = 5/2$ based on the assumption of a Pfaffian wavefunction and supported by shot noise measurements [21]). The uncertainties in Δ and σ_0 are estimated statistical errors based on the fits.

At $\nu = 5/3$ and $\nu = 8/5$, which are LLL states with relatively large gaps ($\Delta > 1$ K), we find $q^2/h < \sigma_0 < 2q^2/h$. This is in line with a calculation by d'Ambrumenil *et al.* showing that for realistic models of disorder, tunneling effects reduce the value of σ_0 below the value given by equation 5.12 [68]. In the SLL, we observe much larger deviation from the theoretical prediction, suggesting that further work is required to understand transport in this regime. In the future, it would be interesting to repeat the experiment in a sample where the SLL states have even larger energy gaps, in order to resolve whether the discrepancy is related to the details of the disorder or is intrinsic to SLL transport.

5.7 Summary

The Corbino geometry is particularly interesting for FQHE studies because it provides a way to probe the bulk of the sample in transport measurements, unlike Hall measurements which are most often dominated by edge physics. We have fabricated and characterized an ultra-high mobility Corbino sample, CB05, which shows many signatures of strongly-interacting electron physics, including a FQHE minimum at $\nu = 5/2$. Finally, we revisited the subject of σ_0 in Arrhenius plots. Our results in the first Landau level are consistent with past experimental and theoretical results, however in the second Landau level σ_0 does not follow the expected (naive) relationship between σ_0 and q. It is not immediately obvious why this is the case, although it suggests at the very least that transport in the SLL is not fully captured by existing models.

Chapter 6

Thermalization of a 2DEG in the FQH regime

The difficulty of cooling electrons is a well-known challenge in semiconductor physics, with the electronic temperature in GaAs/AlGaAs heterostructures often observed to saturate well above the base temperature of the refrigerator. Colloquially, this is understood to be due to the phonons "freezing out" at low temperature, leaving electron diffusion as the only cooling mechanism. While it is true that the electron-phonon coupling is weak at low temperature, we will show that, in the case of a millimetre-scale Corbino device, the electron-phonon interaction is still the dominant cooling mechanism even below 100 mK. Based on our experimental data and modelling, the extrapolated crossover to electron diffusion cooling occurs only in the few-mK temperature regime.

The fact that cooling electrons is difficult also presents an opportunity: it means that there is a built-in "weak link" between the 2DEG and the phonon bath. Thus, it is possible to design an experiment to measure specific heat where the "system" is the 2DEG itself and the "environment" is the phonon bath - a major improvement over previous experiments [69–71] where the "system" included the entire GaAs/AlGaAs heterostructure, plus contacts, thermometer, heater etc. This chapter includes both a general overview of 2DEG thermalization and specific calculations relevant to the experimental work presented in the next chapter.

6.1 Thermal Circuit Model

A system thermalizing to its thermal environment can be modelled as a thermal circuit, in which temperature gradients and heat flows may be thought of as thermal equivalents of voltage and current. In the simple model shown in Figure 6.1a, a tem-

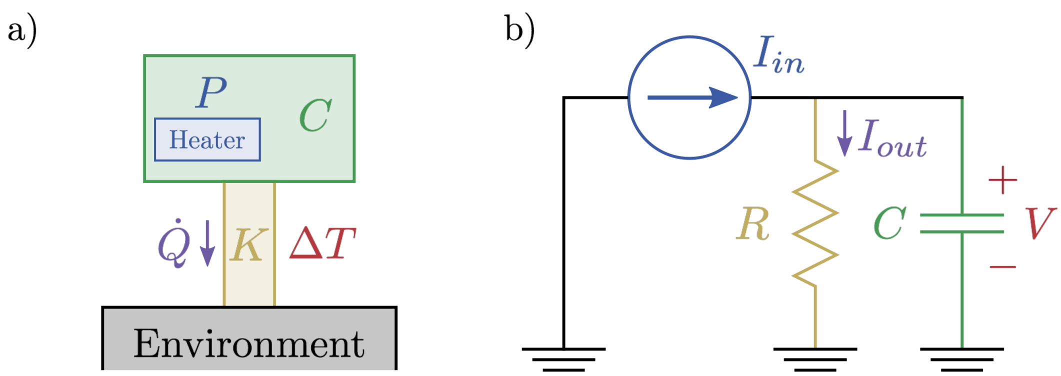

Figure 6.1: Thermal circuit model and its electrical analogue. (a) Thermal circuit consisting of a body (green) with heat capacity C, a thermal link (yellow) with thermal conductivity K to the environment (grey) and a heater (blue) dissipating power P within the body. A thermal current $\dot{Q}$ and temperature difference ΔT result. (b) The electrical analogue of the thermal circuit, with components and values coloured to match their thermal equivalents. A capacitor with capacitance C is grounded by a resistor with resistance R (equivalent to $1/K$ in the thermal circuit) and charged by a current source I_{in}. As a result, a current I_{out} flows across the resistor and a voltage V develops across the capacitor.

perature difference, ΔT, drives a heat current $\dot{Q}$, from the body to the environment via a thermal conductor. For a small temperature difference, the relationship between ΔT and $\dot{Q}$ is linear, and we can define a thermal conductance[1], $K = \dot{Q}/\Delta T$, analogous to electrical conductance G. The relationship between Q, and T for the body is given by the heat capacity, $C \equiv \frac{\partial Q}{\partial T}$. In the equivalent electrical circuit, shown in Figure 6.1b, heat takes the place of charge and temperature takes the place of voltage. Therefore, heat capacity is the equivalent of electrical capacitance. Continuing the analogy, we can also recognize that the thermal circuit shown in Figure 6.1a has a characteristic RC time constant given by $\tau = C/K$. If a heat source within the body is turned on or off in a step, the temperature response will be

$$\Delta T(t) = \Delta T_{initial} e^{-t/\tau} + \Delta T_{final} \left(1 - e^{-t/\tau}\right). \tag{6.1}$$

The rest of both this chapter and the next one will discuss our measurements of K, τ, and thus C. We begin by reviewing previous theoretical and experimental work

[1] Throughout this thesis, the upper case letter kappa (K) is used to denote thermal conductance. Thermal conductivity is denoted by lower case kappa (κ).

regarding the thermal link between a 2DEG and its environment.

6.2 Theory and literature review

The bulk of the 2DEG can potentially thermalize with the environment via two primary mechanisms: electron-phonon coupling (*i.e.* emission of phonons into the 3D bulk GaAs) and thermal diffusion within the 2DEG to the contacts. We can characterize each of these by an effective thermal conductivity, denoted κ_{e-ph} and κ_{WF} respectively. Note that κ_{e-ph} is in units of $\mathrm{W/K \cdot m^2}$, since it is proportional to the area of the 2DEG, whereas κ_{WF} is in W/K with an implied "per-square" geometric dependence analogous to the 2D electrical conductivity σ_{xx}.

6.2.1 Electron diffusion: Wiedemann-Franz law

In the case where both heat and charge are carried by the same quasiparticles (or electrons), the electrical and thermal conductivities are directly related to one another according to the WF law,

$$\kappa_{WF} = \sigma_{xx} L_0 T, \tag{6.2}$$

where $L_0 \approx \frac{\pi^2}{3}\left(\frac{k_B}{e^*}\right)^2$ is the Lorenz constant [72, 73] for quasiparticles of charge e^*. Equation 6.2 has no dependence on dimensionality, since the dependence of the thermal and electrical diffusion constants on dimensionality are the same.

Violations of the Wiedemann-Franz law

Besides cases where phonons provide another heat conduction channel, a number of other cases have been suggested where the WF law does not hold. In metals, the value of L_0 is empirically found to be slightly different from the theoretical prediction. The WF law assumes that the relaxation time for thermal and electrical conductance are identical, which is true for large-angle elastic scattering, but not small-angle inelastic scattering [74]. The latter would lead to a loss of heat as the quasiparticle diffuses, resulting in a reduced thermal conductivity.

Other violations of the WF law occur in correlated transport. Most obviously, cooper-paired electrons in a superconductor transport charge but not heat. Conversely, neutral excitons formed by bound electron-hole pairs can transport heat but not charge. Such neutral fermions are expected to exist at $\nu = 5/2$ and may contribute to thermal transport [75].

Karavolas and Triberis [76] have calculated the ratio κ/σ for the quantum Hall regime, and shown that the WF law is violated near half-filling in broadened Landau levels when $T > \Gamma$. This is because the WF law is only strictly valid when the DOS is approximately linear within $k_B T$ of the Fermi level, which is not true when $k_B T$ is comparable to the LL width, Γ.

6.2.2 Electron-Phonon interaction

The electron-phonon interaction in GaAs heterostructures has been extensively studied both theoretically and experimentally, with a particular focus on the temperature range between 1 and 10 K. At those temperatures, phonon scattering limits the mobility of the 2DEG and the speed of GaAs based sensors such as hot-electron bolometers [77, 78]. This section will first provide a general overview of phonon scattering in GaAs heterostructures, and then focus on what is known about the low temperature regime (below 1 K) where our experiments were performed.

Phonon modes and interaction types

Phonons are vibrations (or sound waves) in the crystal lattice, which can be emitted when an electron in the 2DEG loses energy or absorbed to add energy to an electron. It is well-known that the phonon dispersion relation exhibits two types of modes: acoustic phonons have nearly linear dispersion at low energy, whereas so-called optical phonons have much higher energy even for small wavevectors. At low temperature, only acoustic phonon modes can participate in scattering, since optical phonons have energy much larger than $k_B T$. Acoustic phonons may be further categorized according to the type of vibration: transverse or longitudinal. Transverse phonons can scatter with electrons via the deformation potential interaction and the piezoelectric (PZ) interaction, while longitudinal modes interact via PZ effects only.

Bloch-Grüneisen regime

For either interaction type, we can further break down the temperature regime by considering momentum conservation in scattering and the strong phase-space restrictions that happen at low temperature [79]. In the case of an electron gas at temperature $T_e > T_{ph}$, an electron can lose its excess thermal energy by emitting a single phonon of typical energy $k_B T_e$ and corresponding wavevector $q_{typ} = k_B T_e/\hbar s$, where s is the speed of sound in the crystal. This is only possible if momentum conservation can be fulfilled, that is, if $q_{typ} < 2k_f$ as shown in Figure 6.2. At higher temperatures, where $q_{typ} > 2k_f$, an electron has to emit multiple phonons to lower its energy by $k_b T_e$. These low- and high-temperature regimes are known as the Bloch-Grüneisen and equipartition regimes, respectively, and the crossover temperature between them is given by $k_B T_c = 2k_f \hbar s$. For GaAs, the speed of sound is 3300 m/s [40], and for our usual electron density of $3 \times 10^{11}\,\text{cm}^{-2}$, $k_f = 1.4 \times 10^{-6} cm^{-1}$. Therefore, $T_c = 5.5$ K, which is much higher than our experimental temperature range ($T < 150$ mK), and all of our measurements are therefore in the Bloch-Grüneisen regime.

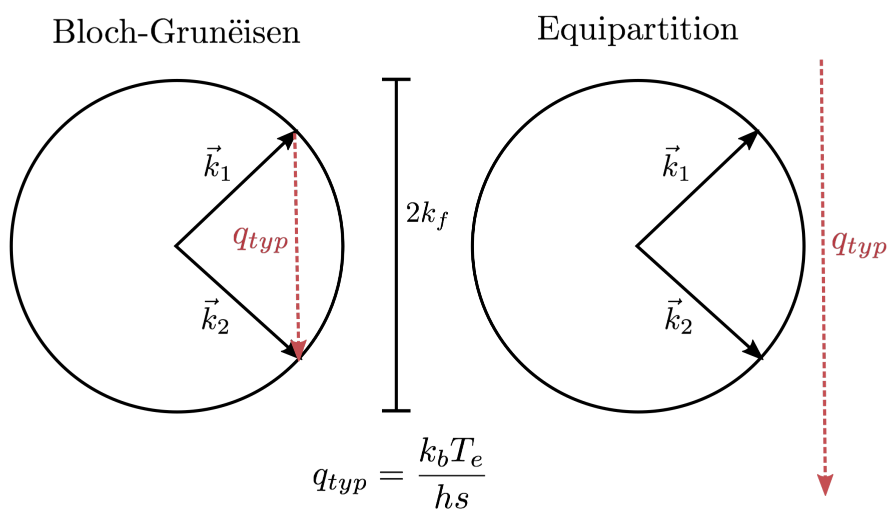

Figure 6.2: Fermi circles and wavevectors in the Bloch-Grunëisen and equipartition regimes. At low temperature (B-G regime, shown on the left), an electron can scatter from k_1 to k_2 by emitting or absorbing a single phonon with wavevector q_{typ}. At higher temperatures (equipartition regime, shown on the right), q_{typ} for T_e is too large to scatter between any pair of k_1 and k_2 on the Fermi surface. Multiple phonons must be emitted for the electron to change its energy by $k_B T_e$. Figure redrawn based on [80].

Role of dimensionality

Due to the close lattice matching between GaAs and AlGaAs, the phonons are not confined to the 2DEG plane (unlike in metallic thin films, where the acoustic impedance mismatch between the metal and substrate confines the phonons). Therefore, we must consider the interaction between 2D-confined electrons and 3D phonons. During a scattering event, momentum and energy must be conserved. In the x-y plane, this means that an electron scattering from k to k' scatters with a phonon with wavevector $q = k' - k$. On the other hand, the quantum well fixes the position of the electron in z, which means its momentum is unknown according to Heisenberg's uncertainty principle. Therefore, q_z can take values within a range of approximately $1/b$, where b is the width of the z direction wavefunction. More formally, we can define a form factor, $I(q_z)$, which can then be used to weight the scattering probability for emission (or absorption) of a phonon with a wavevector component q_z. We define $I(q_z)$ as follows:

$$I(q_z) = \int \psi_z^2 e^{iq_z z} dz, \tag{6.3}$$

where ψ_z is the z-direction wavefunction normalized such that $\int \psi_z^2 dz = 1$.

Power emission model

A model for the low temperatures electron-phonon power emission rate in GaAs heterostructures was first developed by Price [81]. Additional derivations of the same result can be found in works by Karpus [82] and Mittal [80]. Taking into account the appropriate scattering mechanism (PZ interaction with acoustic phonons in the BG regime), the form factor $I(q_z)$, and the appropriate corrections for screening and phonon dispersion anisotropy [83, 84], yields the expression

$$P_{emitted} = 1.37 n_e^{-\frac{1}{2}} T^5 \left[\frac{\mathrm{W}}{\mathrm{cm}^2}\right] \tag{6.4}$$

for the power emitted by the 2DEG, where n_e here is in units of cm^{-2}.

6.2.3 Experimental results in the literature

Low field power emission measurements

The model described in the previous sections has been tested experimentally by multiple groups. Appleyard et. al. [84] have measured the temperature of the 2DEG as a function of DC heating power at zero magnetic field, by using diffusion thermopower in a 1D constriction as a thermometer. Their results, shown in Figure 6.3, are in excellent agreement with the model in equation 6.4, with a crossover to electron diffusion as the primary cooling mechanism below 500 mK.

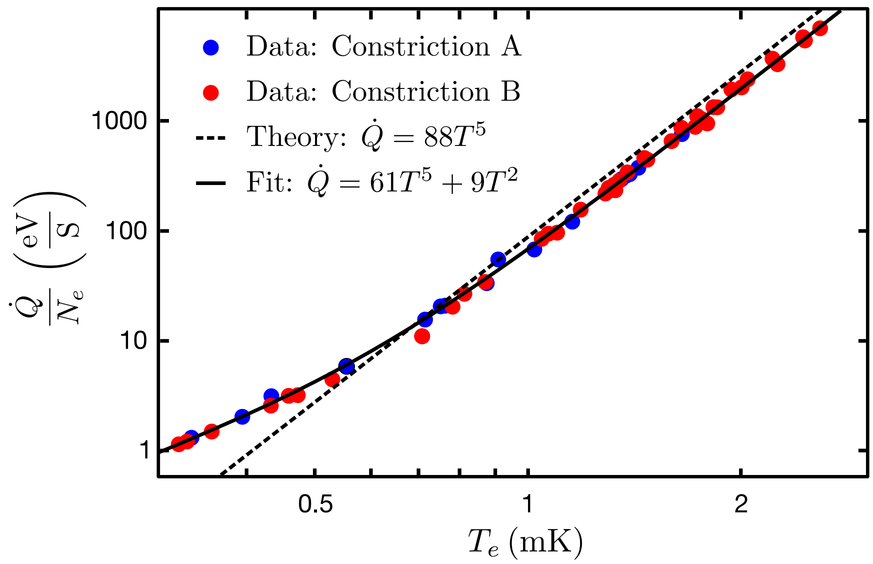

Figure 6.3: Power emission from a 2DEG measured at zero magnetic field using thermopower in two different 1D constrictions (A and B) as a thermometer. Equation 6.4 is shown by the dashed line, while the solid line is a fit to the data including terms for both phonon emission and electron diffusion. The sample parameters are $n_e = 2.1 \times 10^{11}\,\mathrm{cm}^{-2}$ and $\mu = 4.5^6\,\mathrm{cm}^2\mathrm{V}^{-1}\mathrm{s}^{-1}$. Data and fits from reference [84].

Most other attempts to measure power emission rates in GaAs have made use of the temperature sensitivity of SdH oscillations as the thermometer, and thus were necessarily performed in a magnetic field. Gammel *et. al.* [85], Mittal *et. al.* [86] and Chow *et. al.* [87] all found $P \propto T^5$, but with larger prefactors. However, Zhang *et. al.* [88] have raised serious concerns about the use of SdH oscillations as a thermometer while applying a DC voltage. They argue that spectral diffusion modifies the electron distribution into a non-equilibrium distribution, rather than a Fermi distribution at higher temperature. Moreover, they show that even small changes to the shape of the distribution function can strongly affect the observed conductivity, leading to significant errors in the inferred temperature using this technique.

Phonon contribution to mobility

The mobility, μ, of a sample is essentially the conductivity per carrier, given by $\mu = \sigma/nq$, where n is the carrier density and q is the carrier charge. Each scattering mechanism contributes to the mobility, and much like conductivities they can be summed according to Matthiessen's rule:

$$\frac{1}{\mu} = \frac{1}{\mu_{imp}} + \frac{1}{\mu_{e-ph}} + \ldots \tag{6.5}$$

Störmer *et. al.* [79] have used this rule to extract μ_{e-ph} from the temperature dependence of μ from 0.3 to 40 K. Their data fits well to a model of acoustic phonon scattering based on the same assumptions as equation 6.4. In a followup study, Kang *et. al.* [89] measured μ at both zero field and $\nu = 1/2$. They found a drastically enhanced scattering rate for CF's compared to electrons at $B = 0$, and also a weaker temperature dependence. Their results are summarized by the solid lines (and hatched areas indicating estimated uncertainties) in Figure 6.4.

Phonon contribution to thermopower

If a thermal gradient is applied to a GaAs wafer, a "phonon wind" will be established from the hot side to the cold side. This is simply because phonons with larger momentum can be emitted from the higher temperature side than from the cold side. When these phonons are absorbed by electrons in the 2DEG, the average momentum in the 2DEG is from hot to cold. Eventually, electrons build up at the cold electrode, creating an electric field that counteracts the force of the phonon wind. Since this phenomenon has at its core the electron-phonon coupling, it is possible to extract the scattering rates from phonon drag thermopower measurements. Indeed, Tieke *et. al.* [90] have published results for μ_{e-ph} at B=0 and μ_{cf-ph} at $\nu = 1/2$ and compared them to direct mobility measurements by Kang *et al.* [89]. Their zero-field results agree at the order of magnitude level with Kang *et al.* At $\nu = 1/2$, both groups see significant decrease in μ, suggesting stronger coupling between CFs and phonons than between electrons and phonons. However, their results differ by more than one order of magnitude. One possible explanation for the discrepancy is the significant differences in mobility between the samples, perhaps placing them in different regimes of disorder [91].

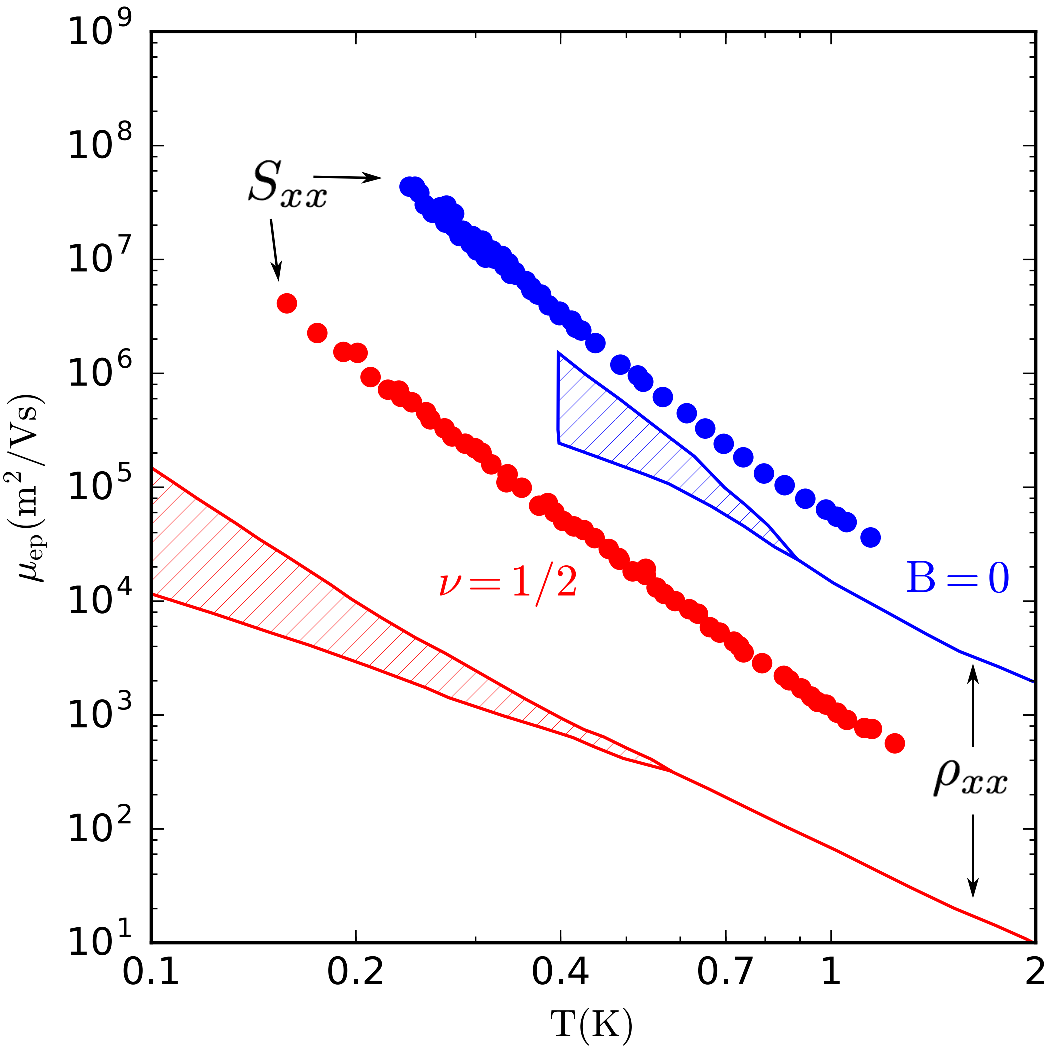

Figure 6.4: Experimentally determined μ_{e-ph} at B=0 and $\nu = 1/2$ from resistivity(solid lines and hatched areas, representing scatter in the data) and thermopower (closed circles). Figure based on reference [90], including resistivity data originally published in reference [89].

Summary

The electron-phonon interaction has been studied both experimentally and theoretically using many different approaches. At zero magnetic field, a theoretical model based on screened piezoelectric interaction has been experimentally validated. At higher magnetic field, and especially in the interacting regime, the picture is less clear. Finally, both theory and experiment agree that the strength of the electron-phonon interaction is enhanced by several orders of magnitude compared to its strength in the absence of magnetic field.

6.3 Model of electron diffusion and phonon scattering contributions in our device

In our specific heat experiments, the electron system is heated by a current passed through the 2DEG itself, raising its temperature relative to the phonons and contacts. At the same time, we use the temperature-dependent conductance of the 2DEG as a thermometer for the electron system. In order to predict whether electron diffusion or phonon scattering is the dominant cooling mechanism in the experiments, we use a simple model for the radial temperature profile in the device when heated by a radial current. The contacts are assumed to be at the same temperature as the phonons, and we define $\Delta T(r) = T_e(r) - T_{ph}$. The differential equation describing $\Delta T(r)$ is

$$\frac{\partial \Delta T(r)}{\partial t} = \frac{1}{c}\left[\kappa_{wf}\frac{1}{r}\frac{\partial}{\partial r}\left(r \cdot \frac{\partial}{\partial r}\Delta T(r)\right) + \frac{i^2}{(2\pi r)^2 \sigma_{xx}} - \kappa_{ph}\Delta T(r)\right], \tag{6.6}$$

which is simply the radially symmetric diffusion equation with additional terms representing dissipation to the phonon bath and input Joule heating. For this diffusion equation to be valid, we require that the electron mean free path is much smaller than the device dimensions. For sample CB05, the mean free path at $B = 0$ T is roughly 200 μm, while the inner and outer radii of the 2DEG are 250 μm and 1000 μm respectively. However, in a strong magnetic field, the *radial* mean free path is reduced by several orders of magnitude due to the Corbino effect (see Chapter 5). We assume that the contacts are at the same temperature as the phonon bath, and therefore use the boundary conditions $\Delta T(r_1) = \Delta T(r_2) = 0$.

The steady state solution is found by setting the left hand side to zero. The solution for electron diffusion only (setting $\kappa_{ph} = 0$) is

$$\Delta T(r) = \frac{P}{4\pi\kappa_{wf}} \frac{\log(\frac{r}{r_1}) \cdot \log(\frac{r_2}{r})}{\log(\frac{r_2}{r_1})}, \tag{6.7}$$

which is plotted in Figure 6.5a. In the case where electron diffusion is negligible, the electron-phonon term dominates, and the steady state solution is

$$\Delta T(r) = \frac{P}{2\pi\kappa_{ph}\log(\frac{r_2}{r_1})r^2}, \tag{6.8}$$

which is plotted in Figure 6.5b. Comparing the two cases, the hottest part in the diffusion case is near $r = 0.5$ mm, far from both contacts. In contrast, the hottest part in the phonon-cooled version is near the inner contact, where the current density (and thus, power density per unit area) is highest.

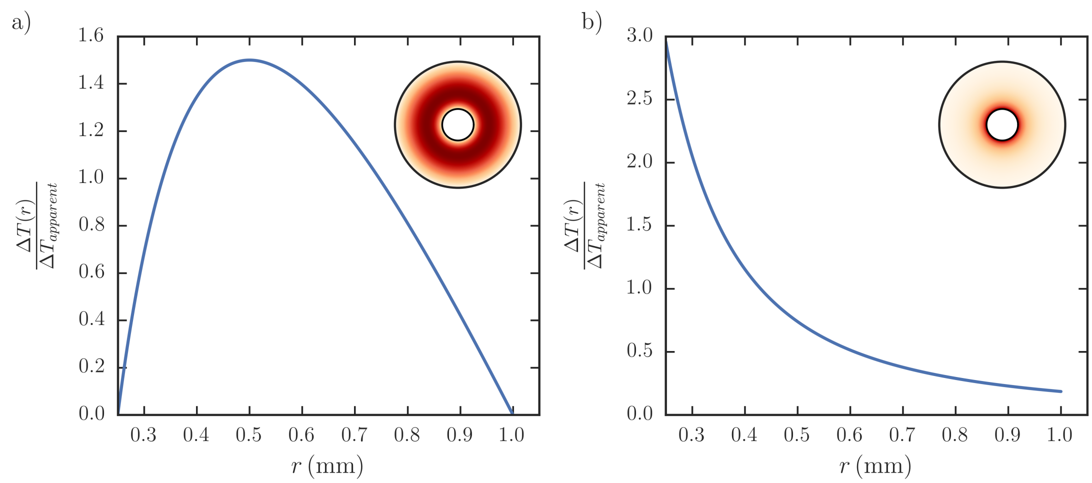

Figure 6.5: Analytical solutions for the temperature profile in our Corbino device under constant voltage bias. (a) Cooling through the contacts via electron diffusion. (b) Cooling through the electron-phonon interaction. Insets show the same data as 2D radial color plots.

Estimated relative contributions of electron diffusion and phonon emission

To simulate both diffusion and phonon emission simultaneously, we solve Equation 6.6 numerically for initial conditions $\Delta T(r, t = 0) = 0$ and boundary conditions $\Delta T(r_1) = \Delta T(r_2) = 0$. We then take the average of ΔT at each time step, weighted appropriately to account for the contribution to G at each radial position, in order to find the apparent temperature change, $\Delta T_{apparent}$, as measured by conductance (see Equation C.5 in Appendix C). From the asymptotic behaviour, we find the apparent thermal conductance, $K_{apparent} \equiv \Delta T_{apparent}(t \to \infty)/P_{applied}$. The thermal time constant, τ, is found by fitting an exponential to $\Delta T_{apparent}(t)$. We can also calculate the power flow to each of the contacts, which indicates the relative importance

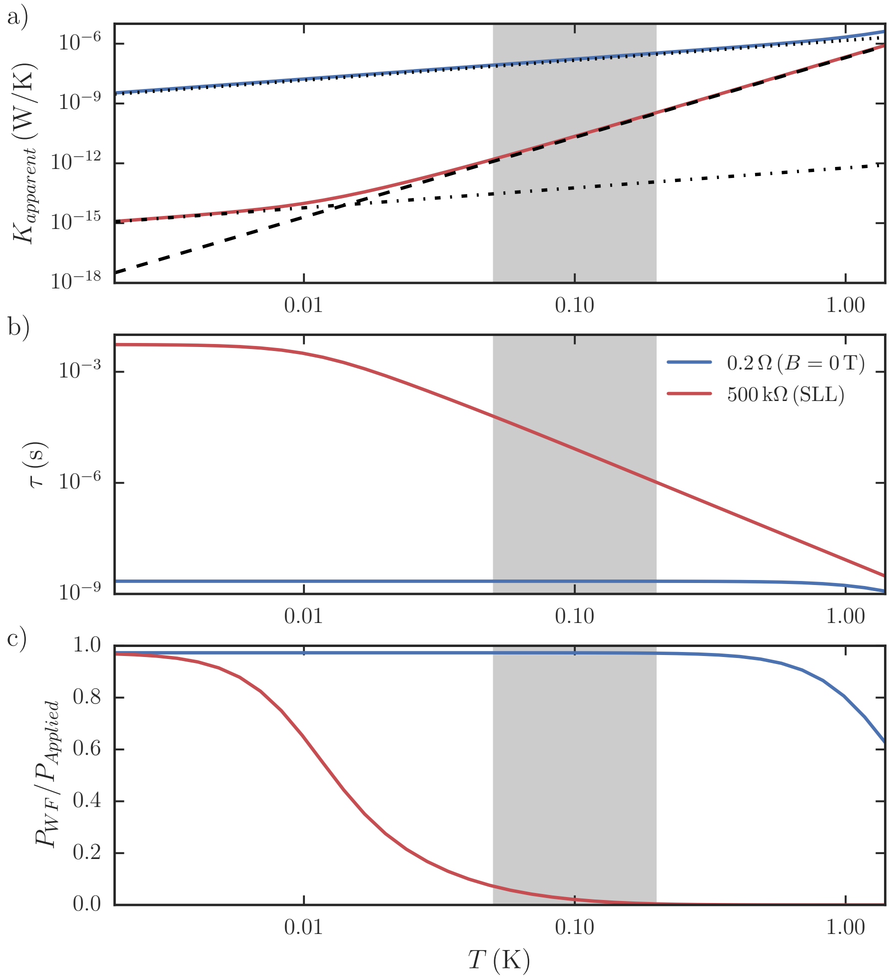

Figure 6.6: Calculated thermalization of a 2DEG with our usual sample geometry using both WF law and equation 6.6 for phonon power emission using a B=0 model. Blue lines correspond to 0.2 Ω resistance across the Corbino, as expected at B = 0 based on measurement of the sample's electron mobility. Red lines are calculated with 500 kΩ, which is a typical value observed at high magnetic field. Note that experimentally observed enhancement of the electron-phonon coupling at high magnetic field is not taken into account. a) K vs. temperature. The dotted line corresponds to WF law for 0.2 Ω, the dash dotted line corresponds to WF law for 500 kΩ, and the dashed line is the calculated $K_{apparent}$ for phonon emission. b) Thermal time constant, calculated using the B=0 theory for 2D electron specific heat. c) Fraction of total power leaving via the contacts in steady state (the remainder is emitted to the lattice). The shaded region in all panels is the approximate temperature range for our measurements.

of diffusion and phonon emission. The results of the calculation, using a realistic model of phonon emission at $B = 0$ T (Equation 6.4) and Wiedemann-Franz law for two example values of R_{total}, are shown in Figure 6.6.

In the absence of magnetic field, the high mobility of our sample allows electrons to rapidly diffuse to the contacts. In the blue curve in Figure 6.6a, we see that at low temperature, K follows the weak (linear) temperature dependence of electron diffusion. Correspondingly, τ is constant as shown in Figure 6.6b, and the fraction of power leaving via the contacts approaches 100% as shown in Figure 6.6c. This calculation shows similar behaviour to the experimental results of Appleyard *et. al.* [84] in a square sample of roughly the same area, in which they saw the crossover from phononic to electronic cooling at around 500 mK (see Figure 6.3).

Conversely, in a magnetic field our sample has a very large resistance between the two contacts, implying that electrons cannot easily diffuse to the contacts. As a rough estimate, we performed the same cooling calculation as before, but with 500 kΩ total resistance for the sample. The results are plotted as the red curves in all three panels of Figure 6.6. The crossover between cooling mechanisms is at a much lower temperature than in the $B = 0$ case, at around 20 mK. Previous measurements at high magnetic field, including in the SLL, suggest that the electron-phonon coupling is significantly enhanced [85–87, 89, 90]. Therefore, we expect electron diffusion to make a negligible contribution to thermalization in a strong magnetic field.

6.4 Summary

In the low temperature regime, the temperature of a 2DEG may differ from the temperature of the phonons in its host material. When heated by, for example, a current passing through the 2DEG, it may thermalize by either electron diffusion to the ohmic contacts or directly to the phonons via the electron-phonon interaction. Based on theory, previous experimental work and numerical modelling, the primary mechanism by which the 2DEG thermalizes in a mm-scale Corbino device is phonon emission, with electron diffusion only playing a major role at temperatures well below 50 mK.

Chapter 7

Specific heat and entropy in the second Landau level

As discussed in Chapter 3, specific heat is closely related to entropy, and measuring it holds promise as a means to detect the non-Abelian entropy at $\nu = 5/2$. In this chapter, I present measurements of the thermal relaxation time of the 2DEG, and the effective thermal conductance between it and the phonon bath, which together can be used to find its specific heat. The measurements were performed in the second Landau Level, including at $\nu = 5/2$. From this data, I also calculated $\mathcal{S}(T)$ and found it to be in excellent agreement with existing thermopower data taken by the Eisenstein group at Caltech. Although a more thorough study and lower temperatures would be required to detect the non-Abelian entropy, the technique is quite promising based on these results.

7.1 Experimental protocol

In order to determine the specific heat, c, we measure both the thermal relaxation time τ and the thermal conductance K. To measure τ, we opted for a time-domain experiment, where we observe the temperature change of the 2DEG (using its conductance as a thermometer) to a step change in applied Joule heating power. To measure K, we measure 2DEG temperature (again via conductance) as a function of DC heating power. In early iterations of the experiment, τ and K were measured in separate data runs, using a small applied voltage to measure the 2DEG's conductance as it cooled down after a larger voltage was turned off, and separately recording dv/di versus V_{DC}. However, I was able to optimize the experiment by instead determining both τ and K from a single dataset, as detailed in the remainder of this section.

7.1.1 Unipolar square wave scheme

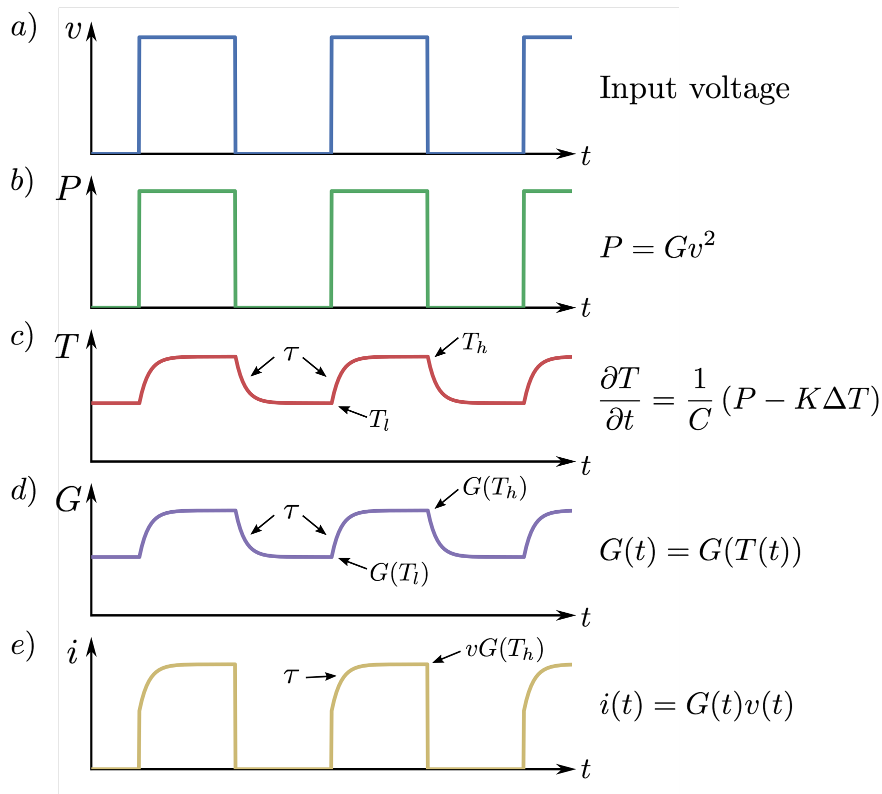

Figure 7.1: Applied unipolar square wave voltage excitation (a) results in a square wave in heating power (b). The temperature of the 2DEG (c) increases and decreases with a time constant τ. Its conductance (d) varies similarly. The resulting current (e) can be used to determine both τ and $G(T_h)$.

Rather than attempting to use a large voltage to drive heating and a small voltage to measure conductance, we introduce a simplified scheme where the voltage excitation is a unipolar square wave, as shown in Figure 7.1a. The resulting power dissipated in the 2DEG is also a square wave (to first order, *i.e.* neglecting changes in G), as shown in Figure 7.1b. The temperature of the 2DEG changes as a result, however it takes a time τ to warm up or cool down each time the power turns on or off (Figure 7.1c). Note that for small ΔT, the heating and cooling time constants are the same. The conductance of the 2DEG varies with its temperature (Figure 7.1d), but we can only observe it by measuring the current, $i(t)$, during the time that the voltage is on, as shown in Figure 7.1e. We can find τ by fitting an exponential to the $i(t)$ data. We can also measure $G(T_0, P)$, and in turn K, from the same $i(t)$

dataset by repeating the experiment for several values of P. Furthermore, these quantities are measured with the maximum possible applied voltage (the voltage used to heat the 2DEG), and therefore have an optimized SNR compared to a "pump-probe" experiment where a much smaller "probe" excitation is used to read out the differential conductance.

7.1.2 Extraction of K

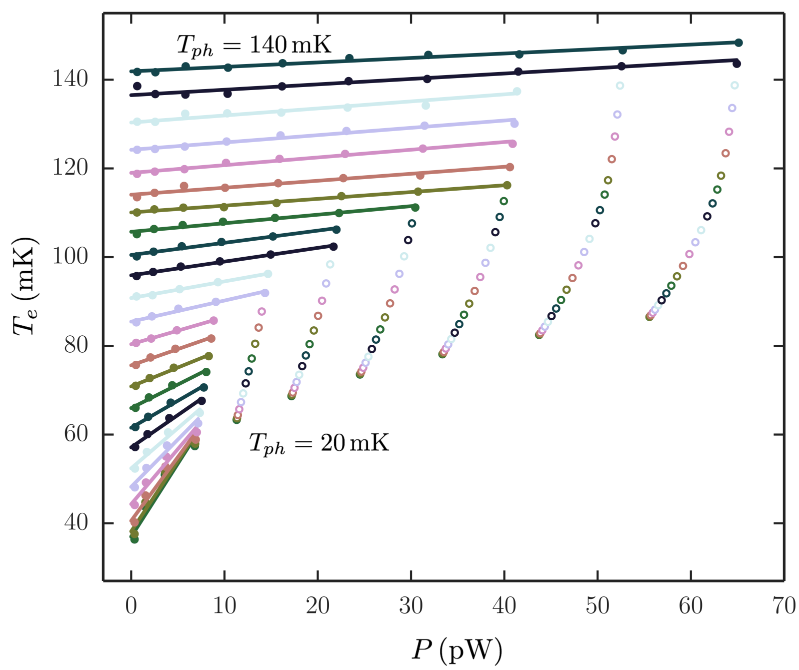

Figure 7.2: Electron temperature vs. Joule heating power at $\nu = 5/2$. Each data series corresponds to a different mixing chamber temperature (from 20 to 140 mK, in 5 mK increments). Voltage biases at each temperature were 0.5 to 5 mV in 0.5 mV increments. The linear fits were determined using either the first 4 data points, or those that result in a temperature change of less than 7 mK. Filled markers indicate data points used in the fit, while empty markers were omitted.

To obtain K from the square wave response data, we analyze the slope of T_e versus P in the low power limit. An example dataset is shown in Figure 7.2. Each set of points was obtained at a fixed phonon (*i.e.* substrate) temperature, with increasing applied voltage. For each combination of T_{ph} and P, the conductance G was found from the value of I_{meas}/V_{high} reached in steady state, at least 5τ after the voltage was turned on. We then fitted a cubic spline to T_e versus G for the lowest applied power, which was then used to infer T_e from G measured with larger applied power. Finally K for each phonon temperature was determined by fitting a line to $T_e(P)$ in the low power limit (either the first four points, or a maximum ΔT of 7 mK, as shown in Figure 7.2), and multiplied by a geometric correction factor of 1.83 applied as described in Appendix C.

7.1.3 Extraction of τ and data cleaning procedure

The thermal time constant τ is determined from the same square wave data set used to find K, by fitting an exponential function to the transient in conductance when the current is turned on. However, in addition to the thermal time constant, electrical resonances and time constants within the measurement setup may also modify the shape of the original square wave. These unwanted signal corruptions can be mitigated by time-shifting the signal by half a period and adding it to the original signal, as shown in Figure 7.3, before performing the exponential fit. This correction procedure works when the undesirable part of the signal is symmetric, in the sense that it is identical (up to a DC offset) when inverted and then shifted by half a period. For example, the response of a simple RC circuit to a square wave input is symmetric, so the nulling procedure reduces it to a flat line. In contrast, the thermal transient in the sample only appears in the "turn-on" step response and not in the "turn-off" response, and hence survives the subtraction procedure, as shown in 7.3b. One should be cautious though, since other combinations of non-linearity with frequency-dependence could also generate a signal that would appear in the output signal $i(t)$.

To help understand the effect of the nulling procedure in different situations, Figure 7.4 shows a block diagram of the measurement circuit, highlighting the different regions that may introduce time constants. The sample is assumed to be the only non-linear component (apart from the preamplifier, which has a finite bandwidth but is assumed to have negligible distortion). Coupling between the input and output sides of the circuit is modelled as "crosstalk", with the crosstalk contribution to the output voltage simulated by multiplying the input voltage by a factor γ. Figure 7.5 shows the result of applying the nulling procedure to the simulated output of the circuit for a variety of situations. If all time constants are extremely short (or zero, as in Figure 7.5a), the raw output signal is just a square wave like the input signal. In this case, the "shift-and-add" nulling procedure gives a flat DC

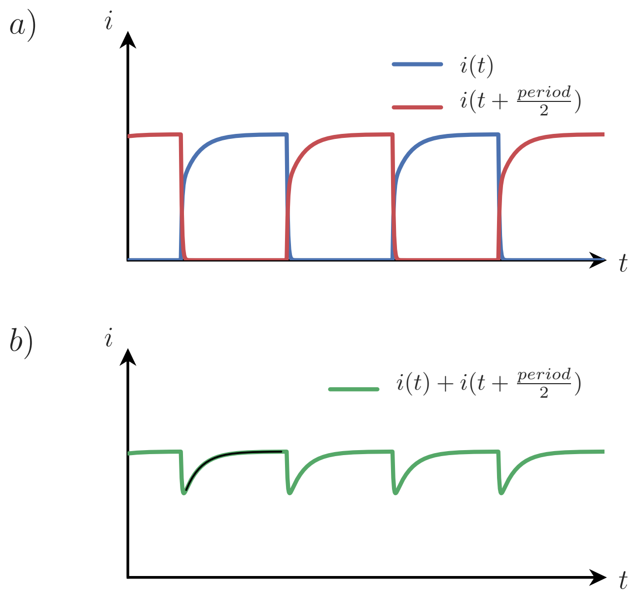

Figure 7.3: "Shift and add" procedure to null extraneous transients. a) Simulated raw signal and time-shifted signal on the same axes. b) Sum of the raw and time-shifted signals (green) and fitted exponential function (black).

output.

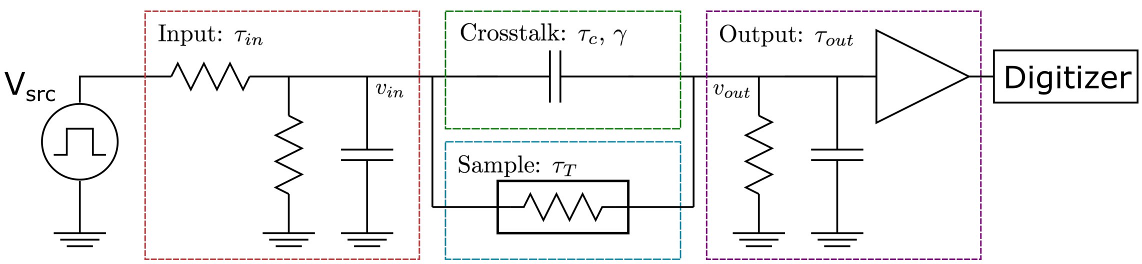

Figure 7.4: Simplified schematic diagram of the experimental setup showing the different regions (dashed line boxes) that could deform the input square wave due to thermal or electrical time constants.

If τ_{in} is non-zero, we have one of the most problematic cases to deal with. Since the square wave's shape is modified by τ_{in} *before* the nonlinearity of the sample is applied, the shape of the high and low parts of the waveform get scaled by different factors and cannot be cancelled out by the nulling procedure. For this reason, our experimental design uses a small 100 Ω resistor on the input side of the circuit and, based on the stray capacitance of the wiring, we estimate τ_{in} = 60 ns. Since this timescale is an order of magnitude faster than the thermal time constants we

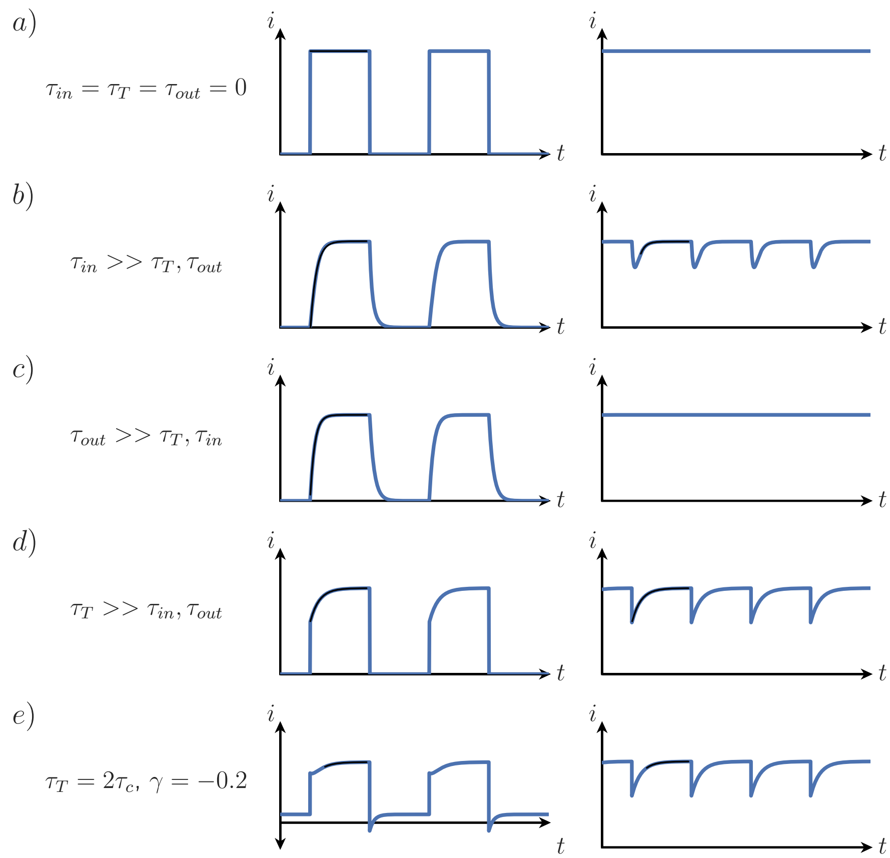

Figure 7.5: Simulated output for a simple model of the experiment. The first column shows the raw current output, while the second column shows the output after applying the shift-and-add procedure described in the text. a) With $\tau = 0$ for each part of the circuit, the output is simply a square wave, and can be nulled to a DC output. b) In the case where τ_{in} is large, the nonlinearity in the sample allows the transient to survive the nulling procedure. c) If the time constant is on the output, after the nonlinear element, the transient can be fully nulled out. d) If the sample itself is the source of the time constant, the transient fully survives the nulling procedure, as desired. e) Additional direct *linear* coupling between the input and output sides of the circuit can lead to odd-looking raw data, but can be fully cleaned up by the nulling procedure.

observed, it is not expected to affect our experimental results.

If τ_{out} dominates, the situation is not as bad, since the square wave sees the non-linearity of the sample before being modified by τ_{out}. Because the signal remains symmetric, the "shift-and-add" procedure can completely null the signal in the $\tau_T << \tau_{out}$ case. However, τ_{out} still provides a bandwidth limitation for the experiment.

If τ_T is the dominant time constant, the thermal transient perfectly survives the nulling procedure, as shown in Figure d. Furthermore, if some current passes directly from the input to the output side of the circuit due to crosstalk (*e.g.* capacitive coupling, mutual inductance, ground loops, RF), those (presumably linear) effects can be completely nulled out as shown in Figure 7.5e.

7.1.4 Example raw data

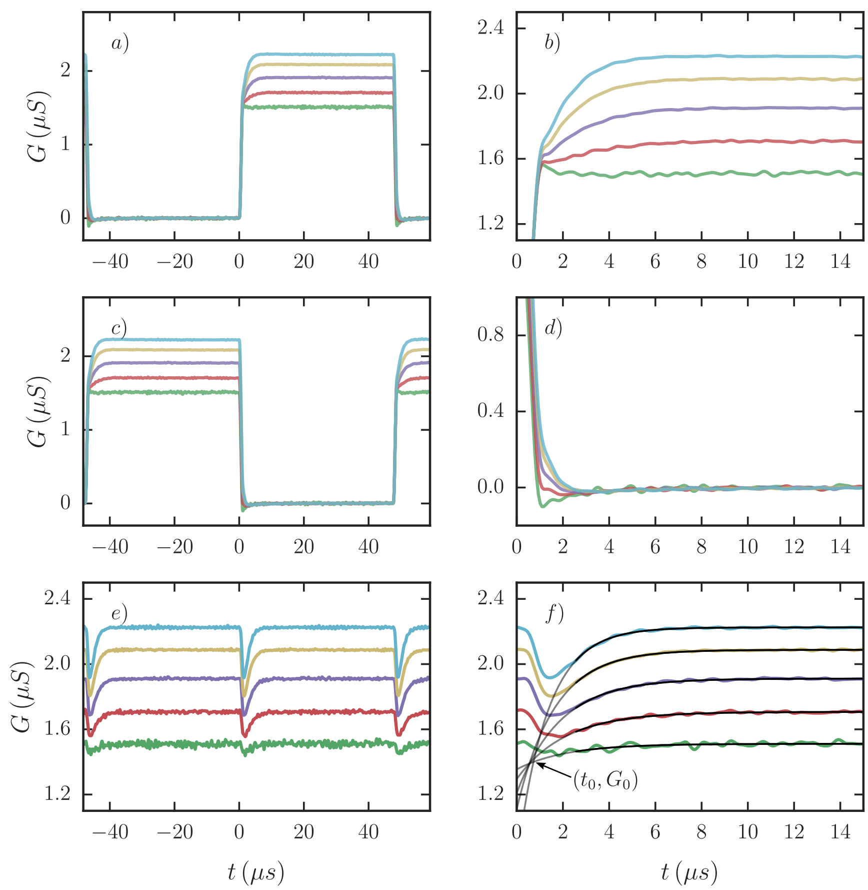

Figure 7.6: Response of sample to square wave with $V_{low} = 0$ mV and $V_{high} = 1$ mV (green), 2 mV (red), 3 mV (purple), 4 mV (yellow) and 5 mV (cyan). (A) and (B) show the response to the voltage turning on. (C) and (D) are shifted by half a period, such that (D) shows the "turn-off" to 0 mV bias. (E) and (F) are obtained by adding the original and time-shifted signals, in order to cancel any voltage transient (due to, for example, LCR resonances in the wiring). The black lines in (F) are exponential fits to each curve. Extrapolation of the curve beyond the fitting range, towards $t = 0$, is shown in dark grey.

Measurements were performed using setup C, as described in section 4.4.3, and sample CB05. Experimental time traces at $\nu = 5/2$ are shown in Figure 7.6 for a series of excitation voltages. The raw data, resulting from averaging $\sim 10^6$ iterations of the square wave excitation, is shown in panels a and b. The time-shifted version, required for the nulling procedure outlined in the previous section, is shown in panels c and d. Finally, the results of the nulling procedure are shown in panels e (the sum of panels a and c) and f (the sum of panels b and d). Exponential fits, from which τ is extracted, are shown in panel f.

Importantly, the exponential fits all extrapolate to intersect at nearly the same point, labelled (t_0, G_0), which strongly suggests that the dominant non-linearity in the sample turns on with a single time constant τ. If there were some other faster non-linearity, such as a diode-like effect at the contacts, the fits would not appear to emanate from a single point. Instead, they would already be shifted relative to one another at t_0. This observation supports the use of $G(P, T_0)$ to find T_e, and by extension K.

7.2 Results

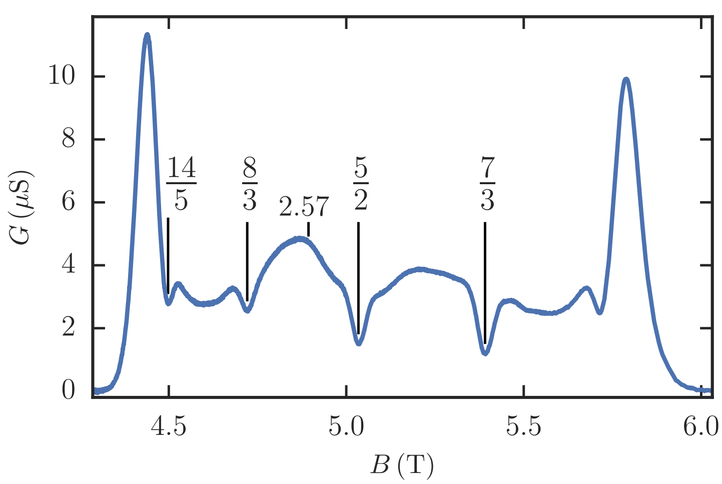

Figure 7.7: a) Conductance at base temperature. Labeled filling factors indicate where measurements of τ, K and C were performed.

The experimental procedure discussed in the preceding section was used to gather data for several filling factors in the SLL at refrigerator temperatures ranging from 20 mK to 140 mK. The specific filling factors are marked on Figure 7.7, which shows the sample's conductance at base temperature. In addition to the four marked FQH states, the experiment was also performed at $\nu = 2.57$, where we observed a strong *increase* of conductance with decreasing temperature (whereas the opposite is observed in FQH states). Within the temperature range of our experiment, we did not observe the re-entrant integer quantum Hall state, conventionally labeled R2c [92], that has previously been reported at the same filling factor at lower temperatures [93]. Data at a fifth FQH state, $\nu = 11/5$, which is visible as a sharp dip to the right of $\nu = 7/3$, are not available due to a technical issue during the data collection run.

7.2.1 Thermal conductance to the environment

We first turn our attention to the measurements of K, which are shown in Figure 7.8. We find that K has the same order of magnitude and a similar temperature dependence across filling factors, with $\nu = 2.57$ showing the largest deviation from the rest. As discussed in Appendix C, if cooling were primarily through electron diffusion, we would expect $K = 12GL_0T \approx 10$ fW/K, which is several orders of magnitude smaller than what we observe. Although this means that diffusion of charged quasiparticles is not the dominant cooling mechanism, it is still possible that there could be cooling by diffusion of *neutral* quasiparticles [75], which are not believed to obey the Wiedemann-Franz law. Moreover, being chargeless, they would also be immune to the Corbino effect and may diffuse more easily, even in a strong magnetic field. However, one would expect the formation of neutral quasiparticles to be highly dependent on filling factor, while our results for K are quite consistent throughout the second Landau level. Therefore, a more likely explanation is a cooling process due to phonon emission.

In chapter 6, we discussed a model for the cooling rate of a 2DEG due to phonon emission. Recasting equation 6.4 in terms of K, and substituting in the area and electron density of our sample, we would expect $K = 370\ T^4$ [nW/K], or 37 pW at 100 mK. Our measured value of K is about two orders of magnitude larger, which is consistent with the enhanced phonon emission rates seen at high magnetic field in previous experimental studies [87, 89, 90]. A theoretical study of the CF-phonon interaction also predicts it to be much stronger than the electron-phonon interaction [91].

Besides the magnitude, it is also interesting to look at the exponent of the temperature dependence of K. The inset of Figure 7.8 shows K vs T on a log-log scale, as well as straight lines with slopes corresponding to T^3, $T^{3.4}$ and T^4 dependencies. The T^4 slope, expected for the zero-field model, is clearly steeper than our data, while the T^3 slope, corresponding to a hydrodynamic model discussed by Chow *et al.* [87] is too shallow. The slope of our data lies somewhere in between, around $T^{3.4}$. A more detailed theoretical analysis of K than either model would have to take into account the gapped DOS at FQH minima, rather than assuming a flat DOS as at $B = 0$.

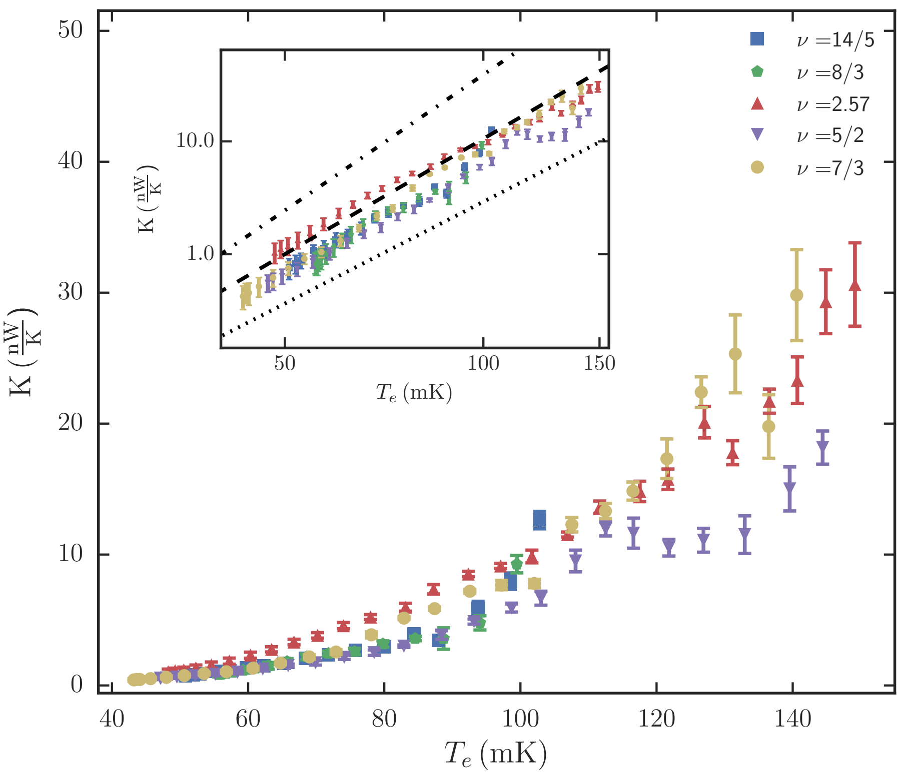

Figure 7.8: Thermal conductance to the environment as a function of temperature for several filling factors in the SLL. The inset shows the same data on a log-log scale with lines, at arbitrary vertical positions, indicating slopes of 3 (dotted), 3.4 (dashed) and 4 (dot-dashed).

7.2.2 Thermal relaxation time

Measurements of the 2DEG's thermal relaxation time are shown in Figure 7.9. The data was obtained by fitting an exponential function to the plot of conductance vs time, after performing the nulling procedure outlined in section 7.1.3. For each data point, the electron temperature was inferred from the final conductance

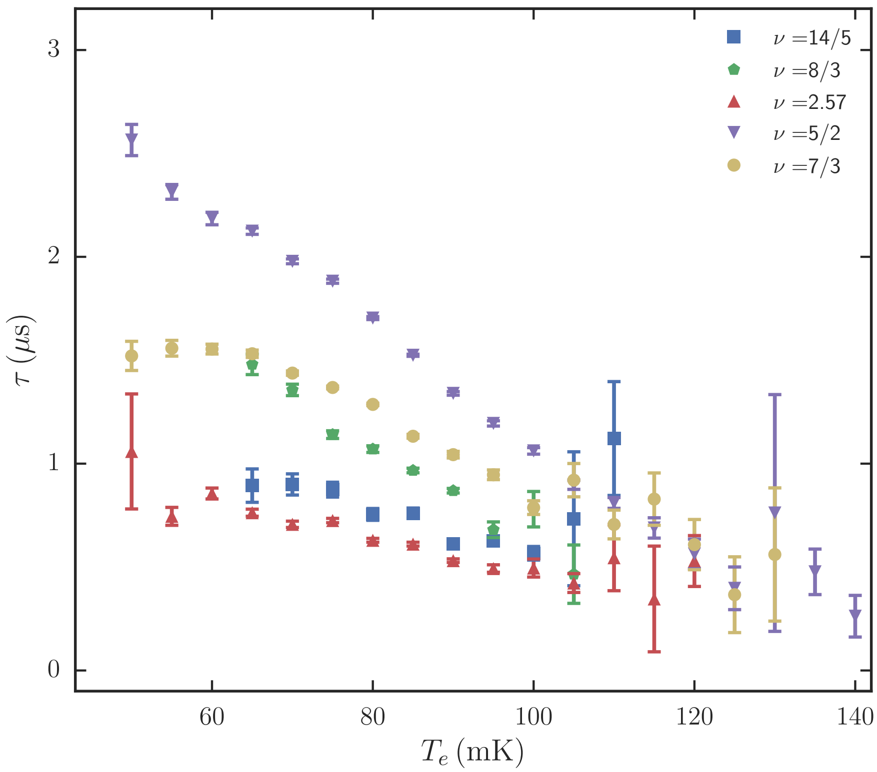

Figure 7.9: Thermal relaxation time τ measured as a function of T_e (as calculated from conductance measurements). Data from multiple phonon temperatures have been binned based on T_e in 5 mK bins and averaged.

reached, rather than the temperature of the sample stage. Data from multiple runs were then binned in 5 mK increments.

Previous estimates of τ were based on measurements of K and the assumption that $C(T)$ takes its zero-field value and temperature dependence [85–87]. To my knowledge, our measurements reported here are the first *direct* measurements of the thermal relaxation time of a 2DEG in the fractional quantum Hall regime. We find that, as expected, τ decreases with increasing electron temperature. There is some variation in τ between different filling factors, with $\nu = 5/2$ having the longest relaxation time, followed by $\nu = 7/3$ and $\nu = 8/3$, which are quite similar to each other. The differences between filling factors may be due to differences in the size, charge, density and screening of quasiparticles.

7.2.3 Specific heat

Having directly measured both τ and K, we are able to determine C, the heat capacity of the 2DEG via the formula $C = K\tau$. Since the size of the sample is arbitrary, we instead report the specific heat per electron in units of k_B, defined as $c \equiv C/k_B N_e$. The results for each filling factor are plotted in Figure 7.10b, alongside corresponding plots of $G(T_e)$ in Figure 7.10a. At most filling factors, both c and G increase monotonically with temperature. However, at $\nu = 2.57$, G decreases with increasing temperature, even as c increases. We will revisit this result later in this chapter when we discuss the entropy of the 2DEG.

In order to better understand the data, we can begin by considering the specific heat of a non-interacting fermi liquid,

$$c = \frac{\pi m^* k_B T}{3\hbar^2 n_q}, \tag{7.1}$$

where m^* is the effective mass of the fermions, and n_q is the quasiparticle density. In a GaAs heterostructure at $B = 0$, the relevant quasiparticles are electrons with band effective mass $m^* = 0.067 m_e$. The calculated $B = 0$ specific heat, shown by the dashed lines in Figure 7.10b, is substantially lower than any of the measured values for c. However, in the fractional quantum Hall regime, the relevant effective mass is not the electron band effective mass. Instead, it might make more sense to consider the effective mass of composite fermions, which has previously been estimated to be $1.3m_e$ at $\nu = 3/2$ from thermopower data [40], and between $0.7m_e$ and $1.2m_e$ (depending on density) at $\nu = 1/2$ in cyclotron resonance measurements [94]. Assuming m_{CF} around $\nu = 5/2$ is of a similar order of magnitude, we have plotted equation 7.1 again using $m^* = m_e$ and $n_q = n_e$ as the dotted line in each panel of Figure 7.10b. The calculation roughly captures the magnitude of the specific heat data, however there is clear deviation from simple linear behaviour at most filling factors. This deviation is expected, since the model in equation 7.1 is for a simple Fermi liquid with a flat density of states, while gapped FQH states occur at most of the measured filling factors. Instead, we can consider the following toy

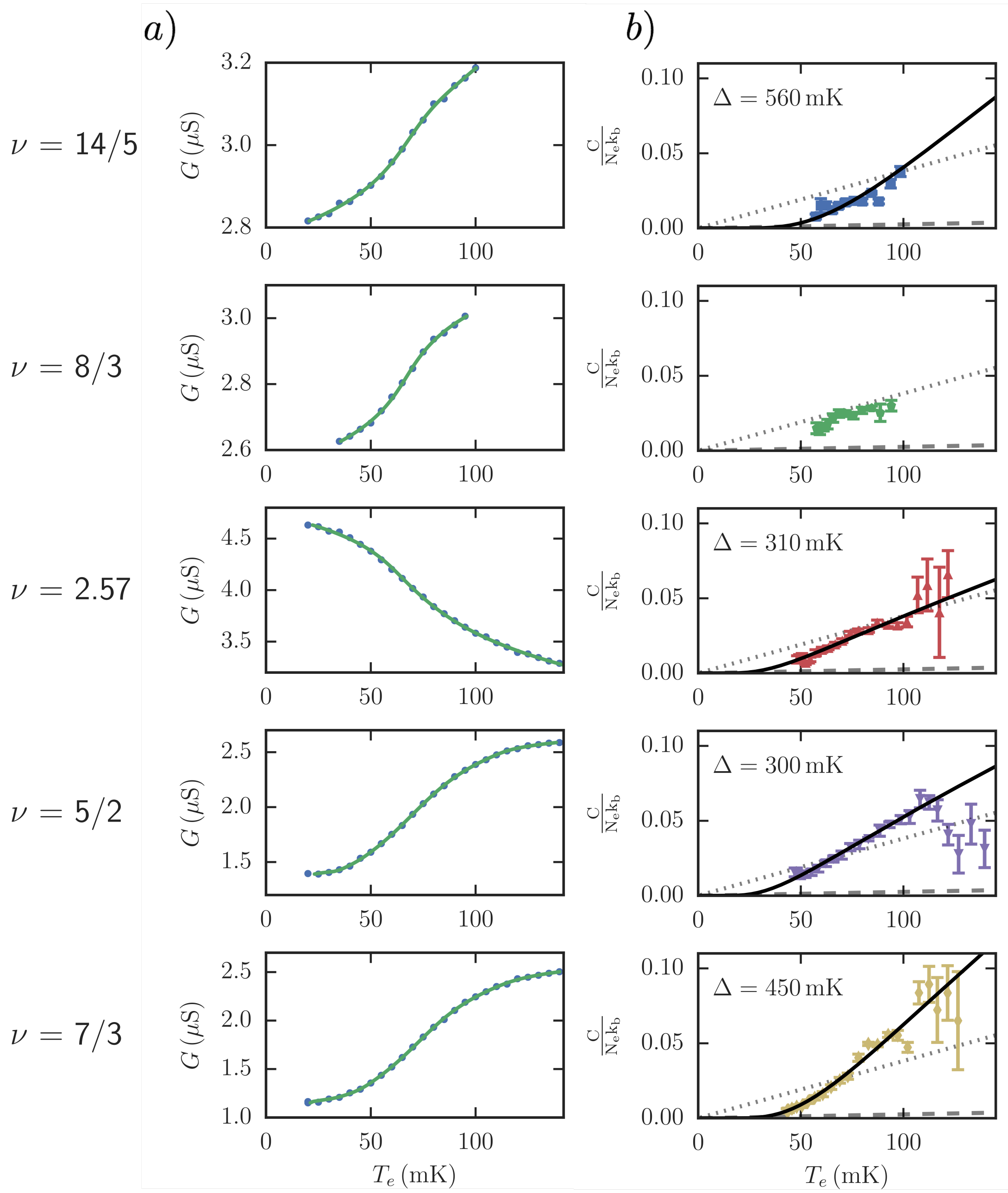

Figure 7.10: (a) Conductance vs. temperature for several states in the SLL. (b) Specific heat vs. temperature at the same set of filling factors. Fits to equation 7.3 are shown by the solid black lines, and the resulting Δ's are given on each plot, while $g_0 k_B/n_e = 0.18$, 0.12, 0.16 and 0.25 K^{-1} for $\nu = 14/5$, 2.57, 5/2 and 7/3, respectively. The dotted line is the specific heat for free 2D electrons ($m^* = m_e$), while the dashed line is the specific heat for 2D electrons in GaAs at zero field ($m^* = 0.067m_e$).

model for a gapped DOS:

$$g(\epsilon) = \begin{cases} g_0 & : \epsilon < \epsilon_f - \Delta/2 \\ 0 & : \epsilon_f - \Delta/2 < \epsilon < \epsilon_f + \Delta/2 \\ g_0 & : \epsilon > \epsilon_f + \Delta/2. \end{cases} \quad (7.2)$$

This model represents a DOS given by two flat regions separated by a gap Δ, with the fermi level exactly in the middle of the gap. The corresponding specific heat is

$$c = \frac{2g_0}{n_e}\left(\frac{\Delta^2}{4k_BT} + \Delta + 2k_BT\right)e^{-\Delta/2k_BT}, \quad (7.3)$$

which, when fitted to the data, yields the black curves in each panel of Figure 7.10b. Based on these fits, we find Δ between 300 mK and 570 mK for the different filling factors. We can also estimate the quasiparticle effective mass from the fits, using the equation

$$m^* = \pi\hbar^2 g_0. \quad (7.4)$$

The resulting values are $m^* = 1.4m_e$ at $\nu = 5/2$ and $m^* = 2.1m_e$ at $\nu = 7/3$. An alternative to Equation 7.3 is to use a standard Arrhenius plot to fit the data, as shown in Figure 7.11, which yields similar values for Δ.

7.2.4 Comparison of Δ from specific heat to Δ from conductance

The values of Δ extracted from the specific heat are much larger than those obtained from conventional Arrhenius fits to the conductance, which are shown in Figure 7.12a. In particular, from specific heat we find $\Delta = 300$ mK at $\nu = 5/2$ and $\Delta = 450$ mK at $\nu = 7/3$, whereas the corresponding values from conductance are 103 mK and 131 mK respectively. The origin of the small measured energy gaps in the second Landau level, relative to those calculated either by exact diagonalization or numerically [48], has been a longstanding question in the study of the second Landau level. One possible explanation is that the apparent gap inferred from conductance data is reduced due to the details of conductance in the presence of disorder. In a model put forward by d'Ambrumenil *et. al* [68], they consider transport through a disorder potential, which is limited by the necessity for the quasiparticles to move across the saddlepoints separating "valleys" in the potential landscape. They further provide a method to calculate the saddle-point gap, Δ_s, from the value of Δ obtained from the Arrhenius plot of conductance along with T_i, the temperature of the inflection point in the same Arrhenius plot. Using their method, we obtain the values $\Delta_s = 300$ mK and 330 mK for $\nu = 5/2$ and $\nu = 7/3$, respectively, which are in much better agreement with the gaps obtained from the specific heat data. This suggests that using the specific heat may be more accurate than conductance as a means to determine Δ, which makes sense, since the former is a direct thermodynamic measurement while the latter may be affected by the details of transport in the system.

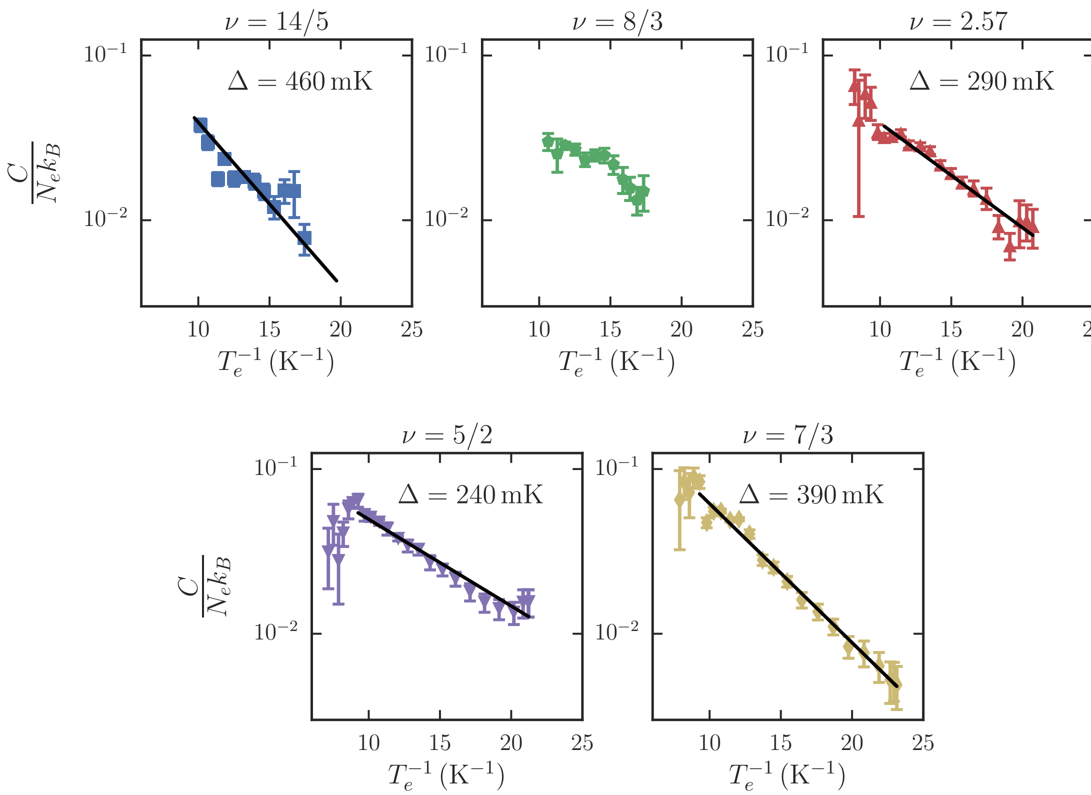

Figure 7.11: Arrhenius fits to c in the SLL.

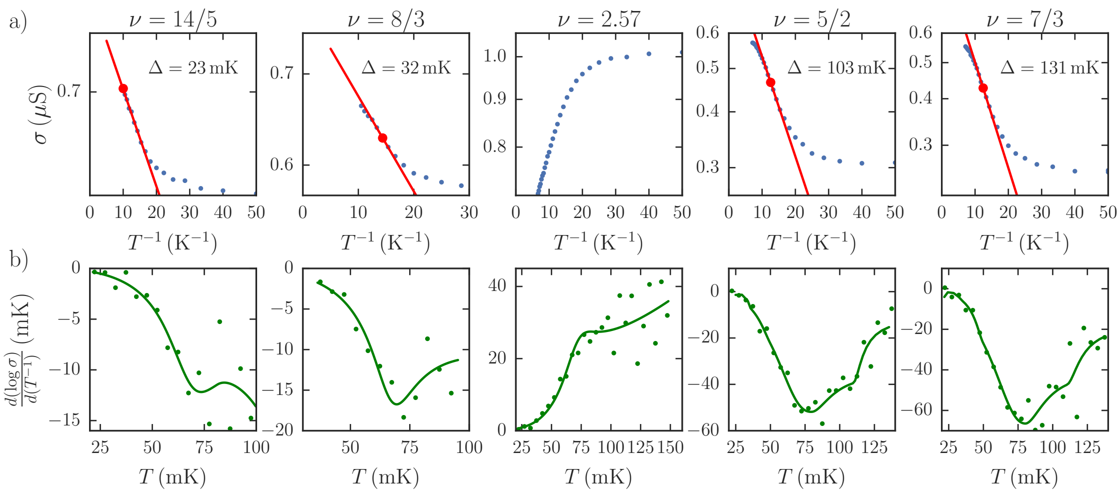

Figure 7.12: (a) Arrhenius fits to the conductivity at each indicated filling factor, with data in blue and linear fit to the activated region in red. The inflection point is marked by a red circle. (b) Corresponding plots of the Arrhenius slope vs. temperature, with data as points and a smoothed spline interpolation in green. The minima give $-\Delta/2$, and their locations in temperature give T_i.

7.2.5 Entropy

The entropy of the 2DEG can be found (up to a constant) from the heat capacity by integrating over temperature according to the equation

$$S(T) - S_0 = \int_{T_0}^{T} \frac{C}{T'} dT', \tag{7.5}$$

where S_0 is the entropy at T_0. As previously discussed in Chapter 3, the longitudinal thermopower S_{xx} can also be used to find the entropy via the relation

$$S_{xx} = -\frac{\mathcal{S}}{|e| n_e}, \tag{7.6}$$

which is valid in the clean limit [39]. In Figure 7.13, we plot $\Delta\mathcal{S} = \mathcal{S}(T) - \mathcal{S}_0$, measured at $\nu = 5/2$ and $\nu = 7/3$ obtained in two different ways: from our specific heat data (via numerical integration of $\frac{C}{T}$ data points, using the trapezoidal rule), and from thermopower data reported by Chickering *et. al.* (Figure 2 of ref [43]). In the case of the heat capacity data, $\Delta\mathcal{S}$ is simply found by calculating the right-hand side of equation 7.5. For thermopower, we use linear interpolation to find $S_0 = S_{xx}(T_0)$, where $T_0 \approx 45$ mK is the lowest temperature at which C was measured, and subtract that offset from all the S_{xx} data. The results from these two different techniques are in excellent agreement at both filling factors, strengthening the case that their interpretation in terms of entropy is correct.

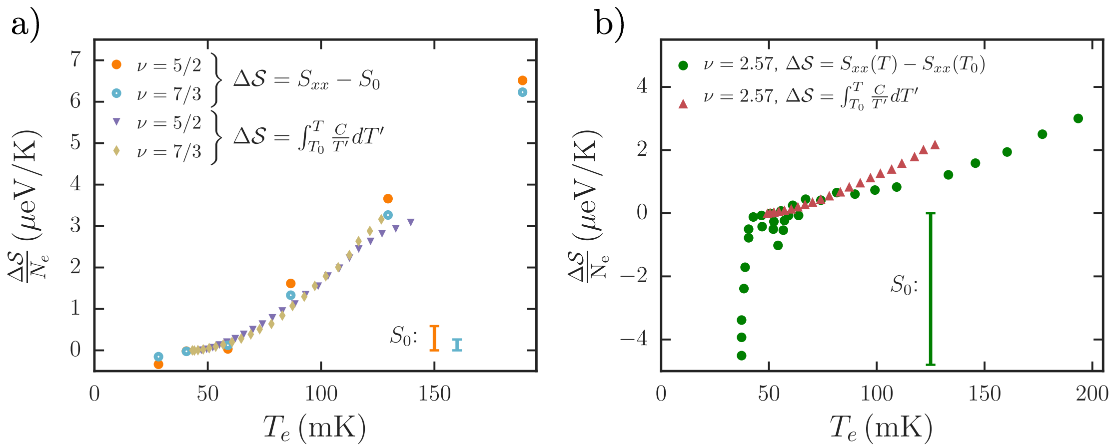

Figure 7.13: Entropy as determined from longitudinal thermopower data [43] and from integration of our specific heat measurements. The thermopower data is offset such that $\Delta\mathcal{S} = 0$ at the lowest temperature for which we measured C. a) Entropy at $\nu = 5/2$ and $\nu = 7/3$. The thermopower data is shifted by the offsets $S_0 = 0.58\,\mu\text{V/K}$ and $S_0 = 0.26\,\mu\text{V/K}$ at $\nu = 5/2$ and $\nu = 7/3$, respectively, as shown by the scale bars on the figure. b) Entropy at $\nu = 2.57$, including the onset of the re-entrant state $R2c$ in the thermopower, but not within the temperature range over which specific heat was measured. The thermopower data is shifted by $S_0 = 4.8\,\mu\text{V/K}$, which is the value of S_{xx} measured at $T_0 = 50$ mK (the lowest temperature where c was measured).

One puzzling aspect of the specific heat data is the activation-like behaviour of c at $\nu = 2.57$ in Figure 7.10, where there is no FQH gap. However, this result is in qualitative agreement with the thermopower data measurements by Chickering *et. al.*, as shown in Figure 7.13b. The thermopower data (green circles) shows a step in S_{xx}, corresponding to onset of the re-entrant state $R2c$. We do not observe the onset of the $R2c$, which would appear as a peak in c, within our measured temperature range (red triangles in Figure 7.13b). This is consistent with our conductance data, in which R2c was also not observed. However, at higher temperatures both the S_{xx} and c data increase super-linearly, in qualitative agreement with one another. The increase of $\mathcal{S}$ we observe with temperature is higher than that seen in the thermopower measurement, but is of a similar order of magnitude. The difference may be due to variation between the samples: the reentrant states are highly sensitive to sample quality and preparation (*i.e.* whether and for how long an LED was used to illuminate the sample during the cooling procedure). It would be interesting to measure the specific heat through the temperature regime where the step in S_{xx} was observed, and see whether there is a corresponding spike in c.

7.3 Summary

In this chapter, we introduced a novel experimental approach to measuring the specific heat of a 2DEG in the quantum Hall regime. By taking advantage of the thermal "weak-link" between the electrons and the phonons, and measuring on a short enough timescale, we were able to determine both the thermal relaxation time of the 2DEG and its thermal conduction to the environment. Specific heat data for several filling factors in the SLL were obtained, including at $\nu = 5/2$ and $\nu = 7/3$. Integration of the specific heat to obtain entropy yielded results in excellent agreement with previous measurements of the entropy via thermopower, demonstrating the potential of the new experimental technique.

Chapter 8

Conclusion and future work

8.1 Conclusion

8.1.1 Transport in the Corbino geometry

We have reported the first Corbino-geometry transport measurements in the second Landau level, including the 5/2 FQHE. Since our work in GaAs was originally published [3], Corbino geometry devices in graphene were shown to exhibit enhanced FQHE signatures compared to Hall bar devices [95, 96]. In contrast, our GaAs/AlGaAs device exhibited behaviour similar to that previously observed in non-Corbino devices fabricated from similar wafers. We did not observe novel or significantly enhanced phenomena compared to Hall geometry transport measurements, however we have demonstrated the viability of ultra-high mobility Corbino samples as a tool to study the fractional quantum Hall effect in the bulk.

8.1.2 Specific heat of a 2DEG in the quantum Hall regime

Using our Corbino sample and a novel technique, we were able to achieve the first reported measurement of the specific heat of a 2D electron system in the quantum Hall regime, in absolute units with no phonon contribution. Our technique is based on *in-situ* Joule heating of the 2DEG, and measurement of its temperature using electrical conductivity. By measuring the timescale for thermal relaxation (on the order of microseconds) and the electron-phonon thermal conductivity (typically on the order of pW/mK), we were able to determine c from a simple thermal RC circuit model. We observed an activation-like behaviour of c, with gap energies of 300 mK and 450 mK for $\nu = 5/2$ and $\nu = 7/3$ respectively. These values are considerably higher than those determined from standard Arrhenius fits to the conductance. The discrepancy appears to be resolvable by considering a more detailed theory of conductance that takes into account the role of disorder in transport. This suggests that c may provide a more direct measurement of the true bulk gap energy than transport.

By integrating c/T over temperature, we were also able to determine the entropy of the 2DEG up to a constant of integration, $\mathcal{S}_0$. Our results are in striking agreement with the entropy according to thermopower measurements by the Eisenstein group. This provides encouraging evidence that both experiments are correctly measuring the entropy of the 2DEG.

8.2 Future Work

8.2.1 Mapping out c in the 5/2 FQH

The logical next step for the specific heat experiment is to perform the measurements as a function of temperature and filling factor near 5/2. It may be possible to reach lower electron temperatures through improved filtering and heatsinking. Measurement setup D (presented in Chapter 4) was not used for SLL specific heat measurements, and promises a significant enhancement in SNR. One could take advantage of that to use a smaller excitation, which would be required to reach lower temperature and obtain more accurate results with a smaller ratio $\Delta T/T$.

8.2.2 Adiabatic cooling

The initial motivation for the experiments described in this thesis was to observe adiabatic cooling, rather than specific heat. Having measured the thermalization time constant ($\sim 1\,\mu$s) and specific heat of the 2DEG in the second level, in appendix D we present a calculation of the expected adiabatic cooling due to non-Abelian anyons. At and above 50 mK, the signal would be far too small to detect, but the experiment may nonetheless be viable in the few mK temperature regime in a device with the appropriate geometry.

8.2.3 Thermopower in the Corbino geometry

Having demonstrated successful fabrication of a Corbino geometry device that exhibits the $\nu = 5/2$ FQHE, it would be interesting to continue our fabrication efforts to develop a device suitable for thermopower studies. In appendix E, we present some preliminary investigations of thermopower using *in situ* Joule heating to create the thermal gradient, as well as other phenomena with very similar qualitative signatures. These experiments are somewhat difficult to interpret and disentangle, requiring more systematic study to obtain meaningful results.

8.3 Final words

This thesis has made a strong case as to why the entropy of a 2DEG is worth measuring, demonstrated the usefulness the power of the Corbino geometry, and provided a blueprint and inspiration for future measurements. Whether by continuing along the path of measuring specific heat, or by implementing some of the other proposed experiments to measure entropy, moving beyond charge transport can provide new insights into the exotic physics of the fractional quantum Hall regime.

Appendix A

Samples

A.1 Corbino geometry devices

All samples used in this thesis were GaAs/AlGaAs heterostructures grown by molecular beam epitaxy (MBE) at either Princeton University or Sandia National Laboratories. The Corbino devices have an inner contact radius $r_1 = 0.25$ mm, outer contact inner radius $r_2 = 1.0$ mm and outer contact outer radius $r_3 = 1.5$ mm. Fabrication details are described in reference [3]. Fabrication of CB01 and CB05 was carried out by Simon Bilodeau and Keyan Bennaceur respectively.

Table A.1: Samples used in this thesis

Name	Wafer	Grown at	$n_e\,(\mathrm{cm}^{-2})$	$\mu\,(\mathrm{cm}^2/\mathrm{V}\cdot\mathrm{s})$	QW width (nm)
CB01	VA142	Sandia	4.6×10^{11}	1.0×10^{6}	30
CB05	3.11.10.2	Princeton	3.0×10^{11}	2.5×10^{7}	30

A.2 Hall Bar Device HB01

A gated Hall bar device was used for some experiments described in Appendix E. This fabrication of the device at Sandia national laboratories was previously described in reference [97], and a representative photograph is reproduced in Figure A.1.

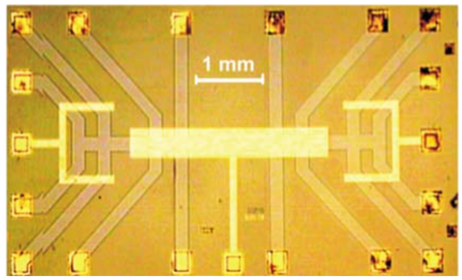

Figure A.1: Photograph of a gated Hall bar, similar to the one used in Appendix E. Reproduced from reference [97].

Appendix B

Wiring Diagram

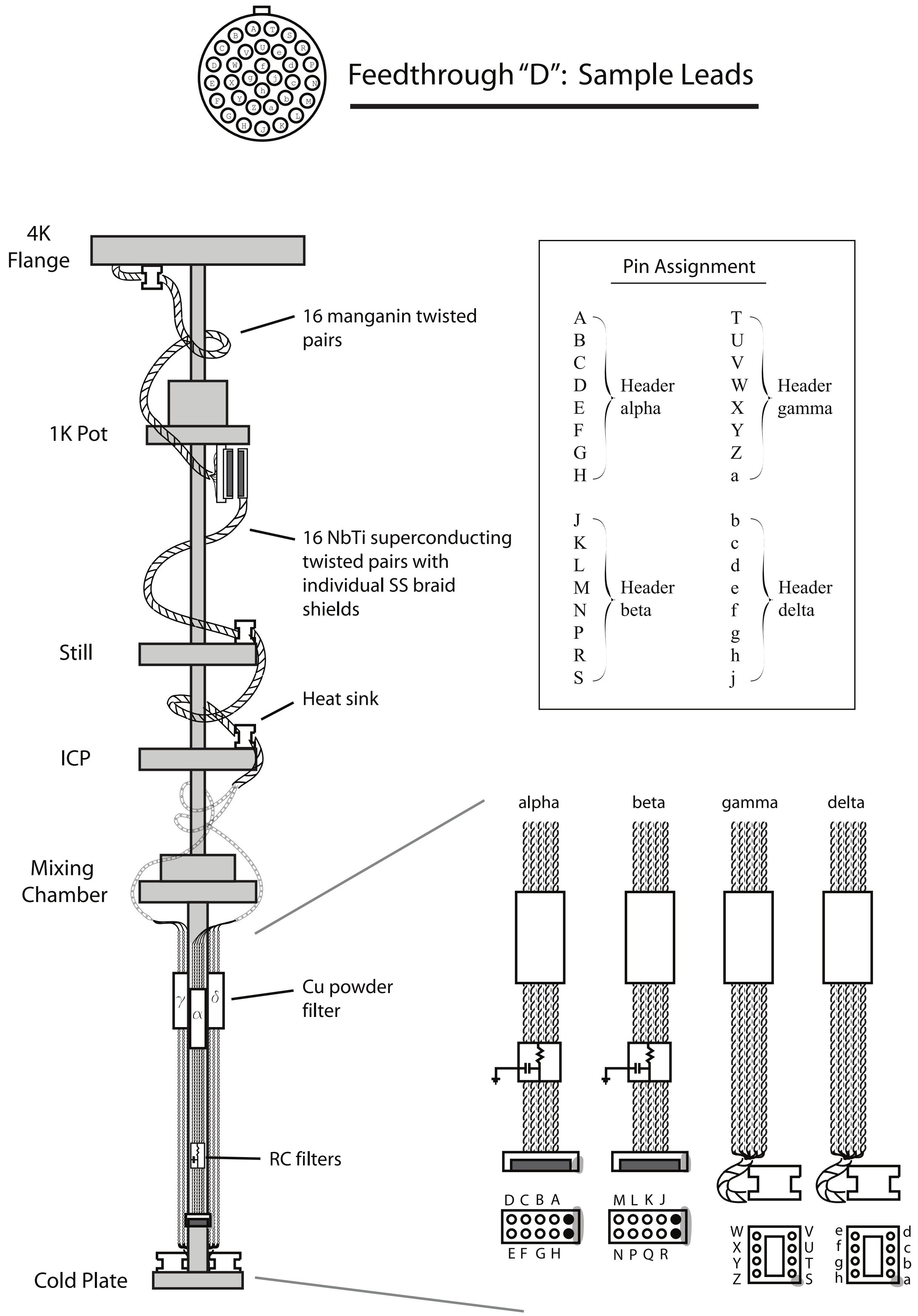

Figure B.1: Sample wiring schematic and pinout. Figure reproduced with permission from [8].

Appendix C

Geometric correction factor for the Corbino geometry

In our conductance thermometry scheme, we infer an apparent (small) temperature change using the equation

$$\Delta T_{apparent} = \left(\frac{dG}{dT}\right)^{-1} \times \Delta G, \tag{C.1}$$

where ΔG is the total conductance across the device, and dG/dT is found from the slope of $G(T)$ measured at low excitation power. However, as discussed in Chapter 6, the temperature change due to self-heating in the device is non-uniform, due to the non-constant current density in the Corbino geometry. More power is dissipated per unit area close to the centre contact than at the outer edge, resulting in a higher temperature. Additionally, heat escapes either to the phonon bath throughout the sample, or only to the contacts in the case of electron diffusion. The very different temperature profiles for these two cases are shown in Figure 6.5. The apparent temperature inferred from ΔG is thus not simply the mean temperature of the device, but rather the average weighted appropriately to account for the contribution to G at each radial position.

C.1 Integral for apparent temperature

In general, a small change in conductance is related to a small change in resistance by the relation

$$\Delta G = \frac{1}{R + \Delta R} - \frac{1}{R} \sim \frac{-\Delta R}{R^2}. \tag{C.2}$$

Using this approximation, we can rewrite equation C.1 in terms of resistance as

$$\Delta T_{apparent} = \left(\frac{dR}{dT}\right)^{-1} \Delta R. \tag{C.3}$$

Substituting in the integral of resistivity for ΔR (similar to Equation 5.4), and relating it to $\Delta T(r)$, we obtain

$$\Delta T_{apparent} = \left(\frac{dR}{dT}\right)^{-1} \int_{r_1}^{r_2} \frac{\partial \rho}{\partial T} \frac{\Delta T(r)}{2\pi r} dr. \tag{C.4}$$

Applying the usual relation between ρ and R (Equation 5.4), we find

$$\Delta T_{apparent} = \frac{1}{\log(r_2/r_1)} \int_{r_1}^{r_2} \frac{\Delta T(r)}{r} dr. \tag{C.5}$$

In other words, $T_{apparent}$ is given by a weighted average of $\Delta T(r)$ where the weights are simply proportional to $1/r$.

C.2 Diffusion case

Inserting the temperature profile for diffusion into equation C.5, we obtain

$$\Delta T_{apparent} = \frac{P}{4\pi\kappa_{wf} \log^2(r_2/r_1)} \int_{r_1}^{r_2} \frac{\log(r/r_1)\log(r_2/r)}{r} dr, \tag{C.6}$$

which can be solved analytically. The result, after rearranging and rewriting in terms of κ_{wf}, is given by

$$K_{apparent} \equiv \frac{P}{\Delta T_{apparent}} = 12\kappa_{wf}, \tag{C.7}$$

which is independent of r_2 and r_1.

C.3 Phonon emission case

In the case of cooling by phonon emission, the relevant integral is

$$\Delta T_{apparent} = \frac{P}{2\pi\kappa_{e-ph} \log^2(r_2/r_1)} \int_{r_1}^{r_2} \frac{dr}{r^3}, \tag{C.8}$$

and, with $K \equiv \kappa_{e-ph} \times A$, we obtain

$$K_{apparent} = \left(\frac{2 r_2 r_1 \log \left(r_2 / r_1 \right)}{r_2^2 - r_1^2} \right)^2 \times K. \tag{C.9}$$

For our devices where $r_2/r_1 = 4$, we find $K = 1.83 K_{apparent}$.

Appendix D

Predicted signal for adiabatic cooling

One of the initial goals of this thesis project was to observe adiabatic cooling (described in Chapter 3), using either a secondary induction coil, or a backgate to modulate the quasiparticle density and the conductivity of the sample as a thermometer. Using the values of τ and c that we have measured at $\nu = 5/2$, we can now revisit the practicality of adiabatic cooling using a gate to induce a change in the quasiparticle density. The temperature change in adiabatic cooling is given by

$$\Delta T = -\frac{T}{C}\frac{\partial \mathcal{S}}{\partial N_q}\Delta N_q, \tag{D.1}$$

where ΔN_q is the change in the total number of quasiparticles in the sample. If we consider only the contribution of the non-Abelian entropy to $\mathcal{S}$, it implies that

$$\Delta T_{NA} = -\frac{k_b T \ln d}{C}\Delta N_q. \tag{D.2}$$

Equivalently, we can calculate the total heat absorbed due to adiabatic cooling, which is simply given by

$$Q_{NA} = -k_b T \Delta N_q \ln d. \tag{D.3}$$

The above equations assume that the 2DEG is completely thermally isolated. However, we have shown in this thesis that the 2DEG thermalizes to the phonon bath on a timescale, τ, of a few microseconds at 50 mK. Therefore, it is useful to consider the cooling power

$$\dot{Q}_{NA} = -k_b T \frac{\partial N_q}{\partial t}\ln d, \tag{D.4}$$

where $\frac{\partial N_q}{\partial t}$ is the rate of change of quasiparticle number in the sample. The maximum temperature change achievable by continuously adding quasiparticles at a constant rate is then given by

$$\Delta T_{max} = -\frac{k_b T \tau \ln d}{C} \frac{\partial N_q}{\partial t}. \tag{D.5}$$

However, the process of adding quasiparticles also dissipates heat into the 2DEG. As an estimate, we can use the Joule heating power, given by

$$P = R \left(q \frac{\partial N_q}{\partial t} \right)^2, \tag{D.6}$$

where R is the resistance of the device and q is the quasiparticle charge. The temperature change and cooling/heating power due to both the adiabatic cooling and Joule heating effects of adding quasiparticles are calculated and plotted in Figure D.1, for parameters based on the CB05 Corbino device and the data presented in Chapter 7. The non-Abelian contribution to adiabatic cooling only outcompetes Joule heating for a very slow rate of adding quasiparticles of less than 150 quasiparticles per microsecond into the entire $3\,\mathrm{mm}^2$ device. The resulting cooling power is only a fraction of a femtowatt, and due to the heat leak to the phonons results in a temperature change of less than a microkelvin. This is well below the threshold of detectability via the conductance thermometry techniques discussed in this thesis (at $T = 50$ mK).

The adiabatic cooling signal may be enhanced by choosing a device with a ratio r_2/r_1 closer to 1, thus reducing R and therefore the Joule heating power. One would also expect the experiment to become more viable at lower temperature, since c is expected to decrease, which would result in a larger ΔT for the same $\dot{Q}$. At the same time, τ increases, providing better better thermalization and the opportunity to do the experiment more slowly. However, ΔT_{max} and P are proportional to T in equations D.4 and D.5, and R diverges in a well-developed QH state, which means more power is required to move quasiparticles in or out of the 2DEG. The specific interplay between these various factors would determine whether there is any temperature range where the adiabatic cooling experiment could lead to an observable signal.

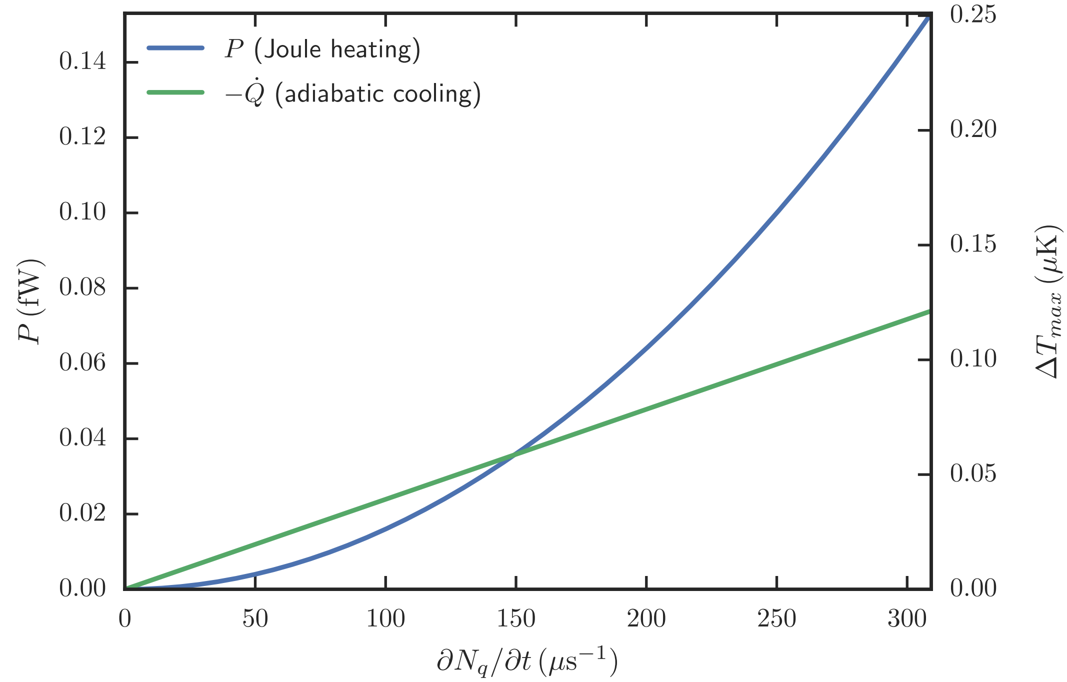

Figure D.1: Estimated magnitude of the non-Abelian contribution to adiabatic cooling effect as a function of the rate at which quasiparticles are added to the sample. The blue curve is an estimate of the heat generated by adding the quasiparticles, while the green line is the non-Abelian contribution to adiabatic cooling. Both curves can be read as power using the lefthand axis, or temperature change using the righthand axis. Parameters used in the calculation are: $R = 1\,\mathrm{M}\Omega$, $\tau = 2\,\mu$s, $T = 50\,$mK, $n_e = 3 \times 10^{11}\,\mathrm{cm}^{-2}$, $A = 0.03\,\mathrm{cm}^2$ and $C = 0.01 k_b N_e$.

Appendix E

Rectification and thermopower

E.1 Introduction

In general, a nonlinear effect that results in an I-V curve that is not antisymmetric around zero (or equivalently dI/dV not symmetric about zero) is known as *rectification* and will result in a DC voltage appearing when an AC voltage is applied to the sample. In this chapter, we will discuss a series of non-linear effects which appear qualitatively similar to one another - they all manifest as rectification with a sign that follows $d\sigma_{xx}/d\nu$ as the filling factor changes. The first such phenomenon is self-gating in a Hall bar, for which we present experimental results that are in excellent agreement with a simple theoretical calculation. The second phenomenon we discuss is rectification due to the self magnetic field of a Corbino device, but our calculation shows that the effect is too tiny to observe. The rectification signal we actually observe in a Corbino device is orders of magnitude larger than expected. We next turn to a third mechanism: thermopower due to non-uniform self-heating of the 2DEG. Although this, or some closely related phenomenon, may explain the observed rectification in the Corbino device, further experiments and analysis are required to understand the data. Finally, we show similar oscillations in the charge on a gate near a 2DEG exposed to a modulated high frequency RF field, which may be a measurement of $\partial\mu/\partial T$, but the unexpectedly large signal magnitude requires further investigation.

E.2 Self-gating

E.2.1 Theory

The electron density in a 2DEG can be changed by applying a voltage difference between it and a nearby gate. Typically, this is accomplished by grounding the 2DEG and using a voltage source to bias the gate. However, if the gate is grounded, a voltage applied on the 2DEG changes the density in the same way. Since the sample and lead wiring have finite resistance, by Ohm's Law a current, i, passing through the sample will result in a voltage, V_{gs} between the gate and 2DEG. This will lead to an effect that has been referred to as "self-gating" in quantum dots [98] and carbon nanotubes [99], and is related to the concept of channel length modulation in electrical engineering. Here, we show how it manifests specifically in a gated Hall bar in a magnetic field. We consider the 2DEG and gate as two plates of a parallel plate capacitor with capacitance C, area A and electron density n_0. A cartoon of the basic arrangement is shown in Figure E.1.

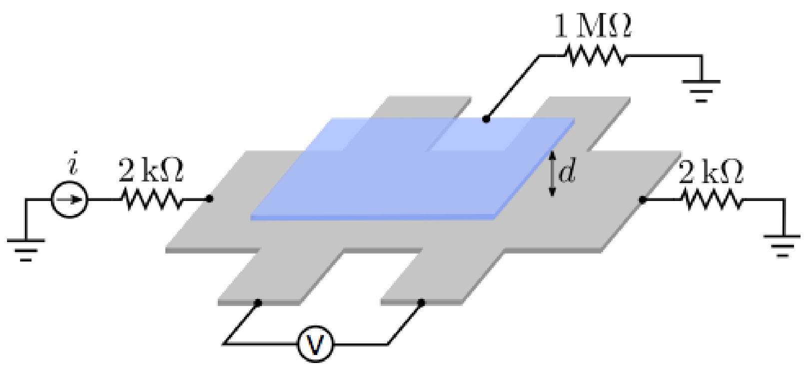

Figure E.1: Cartoon of a gated Hall bar, showing the arrangement in which self-gating may be observed.

The change in electronic density in the 2DEG, Δn, and the voltage between gate and 2DEG, V_{gs}, are then related by the equation $\Delta n = CV_{gs}/eA$. We estimate the average voltage on the sample to be $V_{gs} \simeq \frac{1}{2}R_{2pt}i$, with R_{2pt} being the total two point resistance (including leads). If i is an AC current given by $i_0 \sin \omega t$, the magnitude of the density modulation is

$$\Delta n = \frac{CR_{2pt}}{2eA} i_0 \tag{E.1}$$

and the voltage response is, to first order,

$$V_{xx} = i_0 \sin(\omega t) \left(R_{xx}(n_0) + \frac{\partial R_{xx}}{\partial n} \frac{C R_{2pt}}{2eA} i_0 \sin(\omega t) \right). \quad \text{(E.2)}$$

Multiplication of the two sinusoidal terms leads to the expression

$$V_{xx} = i_0 R(n_0) \sin(\omega t) + \frac{1}{4} i_0 \frac{\partial R_{xx}}{\partial n} \frac{C}{eA} R_{2pt} (1 - \cos(2\omega t)), \quad \text{(E.3)}$$

where the second term represents rectification, which could be observed at DC or the second harmonic. In the quantum Hall regime, R_{xx} is a function of filling factor, $\nu = nh/eB$, where B is the magnetic field. Therefore, the partial derivatives of R_{xx} are related by

$$\frac{\partial R_{xx}}{\partial n} = -\frac{B}{n} \frac{\partial R_{xx}}{\partial B}, \quad \text{(E.4)}$$

and we can write the DC and second harmonic signals as

$$V_{DC,2\omega} = \frac{B C R_{2pt}}{4nA} \frac{\partial R_{xx}}{\partial B} i_0^2, \quad \text{(E.5)}$$

where the 2ω signal is in phase with $-\cos(2\omega t)$. Thus, the expected signature of self-gating is a DC or second harmonic signal that oscillates with B, following the derivative of R_{xx}.

E.2.2 Results and discussion

A demonstration of self-gating behaviour is shown in Figure E.2. The sample is a Hall bar with gate-2DEG overlap area $A = 0.62\,\mathrm{mm}^2$ (determined from photographs of the device), $n_0 = 2.9 \times 10^{11}\,\mathrm{cm}^{-2}$, mobility $1.1 \times 10^6\,\mathrm{cm}^2/\mathrm{V}\cdot\mathrm{s}$ and depth $d = 100\,\mathrm{nm}$. The experiment was performed in a dilution refrigerator at base temperature of 18 mK. Figure E.2a shows R_{xx} measured with a 200 nA sinusoidal excitation current at 6.5 Hz. Well-formed SdH oscillations and even IQHE minima are clearly visible. At the same time, i_{gate} (the current between the gate and ground) was measured using a current preamplifier, as shown in Figure E.2b. Since the 2DEG and gate form the two plates of a capacitor, i_{gate} is equal to the current entering and leaving the 2DEG, so we can directly calculate from it $\Delta N = \frac{i}{\omega}$. The ∼25 pA current at 0 T is primarily due to the 2 kΩ resistors included in the circuit as part of RC filters, while the upward slope is due to the contribution of the Hall

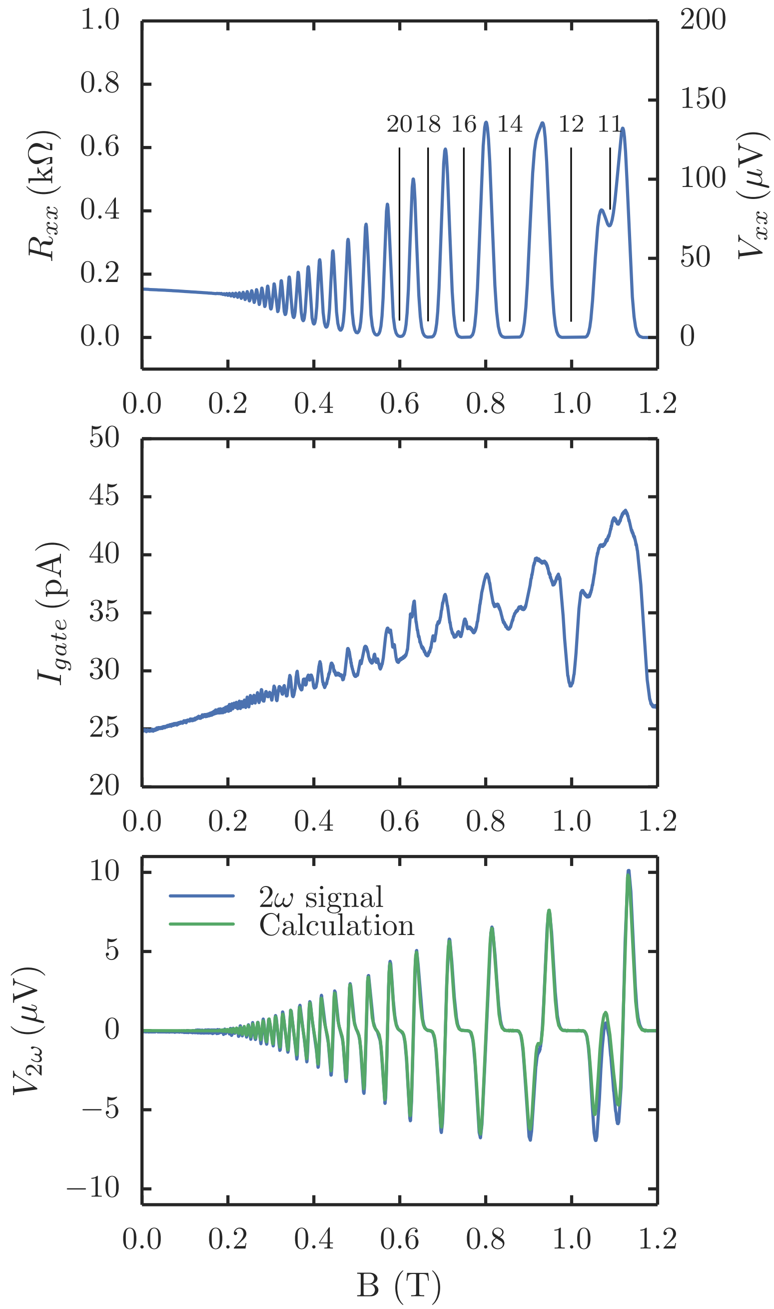

Figure E.2: Self-gating phenomenon in a gated Hall bar. a) R_{xx} measured with a 200 nA current. b) Current measured between the gate and ground, indicating that the 200 nA bias on the 2DEG is large enough to change the electronic density in the 2DEG. c) Second harmonic signal (blue) and model (green). The model is calculated from the data in panels (a) and (b) as described in the text.

effect to R_{2pt}. Oscillations are due to R_{xx}, as well as the timescale to move charge into the bulk of the 2DEG, given by $\tau \simeq C/\sigma_{xx}$, which diverges in well-formed IQHE minima such as $\nu = 12$. Since we have the measurement of i_{gate}, we can use the equation

$$V_{DC,2\omega} = \frac{Bi_{gate}}{2nAe\omega}\frac{\partial R_{xx}}{\partial B}i_0 \tag{E.6}$$

instead of equation E.5 to calculate the expected rectification signal. As shown in Figure E.2c, this calculation closely follows the actual measurement of $V_{2\omega}$. Due to the large capacitance (thanks to the small separation between the 2DEG and gate) and sharp features in the magnetoresistance of high mobility samples, self-gating effects are strong even for a moderate excitation of 200 nA.

It should be noted that self-gating modifies the current flow on the basis of V_{gs}, rather than the physical direction of i within the device. Its directionality as a rectifier is set by choosing which terminal is grounded (or set to the same potential as the gate). This is quite different from many other rectifiers, such as diodes, which rely on physical properties of the device itself to choose an easy and hard direction.

Although self-gating does not itself give access to any particularly deep physics, it is experimentally relevant in that it interferes with other non-linear effects that one might attempt to study. Any non-linear transport experiment where the sample is proximate to a grounded conductor must take self-gating into account as a potential confounding effect.

E.3 Self-magnetic field in a Corbino disk

A variation of self-gating is possible in the Corbino geometry, and was first predicted by Kleinman and Schawlow in 1960 [51] for high-mobility 3D materials and observed experimentally in bulk InSb by Green in 1961 [100]. As shown in Figure E.3a, current flows in a spiral path in a Corbino device subjected to a magnetic field B and the tangential component of the current in turn creates a small additional magnetic field ΔB. Thus, much like self-gating, a strong current slightly changes the filling factor in the 2DEG. The radial voltage response v_r, to a drive current i_r is

$$v_r = iR = (i_r \sin(\omega t))(R_0 + \frac{\partial R}{\partial B}\Delta B \sin(\omega t)) \tag{E.7}$$

where $\Delta B \sin(\omega t)$ is the magnetic field caused by the tangential component of the current and R is the resistance between the two contacts.

For a simple order-of-magnitude estimate of the rectified signal, we assume

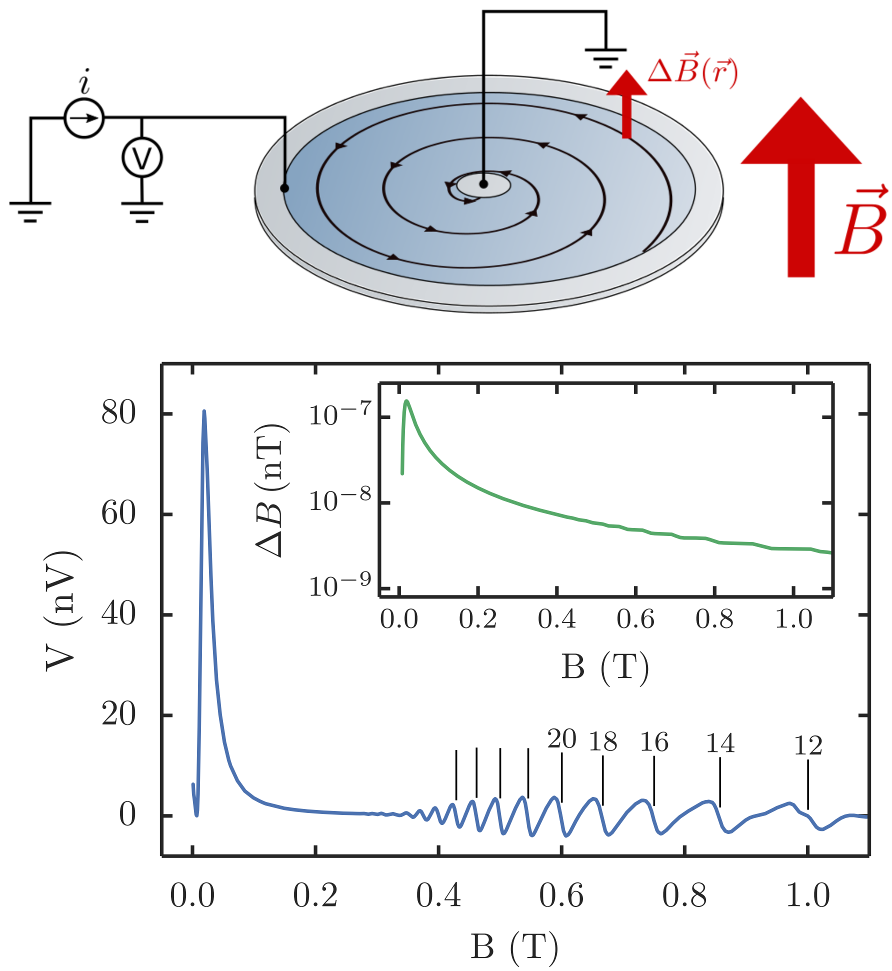

Figure E.3: (a) Cartoon of filling factor modulation due to current in the Corbino geometry. In a magnetic field, B, a voltage applied between the two contacts drives a current in a spiral path. The tangential component of the current creates a field $\Delta B(r)$, which in turn affect ν and σ. (b) Estimated rectified voltage signal due to the self-magnetic field for $v_0 = 10\,\text{mV}$ and $r_2 = 1\,\text{mm}$, calculated from R_{xx} and R_{xy} data according to equation E.8. The estimated ΔB is shown in the inset.

that all of the tangential current flows at the outer rim of the Corbino, and is given by $i_\phi = \sigma_{xy} v_r$. We also assume that the entire device experiences the field which that current would generate at the center of the device, given by $\Delta B = \frac{\mu_0 i_\phi}{2 r_2}$. This simple model, although it is a coarse approximation, provides an upper bound on the possible rectification effect. The rectified part of Equation E.7 can be written for an excitation $v_0 \sin(\omega t)$ as

$$V_{DC,2\omega} = \frac{\mu_0 \sigma_{xy} v_0^2}{2 r_2 \sigma_{xx}} \frac{\partial \sigma_{xx}}{\partial B}, \tag{E.8}$$

where μ_0 is the magnetic constant, and r_2 is the outer radius of the Corbino disk. Using R_{xx} and R_{xy} measured in the Hall bar device shown in Figure E.2a, we have calculated σ_{xx} and σ_{xy} for a hypothetical Corbino sample. In Figure E.3b, equation E.8 is plotted for some reasonable experimental parameters ($r_2 = 1$ mm, $v_0 = 10$ mV), with the estimated magnetic field ΔB in the inset. Other than the peak near 0 T, the expected signal is less than ~5 nV, which is 10^6 times smaller than v_0. While such a small signal may be detectable, it is far smaller than the rectification signal actually observed in our sample, as will be discussed in the results part of the next section.

E.4 Thermopower in the Corbino geometry

Thermopower can be understood as rectification if we consider the (electrical) heater and the sample together as a single device. A typical thermopower experiment may be considered as a four terminal measurement, as shown in Figure E.4. A local heater, driven by I+ and I- leads, creates a temperature differential, ΔT, across the sample. The resulting thermovoltage, V_{tp} is then measured using V+ and V- contacts. Since the direction of the heater current does not affect the orientation of ΔT, the polarity of V_{tp} is also independent of the current direction. The I-V curve where I is the heater current and V is V_{tp} is completely symmetric. Thus, thermopower may be classified as a four terminal rectification effect, and indeed it is common to drive the heater at a frequency ω and detect V_{tp} at 2ω [40, 43, 101, 102].

In the two-terminal Corbino geometry, Joule heating leads to a radial thermal gradient due to the higher current density near the center of the device. In fact, the heating power per unit area varies as $1/r^2$, which can lead to a substantial thermal gradient if the contacts are not able to efficiently remove heat from the 2DEG. Since the heating power is independent of current direction, and the direction of the thermal gradient is set by the physical geometry of the sample, the resulting thermovoltage has the same sign regardless of the current direction. Therefore, thermopower could potentially lead to a rectification signal in Corbino samples.

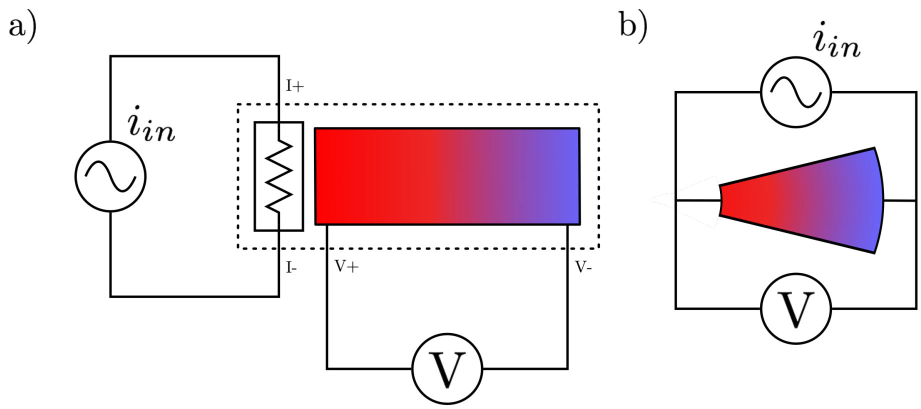

Figure E.4: Thermopower as rectification in four terminal and two terminal configurations. a) Four terminal configuration, where an AC input current to a heater results in a thermal gradient and DC voltage along the sample. b) A two terminal measurement of an assymetrical sample (a slice of a Corbino disk, in this case), where the gradient in current density creates a thermal gradient and results in a DC thermovoltage.

E.4.1 Mott formula for thermopower in the Corbino geometry

In the presence of both an electric field and a thermal gradient, the diffusion current in a conductor is given by

$$j = \hat{\sigma} E + \hat{\lambda} \nabla T, \tag{E.9}$$

where $\hat{\sigma}$ is the electrical conductivity tensor and $\hat{\lambda}$ is the thermoelectric conductivity tensor. Since we are interested in the thermopower with no current flowing, we set $j = 0$ and use the symmetry of our particular geometry to simplify the equation. In the Corbino case, there are no steady state tangential electric fields ($\vec{E} = [E, 0]$) and the thermal gradient we impose is purely radial ($\nabla_\theta T = 0$). Therefore, we have

$$S_{rr} = \frac{E}{\nabla_r T} = \frac{\lambda_{rr}}{\sigma_{rr}}. \tag{E.10}$$

Using the Chester-Thellung-Kubo-Greenwood formalism [103,104], we can write down both $\hat{\sigma}$ and $\hat{\lambda}$ as integrals over energy as follows:

$$\hat{\sigma} = -\int_0^\infty \left(\frac{\partial f}{\partial \epsilon}\right) \hat{\sigma}_0 d\epsilon \tag{E.11}$$

and

$$\hat{\lambda} = -\frac{1}{eT}\int_0^\infty \left(\frac{\partial f}{\partial \epsilon}\right)(\epsilon - \mu)\,\hat{\sigma_0} d\epsilon \tag{E.12}$$

and therefore

$$S_{rr} = \frac{\int_0^\infty \left(\frac{\partial f}{\partial \epsilon}\right)(\epsilon - \mu)\,\sigma_0 d\epsilon}{eT\int_0^\infty \left(\frac{\partial f}{\partial \epsilon}\right)\sigma_0 d\epsilon} \tag{E.13}$$

where we define $\sigma_0 = \sigma_{rr}(T = 0)$ for notational convenience. In the low temperature limit, we can apply a Sommerfeld expansion to equation E.13 to obtain

$$S_{rr} = -\frac{\pi^2 k_B^2}{3e\sigma_0}\left(\frac{d\sigma_0}{d\epsilon}\right)_{\epsilon=\epsilon_f}. \tag{E.14}$$

In order to directly calculate S_{rr} from conductance data, we use the relations between ν, ϵ, n_e and B to write this as

$$S_{rr} = -\frac{L_0 eB}{\epsilon_f \sigma_0}\frac{d\sigma_0}{dB} \tag{E.15}$$

where $L_0 = \pi^2 k_b^2/3e^2$ is the Lorenz number. For a Corbino device being self-heated by a voltage bias v_0, we would therefore expect a signal like

$$V_{tp} = S_{rr}\Delta T = -\frac{L_0 eB}{\epsilon_f \sigma_0}\frac{d\sigma_0}{dB}\Delta T \tag{E.16}$$

with

$$\Delta T(v_0, B) = \gamma(B) v_0^2, \tag{E.17}$$

where $\gamma(B)$ is some function such that $\Delta T(v_0, B) = \gamma(B)v_0^2$. To determine $\gamma(B)$, one would need a detailed model of heat flow in the device, especially near the ohmic contacts to the 2DEG.

E.4.2 Experimental design

Figure E.5 shows the measurement scheme for the basic Corbino rectification measurement. A high frequency AC voltage is capacitively coupled to the sample, which is then measured by a DC coupled preamplifier. This unusual setup allows us to both apply a voltage bias and measure the open-circuit voltage (at different frequencies), unlike the more conventional circuits discussed in Chapter 4 that apply voltage and measure current and vice versa. This configuration is ideal for measuring thermopower, where we are interested in measuring the open circuit voltage, but

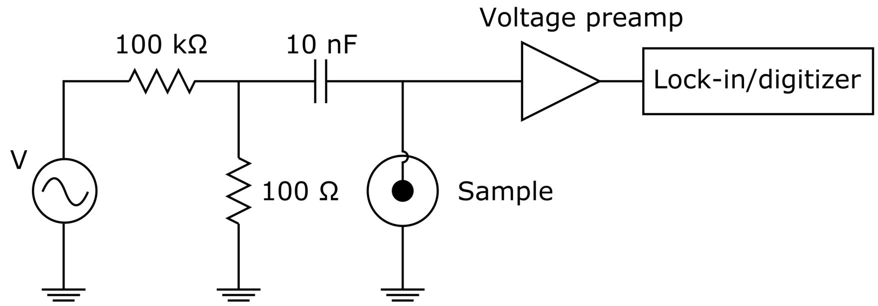

Figure E.5: Simplified schematic diagram for a rectification measurement in the Corbino geometry.

applying a constant current to the Corbino is impractical due to its extremely high resistance in quantum Hall states.

In order to improve the signal-to-noise-ratio and avoid DC drift, the AC voltage is also modulated at 6.5 Hz, and the lock-in amplifier detects at the modulating frequency rather than DC. However, the basic result does hold for continuous-wave AC excitation (or even excitation by white noise) and purely DC detection. The conductance of the sample could also be measured simultaneously by adding another AC voltage at a different frequency and measuring the current between the sample and ground using a second lock-in amplifier.

E.4.3 Results with DC detection

In the most basic rectification measurement, we measured the DC response to an AC excitation. In this case, an AC voltage of 0.5 mV at 200 kHz is applied across the sample. A preamplifier with a low pass filter (0.3 Hz, 12 dB) and gain of 1000 is also connected to measure the voltage across the sample. The output of the preamplifier is then connected to a DC voltmeter. The result of this measurement is plotted as the blue line in Figure E.6. For comparison, we also plot the conductance, measured on a separate field sweep using a conventional lock-in technique.

As the magnetic field increases, σ decreases and begins to oscillate, as is typical for the SdH and IQH regime. Meanwhile, V_{DC} oscillates, rapidly switching from negative to positive as the field passes through each minimum of σ. These sawtooth-like oscillations grow in amplitude with increasing magnetic field. Interestingly, a substantial portion of the DC response is present even with no applied voltage, as shown in Figure E.7. This suggests that, at least in this measurement configuration,

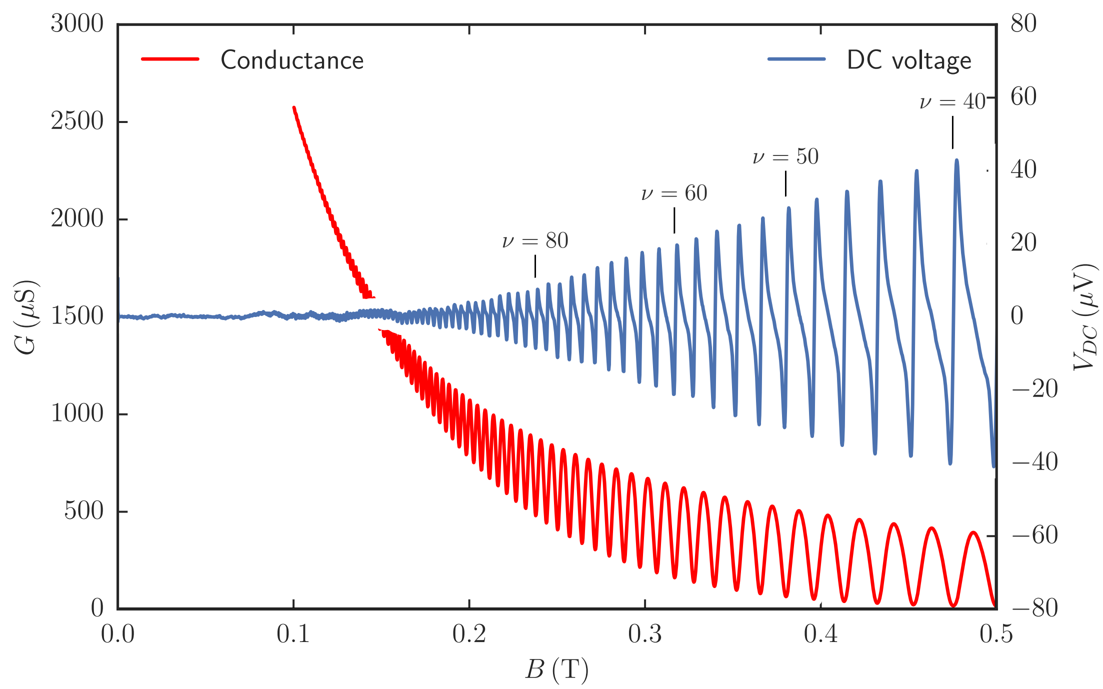

Figure E.6: Rectification signal in the Corbino geometry. A constant offset of 19 μV has been subtracted from V_{DC}, such that V_{DC} is zero at $B = 0$ T.

a substantial stray voltage (nearly equivalent to 500 μV at a single frequency) is coupled to the sample. This is probably due to the length of the wires, and the absence of a room temperature resistor in the circuit to shunt pickup voltages to ground.

E.4.4 Possible explanations in terms of filling factor shifts

Self-gating

The behaviour of V_{DC} in Figure E.6 looks strikingly similar to rectification due to self-gating, discussed earlier in this chapter. Although sample CB01 is not intentionally gated, a nearby ground plane could nonetheless act as a gate and cause rectification. We can calculate the approximate capacitance between the 2DEG and the ground plane and see if it is consistent with any known features in the sample. The equivalent of Equation 1.5 for constant voltage V_{in} (rather than constant

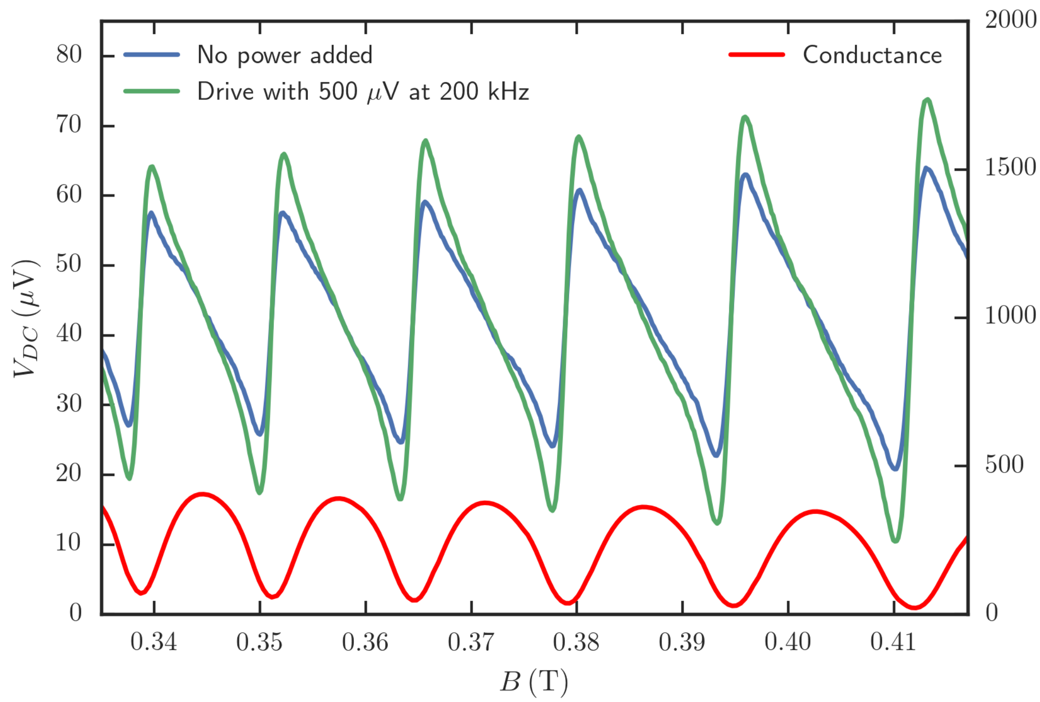

Figure E.7: DC voltage across the Corbino device both with and without an applied AC voltage. Here, the offset has not been subtracted, but is arbitrary (it can be adjusted using a screw on the preamplifier).

current) in a Corbino device is

$$V_{DC} = -\frac{CV_{in}^2 B}{2eAnR}\frac{\partial R}{\partial B}. \tag{E.18}$$

The value of C required to make this calculation overlap with the data over the range from 0.4 to 0.5 T is roughly 1.5 nF, as shown in Figure E.8a. The capacitance would also have to be field dependent, monotonically increasing with increasing magnetic field, in order to fully capture the behaviour of the data. From this calculation, it appears that the rectification is roughly consistent with self-gating between the 2DEG and the surface of the sample. However, this would require the presence of a conducting layer at the surface with fairly high mobility that is connected to only one of the contacts. Since the drive frequency was 200 kHz, we can conclude that resistance of the surface layer would have to be less than 500 Ω in order for the RC time constant to be sufficiently short enough. It seems unlikely that such a conductive layer could "accidentally" be connected to only one contact and completely disconnected from the other, which would be necessary since parallel conduction between the contacts is seen in this device. One possibility is metallic contamination on the top surface of the sample, perhaps due to excess indium solder extending beyond the central contact area [1]. However, it would not explain the field dependence; the dielectric constant for GaAs does not vary strongly with magnetic field. This explanation could be checked by repeating the experiment with multiple samples to check for consistency and any dependence on 2DEG depth and design. Qualitatively similar results were observed in two other samples, but systematic experiments have not yet been performed.

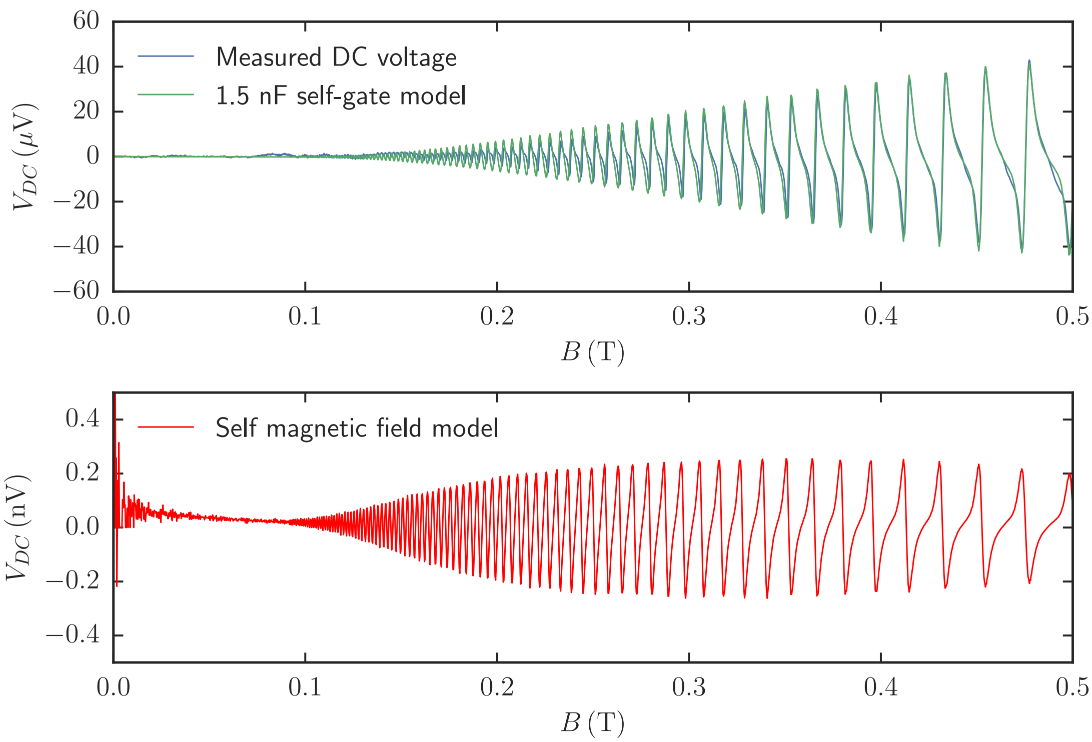

Figure E.8: (A) Experimental V_{DC} (blue) and calculated self-gating effect assuming a 1.5 nF capacitance to ground. (B) Modelled rectification due to self magnetic field. Note the difference in scale - the prediction is five orders of magnitude smaller than the data in panel A.

Self-magnetic field

As discussed in section E.3, the current in a Corbino device travels in a spiral path, and its tangential component generates a small magnetic field that could

[1] Note that the bottom surface of the sample is about 0.7 mm away from the 2DEG, yielding a capacitance of just 0.5 pF

change the conductance of the sample by slightly shifting ν. The result of this calculation based on equation E.8 using the conductance data from CB01 is shown in Figure E.8b. The effect is far too small to account for the observed magnitude of V_{DC}. Additionally, the model fails to capture the shape of the envelope of the rectification data, as well as having the opposite sign.

E.4.5 Modeling as thermopower

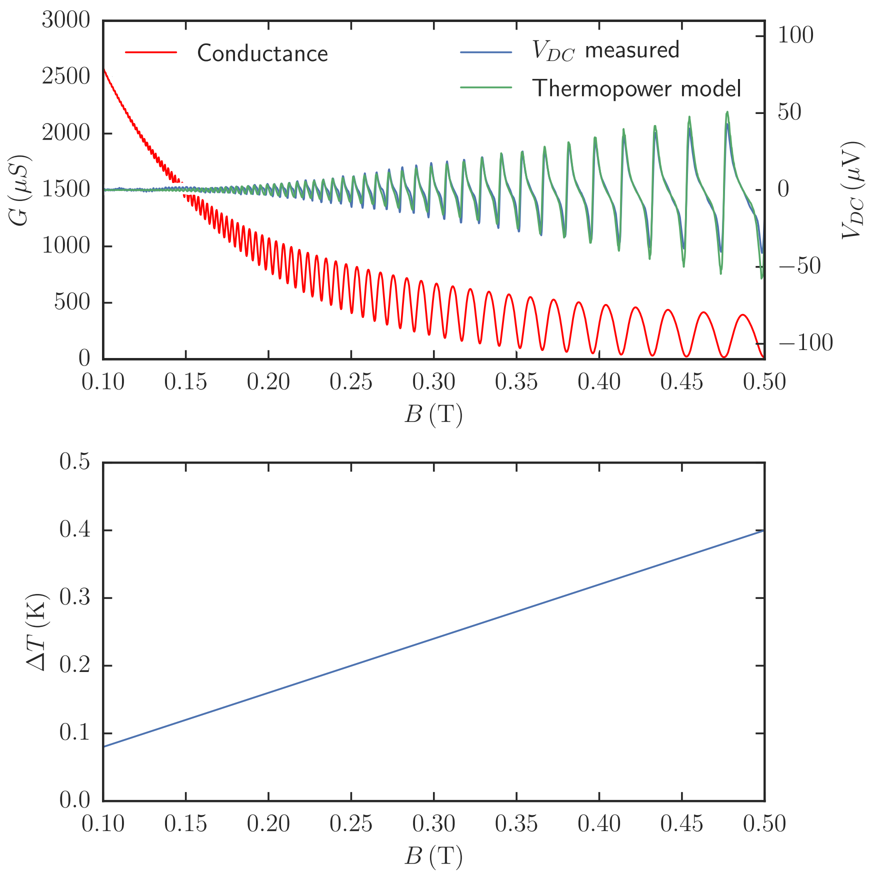

Figure E.9: Experimental rectification data (blue) overlaid with calculated thermovoltage assuming $\Delta T = 0.8 \times B\,[\mathrm{K/T}]$. b) Assumed ΔT dependence for panel a.

In order to better understand whether V_{DC} is a thermovoltage due to self-heating, we consider the possibility that ΔT is field-dependent. In Figure E.9a, V_{DC} is plotted again, along with the thermovoltage calculated according to Equation E.16 with $\Delta T = 0.8 \times B\,[\mathrm{K/T}]$ as shown in panel b. The form of $\Delta T(B)$ was chosen to capture the observed envelope shape across a wide range of magnetic field, and is not based on any physical model. It would suggest that the self-heating of the 2DEG is substantial, with $\Delta T > T_0$. The increase of ΔT with increasing magnetic field would imply that the 2DEG is less able to thermalize as the field increases, which is consistent with the increasing magnetoresistance of the 2DEG (and, perhaps, contacts) with increasing magnetic field.

E.5 Measuring entropy via $\frac{\partial \mu}{\partial T}$

E.5.1 Experimental Design

As another approach to measuring the entropy of the 2DEG, we tested a variation of a scheme proposed by Cooper and Stern [38] and previously carried out experimentally at high temperature (at and above 2.4 K) by Kuntsevich *et. al.* [44], and more recently using a quantum dot charge sensor by Hartman *et. al.* [105] . The basic concept, as discussed in Chapter 3 of this thesis, is to measure the change in chemical potential of the 2DEG as temperature changes, and then use the Maxwell relation

$$\left(\frac{\partial \mu}{\partial T}\right)_N = -\left(\frac{\partial S}{\partial N}\right)_T \tag{E.19}$$

to obtain the entropy. A sketch of our version of the experiment is shown in Figure E.10. The sample, the same gated Hall bar used in the self-gating experiment described in section E.2, is placed inside a small external RF coil, which is perpendicular to the magnetic field. This coil arrangement is similar to the setup used for resistively detected nuclear magnetic resonance experiments (RDNMR), but rather than tuning to a specific resonance frequency we use some other arbitrary frequency ($f_{RF} = 100$ MHz) to induce non-resonant heating. The RF field is modulated at a much lower frequency $f_{mod} = 500$ Hz, with the result that the electron temperature includes a time-varying component of the form $\Delta T \sin(\omega_{mod} t)$ [2].

As the temperature of the 2DEG changes by an amount ΔT, so too does its chemical potential by an amount $\Delta \mu = \Delta T \frac{\partial \mu}{\partial T}$. Because the 2DEG and its top gate form a parallel plate capacitor as shown in Figure E.10, $\Delta \mu$ can be inferred by measuring the electrical current flowing in and out of the top gate. The gate current

[2] The actual modulation used here is such that the drive voltage is given by $v = \frac{1}{2}(1 + \sin(\omega_{mod} t)) \times \sin(\omega_{RF} t)$. Since the heating is proportional to power, not voltage, there will be additional higher order terms, which we neglect since the measurement is performed with a lock-in tuned to ω_{mod}.

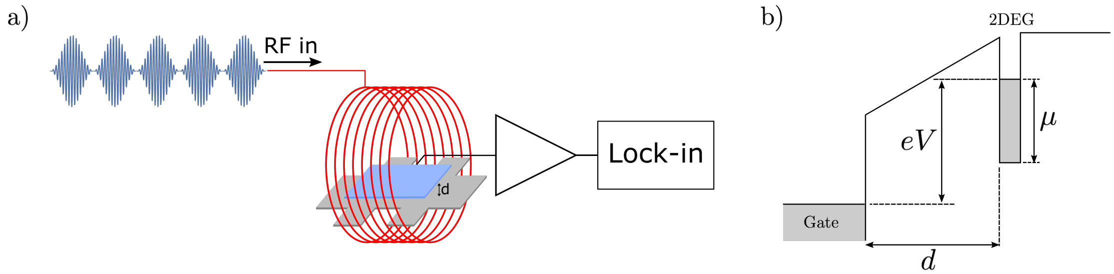

Figure E.10: a) Experimental setup to heat the sample via non-resonant heating and detect the resulting gate current. b) Simplified band diagram showing the capacitor formed by the gate and 2DEG.

i_{gate} is given by

$$i_{gate} = \frac{1}{\omega_{mod} C} \frac{\partial \mu}{\partial T} \Delta T \cos(\omega_{mod} t). \tag{E.20}$$

In the experimental arrangement reported here, we do not strictly maintain a constant number of electrons in the sample. As proposed by Cooper and Stern [38], one could instead measure the current between the sample and ground, and use a feedback loop to apply a voltage to the sample to null that current. The required feedback voltage would then be precisely equal to μ with $\Delta N = 0$.

E.5.2 Results and Discussion

The experiment was tested in the SdH and IQHE regime with the coil driven at -25 dBm. Simultaneously, a 10 nA AC current at 17 Hz was used to perform a standard R_{xx} and R_{xy} measurement. The resulting measurements of R_{xx} and R_{xy} are shown in Figure E.11a, while i_{gate} is shown in Figure E.11b (on the lefthand axis). The righthand axis shows $\Delta\mu$ calculated using $C = 0.7$ nF, as determined from the self-gating dataset (which also agrees with the known geometry of the sample). The shape of the signal is quite different from the shape of dR_{xx}/dB and the self-gating signal discussed earlier in this chapter, suggesting that this is not a variation of the same phenomenon. Instead, the qualitative behaviour of i_{gate} is roughly as expected for $\partial s/\partial n$: a slightly saw toothed oscillation with zero crossings at the minimum and maximum of R_{xx}, appearing primarily in the out-of-phase (imaginary) part of the signal. For comparison to a simple model, Figure E.12 shows $\mathcal{S}$ and $\partial\mathcal{S}/\partial N$ at T $= 100$ mK for $n = 2.9 \times 10^{11}$ cm^{-2} using the low-temperature approximation

$$\mathcal{S} = \frac{\pi^2 T g(\epsilon_F)}{3} \tag{E.21}$$

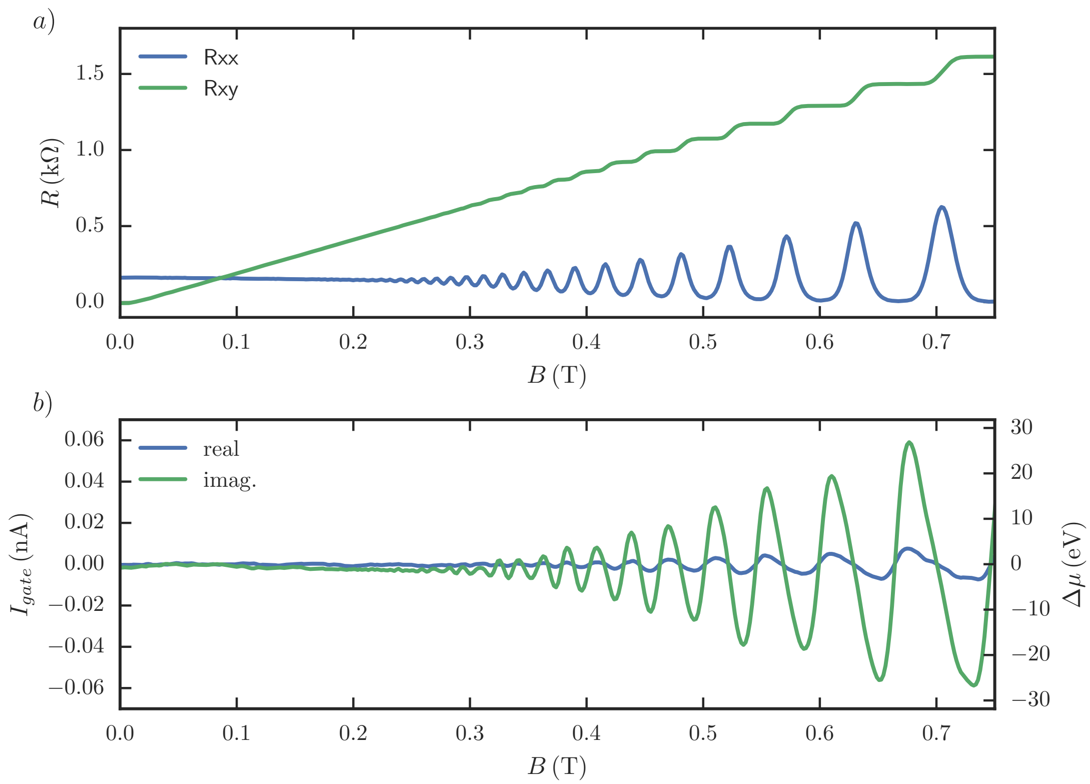

Figure E.11: Measurement of i_{gate} due to non-resonant RF heating of the 2DEG, measured in a Hall bar configuration. a) R_{xx} and R_{xy} measured using a 10 nA excitation and standard lock-in technique at 17 Hz. b) Current between the gate and ground measured at ω_{mod}=500 Hz. The mixing chamber temperature was 70 mK during the experiment.

and Gaussian-broadened Landau levels with $\Gamma = 1$ K (FWHM = 1.6 K). The qualitative differences in the shape of i_{gate} and the calculation of $\partial\mathcal{S}/\partial N$ could be explained by differences in the broadening function, if the Gaussian model is not a good approximation of the real LL shape in this sample. However, the experimental data is also more than an order of magnitude larger than expected. The unexpectedly large signal size could only be explained if both T and ΔT are close to 0.5 K, implying that the RF heating of the 2DEG was much stronger than anticipated based on previous studies that used similar RF power levels and the same apparatus (albeit at a much lower frequency, around 50 MHz, and in an ungated sample with much higher mobility) [8]. Further investigation is required to determine whether that explanation holds, or whether there is some origin for this striking result.

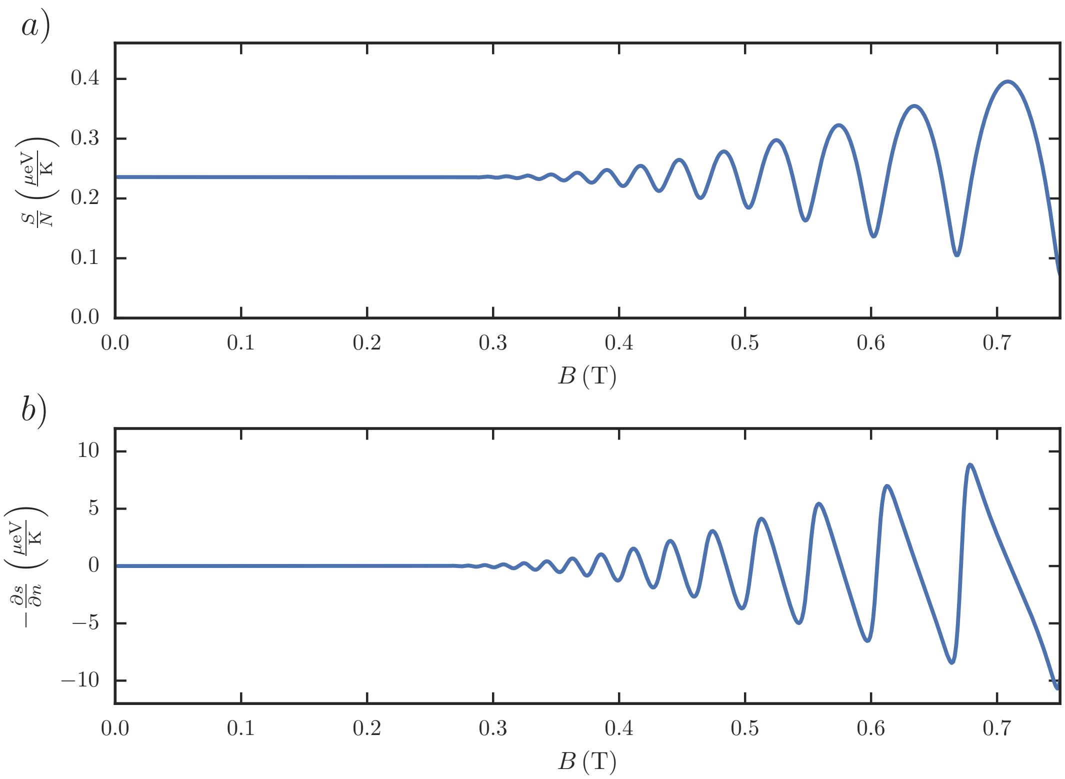

Figure E.12: Numerical calculations of entropy for Gaussian-broadened LLs with $n_e = 2.9 \times 10^{11}\,\mathrm{cm}^{-2}$, $\Gamma = 1$ K and T = 100 mK. a) Entropy per electron. b) $\partial\mathcal{S}/\partial N$ for the same parameters.

E.6 Summary

In this chapter, we discussed several different experiments and phenomena that all share a common qualitative signature. In the case of self-gating, theory and experiment are in excellent agreement. The closely related self-magnetic field effect in a Corbino device is predicted to be too small to observe experimentally. Instead, we observed a much larger rectification signal in an actual Corbino device. The signal is somewhat consistent with thermopower, but the overall field dependence and signal strength are difficult to understand. In the absence of a detailed thermal model for the 2DEG, its substrate and contacts, it is challenging to properly interpret the results or extract meaningful thermopower results. Finally we discussed another possible way to measure the entropy of the 2DEG, by using a gate as a charge sensor while varying the 2DEG temperature using non-resonant RF heating. Again, the shape of the signal is extremely promising, but the signal strength is much larger than expected. Further systematic work will be needed to disentangle the various physical phenomena that share remarkably common signatures.

Appendix F

Specific heat at high filling factors

Besides the results for τ, K and c in the SLL described in Chapter 7, I also performed measurements at higher filling factors (*i.e.* the IQH regime). These experiments were actually performed before the SLL ones, using a slightly different (and therefore less refined) technique. In this appendix, we will first calculate the integral of c over a Landau Level, and then compare it to our experimental result.

F.1 Integral of specific heat over a filling factor in magnetic field

Assume that the density of states contribution of a single spin-split Landau level can be described by the equation

$$g(\epsilon, E_c) = \frac{g_0 E_c}{2} \cdot h(\epsilon - E_N), \tag{F.1}$$

where $g_0 = m^*/\pi\hbar^2$ is the zero field density of states, $E_c = \hbar\omega_c = eB/m^*$, $E_N = \frac{1}{2}(N + 1/2)E_c$ and $h(\epsilon') = h(-\epsilon')$ is a symmetric broadening function normalized such that

$$\int_{-\infty}^{\infty} h(\epsilon')d\epsilon' = 1. \tag{F.2}$$

We now consider the integral of c, the specific heat per unit area, over a magnetic field range spanning from filling factor $\nu = N + 1$ to $\nu = N$. For simplicity, we will perform the integral over E_c. We assume the Landau levels are well-separated, and we only see contributions due to the single Landau level we are considering. Therefore, we take the integrations limits to $\pm\infty$, but only include the contribution of the Landau level centred at E_N, as follows:

$$\begin{aligned}\int_{-\infty}^{\infty} c(T,E_c)dE_c &= \int_{-\infty}^{\infty} \frac{du}{dT} dE_c \\ &= \int_{-\infty}^{\infty} dE_c \frac{d}{dT} \int_{-\infty}^{\infty} \epsilon f(\epsilon,\mu,T) g(\epsilon,\epsilon_c) d\epsilon \\ &\simeq \int_{-\infty}^{\infty} dE_c \int_{-\infty}^{\infty} d\epsilon \left(\epsilon \frac{\partial f(\epsilon)}{\partial T} \frac{g_0}{2} \cdot E_c \cdot h(\epsilon - E_N)\right).\end{aligned}$$

Next, we use the relation between E_N and E_c to eliminate E_c from the integral, and at the same time use the symmetry of h to switch ϵ and E_N, yielding

$$\int_{-\infty}^{\infty} c(T,E_c)d\epsilon_c = \frac{4g_0}{2(N+1/2)^2} \int_{-\infty}^{\infty} dE_N \int_{-\infty}^{\infty} d\epsilon \left(\epsilon \cdot \frac{\partial f(\epsilon)}{\partial T} \cdot E_N \cdot h(\epsilon - E_N)\right),$$

which can be split into two terms by substituting $E_N = (E_N - \epsilon) + \epsilon$.

$$\begin{aligned}\int_{-\infty}^{\infty} c(T,E_c)d\epsilon_c = &\frac{2g_0}{(N+1/2)^2} \int_{-\infty}^{\infty} dE_N \int_{-\infty}^{\infty} d\epsilon \left(\epsilon \cdot \frac{\partial f(\epsilon)}{\partial T} \cdot (E_N - \epsilon) \cdot h(E_N - \epsilon)\right) \\ &+ \frac{2g_0}{(N+1/2)^2} \int_{-\infty}^{\infty} dE_N \int_{-\infty}^{\infty} d\epsilon \left(\epsilon^2 \frac{\partial f(\epsilon)}{\partial T} \cdot h(E_N - \epsilon)\right).\end{aligned}$$

Each term can now be written as the integral of a convolution of two functions. The first term is

$$\begin{aligned}&\frac{2g_0}{(N+1/2)^2} \int_{-\infty}^{\infty} dE_N \left(\left(E_N \frac{\partial f(E_N)}{\partial T}\right) * (E_N h(E_N))\right)(E_N) \\ &= \frac{2g_0}{(N+1/2)^2} \left(\int_{-\infty}^{\infty} dE_N \left(E_N \frac{\partial f(E_N)}{\partial T}\right)\right) \cdot \left(\int_{-\infty}^{\infty} dE_N \left(E_N h(E_N)\right)\right) \\ &= 0,\end{aligned}$$

since $E_N h(E_N)$ is symmetric. The integral of C is then given by the second term only, which is

$$\begin{aligned}&\frac{2g_0}{(N+1/2)^2} \int_{-\infty}^{\infty} dE_N \left(\left(E_N^2 \frac{\partial f(E_N)}{\partial T}\right) * (h(E_N))\right)(E_N) \\ &= \frac{2g_0}{(N+1/2)^2} \left(\int_{-\infty}^{\infty} dE_N \left(E_N^2 \frac{\partial f(E_N)}{\partial T}\right)\right) \cdot \left(\int_{-\infty}^{\infty} dE_N h(E_N)\right) \\ &= \frac{2g_0}{(N+1/2)^2} \cdot \left(\frac{2\pi^2}{3} E_f k_b^2 T\right) \cdot 1,\end{aligned}$$

and, using the fact that $g_0 = n_e/E_f$,we have

$$\int_{-\infty}^{\infty} c(T, E_c)dE_c = \frac{n_e}{(N+1/2)^2}\frac{4\pi^2}{3}k_b^2 T.$$

Finally, making use of the definition of E_c in terms of B, we obtain

$$\int_{B_{\nu=i+1}}^{B_{\nu=i}} c(T, B)dB = \frac{4\pi^2 m^*}{3(N-1/2)^2 e\hbar}k_b T. \tag{F.3}$$

F.2 Experimental results

Specific heat measurements at high filling factors were performed using measurement setup B (as described in Section 4.4.2), with a variation of the technique described in Chapter 7. Rather than using a pure unipolar square wave to measure both K and τ, the two measurements were performed separately. First, K was found by measuring di/dv vs. V_{DC}. Then, τ was measured by continuing to apply a small voltage v_{low} to the sample after turning off the strong heating voltage v_{high}.

The results of the experiment are shown in Figure F.1. Notably, τ is relatively constant, while K varies strongly with B, roughly following the trend of G. This is expected, since, like G, K is dependent on the density of states near the Fermi energy: the amount of power that the 2DEG can dissipate is directly proportional to the number of electrons available to interact with the phonon bath. Since $\tau = C/K$, and both C and K approximately follow the density of states, it follows that τ is relatively constant.

To compare the experimental results the theoretical prediction of equation F.3, c was numerically integrated between $\nu = 11$ to $\nu = 12$, yielding a value of 4.4×10^{-4} [$\mathrm{k_b} \cdot \mathrm{T}$] per electron. The theoretical result is somewhat smaller, 3.0×10^{-4} [$\mathrm{k_b} \cdot \mathrm{T}$] per electron. The discrepancy may be due to the presence of strongly interacting bubble and stripe phases.

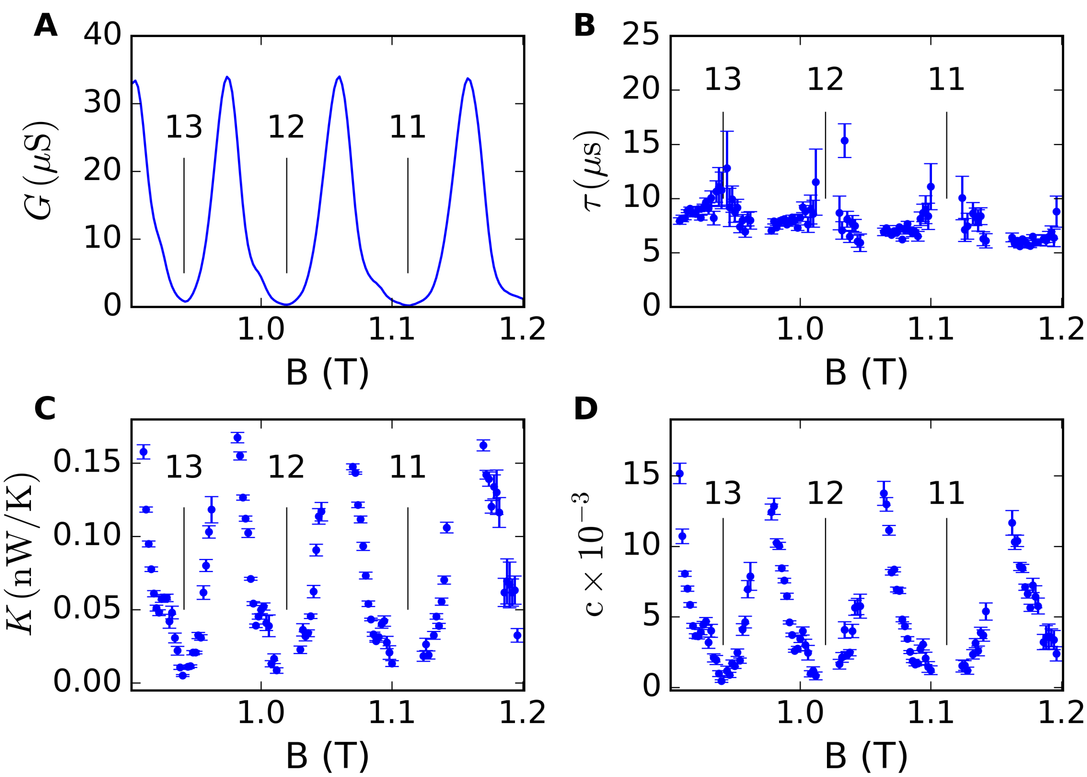

Figure F.1: Measurement of G, K, τ and c at $T_e = 60$ mK in the IQH regime. a) Conductance versus field, showing IQHE as well bubble-phase features on the left flank of each minimum (see Chapter 5). b) Thermal relaxation times, τ, which were measured during cooling (rather than during heating, as in Chapter 7). c) Thermal conductance, K, measured via di/dv. d) Specific heat c, in units of k_b per electron, calculated by multiplying τ and κ.

References

[1] R. L. Willett, C. Nayak, K. Shtengel, L. N. Pfeiffer, and K. W. West. *Physical Review Letters*, 111(18):186401, 2013.

[2] J. D. Sau, R. M. Lutchyn, S. Tewari, and S. Das Sarma. *Physical Review Letters*, 104(4):1–4, 2010.

[3] B. A. Schmidt, K. Bennaceur, S. Bilodeau, G. Gervais, L. N. Pfeiffer, and K. W. West. *Solid State Communications*, 217:1–5, 2015.

[4] B. Schmidt, K. Bennaceur, S. Gaucher, G. Gervais, L. Pfeiffer, and K. West. *Physical Review B*, 95(20), 2017.

[5] M. P. Marder. *Condensed Matter Physics*. John Wiley & Sons Inc., 2000.

[6] B. A. Piot, D. K. Maude, M. Henini, Z. R. Wasilewski, K. J. Friedland, R. Hey, K. H. Ploog, A. I. Toropov, R. Airey, and G. Hill. *Physical Review B*, 72(24):245325, 2005.

[7] K. von Klitzing, G. Dorda, and M. Pepper. *Physical Review Letters*, 45(6):494–497, 1980.

[8] C. R. Dean. *A Study of the Fractional Quantum Hall Energy Gap at Half Filling*. PhD thesis, McGill University, 2008.

[9] M. Fogler and B. Shklovskii. *Physical Review B*, 52(24):17366–17378, 1995.

[10] D. R. Leadley, R. J. Nicholas, P. J. Gee, H. Singleton, J., and C. T. J. J., and Foxon. In *22nd International Conference on the Physics of Semiconductors*, volume 3, 1995.

[11] R. Willett, J. P. Eisenstein, H. L. Störmer, D. C. Tsui, A. C. Gossard, and J. H. English. *Physical Review Letters*, 59(15):1776–1779, 1987.

[12] G. Moore and N. Read. *Nuclear Physics B*, 360(2-3):362–396, 1991.

[13] F. D. M. Haldane and E. H. Rezayi. *Physical Review Letters*, 60(10):956–959, 1988.

[14] N. Read and D. Green. *Physical Review B*, 61(15):10267, 2000.

[15] B. I. Halperin. *Helvetica Physica Acta*, 56:75–102, 1983.

[16] M. Levin, B. I. Halperin, and B. Rosenow. *Physical Review Letters*, 99(23):236806, 2007.

[17] S.-S. Lee, S. Ryu, C. Nayak, and M. P. A. Fisher. *Physical Review Letters*, 99(23):236807, 2007.

[18] B. I. Halperin. *Physical Review Letters*, 52(18):1583–1586, 1984.

[19] A. Kitaev. *Annals of Physics*, 303(1):2–30, 2003.

[20] S. D. Sarma, M. Freedman, C. Nayak, and S. Das Sarma. *Physical Review Letters*, 94(16):1–4, 2005.

[21] M. Dolev, M. Heiblum, V. Umansky, A. Stern, and D. Mahalu. *Nature*, 452(7189):829–34, 2008.

[22] I. P. Radu, J. B. Miller, C. M. Marcus, M. a. Kastner, L. N. Pfeiffer, and K. W. West. *Science*, 320(5878):899–902, 2008.

[23] V. Venkatachalam, A. Yacoby, L. Pfeiffer, and K. West. *Nature*, 469(7329):185–8, 2011.

[24] J. P. Eisenstein, R. Willett, H. L. Stormer, D. C. Tsui, A. C. Gossard, and J. H. English. *Physical Review Letters*, 61(8):997–1000, 1988.

[25] C. R. Dean, B. A. Piot, P. Hayden, S. Das Sarma, G. Gervais, L. N. Pfeiffer, and K. W. West. *Physical Review Letters*, 100(14):11–14, 2008.

[26] C. Zhang, T. Knuuttila, Y. Dai, R. R. Du, L. N. Pfeiffer, and K. W. West. *Physical Review Letters*, 104(16):2–5, 2010.

[27] S. Das Sarma, G. Gervais, X. Zhou, S. D. Sarma, G. Gervais, X. Zhou, and S. Das Sarma. *Physical Review B*, 82(11):1–6, 2010.

[28] L. Tiemann, G. Gamez, N. Kumada, and K. Muraki. *Science*, 335(6070):828–831, 2012.

[29] M. Stern, B. Piot, Y. Vardi, V. Umansky, P. Plochocka, D. Maude, and I. Bar-Joseph. *Physical Review Letters*, 108(6):1–5, 2012.

[30] H. Fu, P. Wang, P. Shan, L. Xiong, L. N. Pfeiffer, K. West, M. A. Kastner, and X. Lin. *Proceedings of the National Academy of Sciences*, 113(44):201614543, 2016.

[31] M. Dolev, Y. Gross, R. Sabo, I. Gurman, M. Heiblum, V. Umansky, and D. Mahalu. *Physical Review Letters*, 107(3):036805, 2011.

[32] R. L. Willett. *Reports on Progress in Physics*, 76(7):076501, 2013.

[33] P. Bonderson, A. Kitaev, and K. Shtengel. *Physical Review Letters*, 96(1):1–4, 2006.

[34] A. Stern and B. I. Halperin. *Physical Review Letters*, 96(1):1–4, 2006.

[35] R. L. Willett, L. N. Pfeiffer, and K. W. West. *Proceedings of the National Academy of Sciences*, 106(22):8853–8858, 2009.

[36] R. Willett, L. Pfeiffer, and K. West. *Physical Review B*, 82(20):1–12, 2010.

[37] C. Nayak, S. H. Simon, A. Stern, M. Freedman, S. Das Sarma, S. H. Simon, A. Stern, M. Freedman, and S. Das Sarma. *Reviews of Modern Physics*, 80(3):1083–1159, 2008.

[38] N. R. Cooper and A. Stern. *Physical Review Letters*, 102(17):176807, 2009.

[39] K. Yang and B. I. Halperin. *Physical Review B*, 79(11):115317, 2009.

[40] W. E. Chickering, J. P. Eisenstein, L. N. Pfeiffer, and K. W. West. *Physical Review B*, 81(24):245319, 2010.

[41] N. R. Cooper, B. I. Halperin, and I. M. Ruzin. *Physical Review B*, 55(4):2344–2359, 1997.

[42] Y. Barlas and K. Yang. *Physical Review B*, 85(19):195107, 2012.

[43] W. E. Chickering, J. P. Eisenstein, L. N. Pfeiffer, and K. W. West. *Physical Review B*, 87(7):075302, 2013.

[44] A. Y. Kuntsevich, Y. V. Tupikov, V. M. Pudalov, and I. S. Burmistrov. *Nature Communications*, 6:7298, 2015.

[45] W. E. Chickering, J. P. Eisenstein, and J. L. Reno. *Physical Review Letters*, 103(4):1–4, 2009.

[46] G. Gervais and K. Yang. *Physical Review Letters*, 105(8):1–4, 2010.

[47] A. Stern. *Nature*, 464(7286):187–93, 2010.

[48] J. Nuebler, V. Umansky, R. Morf, M. Heiblum, K. von Klitzing, and J. Smet. *Physical Review B*, 81(3):1–7, 2010.

[49] H. Choi, K. Yawata, T. M. Haard, J. P. Davis, G. Gervais, N. Mulders, P. Sharma, J. A. Sauls, and W. P. Halperin. *Physical Review Letters*, 93(14):145301, 2004.

[50] O. M. Corbino. *Physikalische Zeitschrift*, 12(14):561–568, 1911.

[51] D. A. Kleinman and A. L. Schawlow. *Journal of Applied Physics*, 31(12):2176, 1960.

[52] D. Midgley. *Nature*, 186(4722):377–377, 1960.

[53] M. Green. *Journal of Applied Physics*, 32(10):2047, 1961.

[54] H. Johnson and D. Midgley. *Proceedings of the IEE Part B: Electronic and Communication Engineering*, 109(45):283, 1962.

[55] R. B. Laughlin. *Physical Review B*, 23(10):5632–5633, 1981.

[56] P. F. Fontein, J. M. Lagemaat, J. Wolter, and J. P. Andre. *Semiconductor Science and Technology*, 3(9):915, 1988.

[57] V. T. Dolgopolov, A. A. Shashkin, N. B. Zhitenev, S. I. Dorozhkin, and K. Von Klitzing. *Physical Review B*, 46(19):12560–12567, 1992.

[58] B. Jeanneret, B. B. Hall, H. H.-J. Bühlmann, R. Houdré, M. Ilegems, B. Jeckelmann, and U. Feller. *Physical Review B*, 51(15):9752–9756, 1995.

[59] P. T. Coleridge. *Semiconductor Science and Technology*, 12(1):22, 1997.

[60] J. P. Harrang, R. J. Higgins, R. K. Goodall, P. R. Jay, M. Laviron, and P. Delescluse. *Physical Review B*, 32(12):8126–8135, 1985.

[61] S. Das Sarma and F. Stern. *Physical Review B*, 32(12):8442–8444, 1985.

[62] M. P. Lilly, K. B. Cooper, J. P. Eisenstein, L. N. Pfeiffer, and K. W. West. *Physical Review Letters*, 82(2):394–397, 1999.

[63] R. R. Du, D. C. Tsui, H. L. Stormer, L. N. Pfeiffer, K. W. Baldwin, and K. W. West. *Solid State Communications*, 109(6):389–394, 1999.

[64] N. Deng, J. D. Watson, L. P. Rokhinson, M. J. Manfra, and G. a. Csáthy. *Physical Review B*, 86(20):201301, 2012.

[65] W. Pan, J. S. Xia, H. L. Stormer, D. C. Tsui, C. Vicente, E. D. Adams, N. S. Sullivan, L. N. Pfeiffer, K. W. Baldwin, and K. W. West. *Physical Review B*, pages 1–18, 2008.

[66] G. Gamez and K. Muraki. *Physical Review B*, 88(7):075308, 2013.

[67] D. G. Polyakov and B. I. Shklovskii. *Physical Review Letters*, 48(1):4, 1994.

[68] N. D'Ambrumenil, B. I. Halperin, and R. H. Morf. *Physical Review Letters*, 106(12):126804, 2011.

[69] E. Gornik, R. Lassnig, G. Strasser, H. L. Störmer, A. C. Gossard, and W. Wiegmann. *Physical Review Letters*, 54(16):1820–1823, 1985.

[70] J. K. Wang, J. H. Campbell, D. C. Tsui, and A. Y. Cho. *Physical Review B*, 38(9):6174–6184, 1988.

[71] V. Bayot, E. Grivei, S. Melinte, M. Santos, and M. Shayegan. *Physical Review Letters*, 76(24):4584–4587, 1996.

[72] R. Franz and G. Wiedemann. *Annalen der Physik und Chemie*, 165(8):497–531, 1853.

[73] C. Kittel. *Introduction to Solid State Physics, 8th edition*. Wiley, 8 edition, 2004.

[74] K. Gloos, C. Mitschka, F. Pobell, and P. Smeibidl. *Cryogenics*, 30(1):14–18, 1990.

[75] P. Bonderson, A. E. Feiguin, and C. Nayak. *Physical Review Letters*, 106(18):186802, 2011.

[76] V. Karavolas and G. Triberis. *Physical Review B*, 59(11):7590–7595, 1999.

[77] Y. Kawano, Y. Hisanaga, H. Takenouchi, and S. Komiyama. *Journal of Applied Physics*, 89(7):4037–4048, 2001.

[78] K. S. Yngvesson. *Applied Physics Letters*, 76(6):777, 2000.

[79] H. L. Stormer, L. N. Pfeiffer, K. W. Baldwin, and K. W. West. *Physical Review B*, 41(2):1278–1281, 1990.

[80] A. Mittal. *Electron-Phonon Scattering Rate in GaAs/AlGaAs 2DEGs Below 0.5K*. Phd thesis, Yale University, 1996.

[81] P. J. Price. *Journal of Applied Physics*, 53(10):6863, 1982.

[82] V. Karpus. *Soviet Physics - Semiconductors*, 22(3):268, 1988.

[83] C. Jasiukiewicz and V. Karpus. *Semiconductor Science and Technology*, 11(12):1777–1786, 1996.

[84] N. J. Appleyard, J. T. Nicholls, M. Y. Simmons, W. R. Tribe, and M. Pepper. *Physical Review Letters*, 81(16):3491–3494, 1998.

[85] P. L. Gammel, D. J. Bishop, J. P. Eisenstein, J. H. English, A. C. Gossard, R. Ruel, and H. L. Stormer. *Physical Review B*, 38(14):10128–10130, 1988.

[86] A. Mittal, R. Wheeler, M. Keller, D. Prober, and R. Sacks. *Surface Science*, 361-362:537–541, 1996.

[87] E. Chow, H. P. Wei, S. M. Girvin, and M. Shayegan. *Physical Review Letters*, 77(6):1143–1146, 1996.

[88] J. Q. Zhang, S. Vitkalov, and A. A. Bykov. *Physical Review B*, 80(4):045310, 2009.

[89] W. Kang, S. He, H. L. Stormer, L. N. Pfeiffer, K. W. Baldwin, and K. W. West. *Physical Review Letters*, 75(22):4106–4109, 1995.

[90] B. Tieke, R. Fletcher, U. Zeitler, M. Henini, and J. C. Maan. *Physical Review B*, 58(4):2017–2025, 1998.

[91] D. V. Khveshchenko and M. Y. Reizer. *Physical Review Letters*, 78(18):3531–3534, 1997.

[92] N. Deng, A. Kumar, M. J. Manfra, L. N. Pfeiffer, K. W. West, and G. A. Csáthy. *Physical Review Letters*, 108(8):086803, 2012.

[93] J. P. Eisenstein, K. B. Cooper, L. N. Pfeiffer, and K. W. West. *Physical Review Letters*, 88(7):076801, 2002.

[94] I. V. Kukushkin, J. H. Smet, K. von Klitzing, and W. Wegscheider. *Nature*, 415(6870):409–12, 2002.

[95] M. Kumar, A. Laitinen, and P. Hakonen. *Nature Communications*, 9(1):1–8, 2018.

[96] Y. Zeng, J. I. A. Li, S. A. Dietrich, O. M. Ghosh, K. Watanabe, T. Taniguchi, J. Hone, and C. R. Dean. *Physical Review Letters*, 122(13):137701, 2019.

[97] D. Laroche, S. Das Sarma, G. Gervais, M. P. Lilly, and J. L. Reno. *Applied Physics Letters*, 96(16):162112, 2010.

[98] A. Kristensen, H. Bruus, A. E. Hansen, J. B. Jensen, P. E. Lindelof, C. J. Marckmann, J. Nygård, C. B. Sørensen, F. Beuscher, A. Forchel, and M. Michel. *Physical Review B*, 62(16):10950–10957, 2000.

[99] J. Li, Z. B. Zhang, M. Östling, and S. L. Zhang. *Applied Physics Letters*, 92(13):2006–2009, 2008.

[100] M. Green. *Journal of Applied Physics*, 32(7):1286, 1961.

[101] K. Fujita, a. Endo, S. Katsumoto, and Y. Iye. *Physica E: Low-dimensional Systems and Nanostructures*, 42(4):1030–1033, 2010.

[102] X. Liu, T. Li, P. Zhang, L. N. Pfeiffer, K. W. West, C. Zhang, and R.-r. Du. *Physical Review B*, 97(24):245425, 2018.

[103] R. Fletcher. *Semiconductor Science and Technology*, 14(4):R1, 1999.

[104] S. Kobayakawa, A. Endo, and Y. Iye. *Journal of the Physical Society of Japan*, 82(5):053702, 2013.

[105] N. Hartman, C. Olsen, S. Lüscher, M. Samani, S. Fallahi, G. C. Gardner, M. Manfra, and J. Folk. *Nature Physics*, 14(11):1083–1086, 2018.